In Situ Imaging of Metals in Cells and Tissues

Reagan McRae, Pritha Bagchi, S. Sumalekshmy, and Christoph J. Fahrni*

School of Chemistry and Biochemistry and Petit Institute for Bioengineering and Bioscience, Georgia Institute of Technology, 901 Atlantic Drive, Atlanta, Georgia 30332

Received June 20, 2009

Contents

1. Introduction 4780
2. Histochemical Techniques 4782
2.1. Chromogenic Detection with Chelators and Ligands 4782
2.1.1. Histochemistry of Iron 4782
2.1.2. Histochemistry of Copper 4783
2.1.3. Histochemistry of Zinc 4784
2.2. Fluorescence Probes 4784
2.3. Autometallography 4786
2.3.1. AMG Detection of Zinc 4787
2.3.2. AMG Visualization of Metals Other than Zinc 4787
3. Radioisotope Imaging Techniques 4788
3.1. Autoradiography 4788
3.1.1. Zinc Transport and Distribution in the Brain 4788
3.1.2. Manganese Transport and Distribution in Brain 4790
3.1.3. Iron Transport and Distribution 4791
3.1.4. Whole-Body Autoradiography 4791
3.2. Positron Emission Tomography (PET) 4791
4. Magnetic Resonance Imaging (MRI) 4792
4.1. Magnesium, Potassium, and Calcium 4793
4.2. Zinc 4793
4.3. Copper 4793
5. Microprobe X-ray Fluorescence Imaging Techniques 4793
5.1. Physical Background and Instrumentation 4793
5.1.1. Electron Beam Microprobe Methods 4793
5.1.2. Proton Beam Microprobe Methods 4795
5.1.3. X-ray Beam Microprobe Methods 4795
5.2. Metal Ions in Various Diseases and Medical Conditions 4796
5.2.1. Cancer Diagnosis and Disease Progression 4796
5.2.2. Anticancer Drugs 4797
5.2.3. Neurodegenerative Diseases 4797
5.2.4. Atherosclerosis and Cardiovascular Disease 4800
5.2.5. Other Diseases Linked with Abnormal Metal Homeostasis 4802
5.3. Xenobiotic Trace Metals and Materials 4804
5.3.1. Toxicology of Heavy Metals 4804
5.3.2. Nanoparticle Applications 4810
5.4. Environmental Metal Speciation 4812
5.4.1. Bacteria 4812
5.4.2. Aquatic Organisms 4812
6. Mass Spectrometry Imaging Techniques 4813
6.1. Secondary Ion Mass Spectrometry (SIMS) 4813
6.1.1. Metal Ion Distribution in Chromosomes 4813
6.1.2. Subcellular Distribution of Metal Ions 4814
6.1.3. Distribution of Metal Ions in Various Tissues 4815
6.1.4. NanoSIMS 4815
6.2. Laser Ablation Inductively Coupled Plasma Mass Spectrometry (LA−ICP−MS) 4816
6.2.1. Elemental Distribution in Brain Tissue 4816
6.2.2. Tumor Analysis in Various Tissues 4817
6.2.3. Xenobiotic Elemental Labeling 4817
6.2.4. Environmental Toxicology 4817
6.2.5. Isotope Ratio Measurements 4818
6.2.6. Near-Field Laser Ablation 4818
7. Conclusions 4818
8. Acknowledgments 4818
9. References 4819

1. Introduction

Approximately one third of the human proteome contains metal cations, either in the form of cofactors with catalytic functions or as structural support elements.[1,2] To guarantee a proper maintenance of this metal ion pool, both at the cellular and at whole organism levels, nature has evolved a highly sophisticated machinery comprised of a complex interplay between DNA, proteins, and biomolecules.[3] Over the past decades, a steadily growing number of diseases have been identified that are characterized by metal imbalance in cells and tissues. Among the most prominent examples rank Alzheimer's disease and Parkinson's disease, two neurodegenerative disorders that involve abnormal accumulation of transition metals in brain tissue.[4] While some progress has been made in understanding the molecular basis of these disorders, many important questions remain unanswered. For example, little is known about the cellular structures that are involved in transiently storing metal ions prior to their incorporation into metalloproteins or the fate of metal ions upon protein degradation. An important first step toward unraveling the regulatory mechanisms involved in trace metal transport, storage, and distribution represents the identification and quantification of the metals, ideally in context of their native physiological environment in tissues, cells, or even at the level of individual organelles and subcellular compartments.

Since the inception of the first histochemical methods for the microscopic demonstration of transition metals in tissues more than 140 years ago,[5] many highly sensitive microana-

* To whom correspondence should be addressed. Phone: 404-385-1164. Fax: 404-894-2295. E-mail address: fahrni@chemistry.gatech.edu.

10.1021/cr900223a CCC: $71.50
Published on Web 09/22/2009

Reagan McRae received her B.S. in Chemistry and Biochemistry from the University of the South - Sewanee, Tennessee, where she worked as an undergraduate researcher for Dr. Richard Summers and Dr. John Shibata in the areas of biochemistry/molecular biology and biophysical chemistry, respectively. In the summer of 2003, she worked as an undergraduate researcher at the University of Tennessee with Dr. Doug Gilman where she investigated mechanisms of amyloid plaque formation using bioanalytical approaches. In 2004, she joined the graduate program in the School of Chemistry and Biochemistry of Georgia Institute of Technology, Atlanta, where she is currently pursuing a Ph.D. degree in biochemistry with Dr. Christoph Fahrni. Her current research involves the study of the intracellular metabolism of copper and zinc using correlative optical and synchrotron X-ray fluorescence imaging techniques.

Pritha Bagchi received her M.Sc. (2002) in Chemistry from the University of Calcutta, India. In 2007, she joined the graduate program of Georgia Institute of Technology, currently working in the laboratory of Dr. Christoph Fahrni. Her current research is centered around copper transport and storage in mammalian cells using proteomics and cellular imaging techniques.

lytical techniques and instruments have been developed for the in situ analysis of trace metals. The aim of this review is to provide an overview of the most recent achievements in trace metal imaging while at the same time also offering a historical perspective of this rapidly evolving research field. Although this survey has been structured according to the various analytical techniques, particular emphasis is given to the biological background for a better understanding of the context and importance of each discussed study.

An overview of the most important microanalytical techniques currently available for the in situ detection of trace metals in cells and tissues is compiled in Table 1. Depending on the task, each technique may offer specific advantages and, of course, also disadvantages. Currently, synchrotron and focused ion-beam microprobes presumably offer the best combination of sensitivity and spatial resolution; however, the ionizing high-energy excitation beam is not compatible

Sumalekshmy Sarojini Amma obtained her master's degree in Organic Chemistry (1998) from Mahatma Gandhi University, Kerala, India, and a doctoral degree in Chemistry (2004) from University of Kerala, Trivandrum, India. Her Ph.D. project focused on the design and synthesis of charge-transfer-based fluorescent probes, under the supervision of Dr. K. R. Gopidas at the Photosciences and Photonics Division of the National Institute for Interdisciplinary Science and Technology (NIST-CSIR), Trivandrum. Subsequently, she joined Professor Andre Braun's group at University of Karlsruhe, Germany, as a Postdoctoral Fellow, where she was involved in multiple projects related to vacuum-irradiation-mediated functionalization of polymer nanoparticles. In 2006, she joined the School of Chemistry and Biochemistry at the Georgia Institute of Technology, Atlanta, as a Postdoctoral Fellow with Dr. Christoph Fahrni. Her current research focuses primarily on the development of novel two-photon-based fluorescence sensors for the detection of metal ions in biological systems.

Christoph J. Fahrni earned a master's degree in chemistry from the Federal Institute of Technology (ETH, Switzerland) and a Ph.D. degree in chemistry from the University of Basel (Switzerland). He simultaneously pursued studies in piano performance at the Conservatories of Zurich and Lucerne (Switzerland), where he earned a bachelor's and master 's degree. After working as a postdoctoral fellow at Northwestern University (Evanston, IL), he joined the School of Chemistry and Biochemistry at the Georgia Institute of Technology. His current research interests focus on the development of fluorescent probes and imaging methodologies for studying the physiology of trace metals in biological systems.

with studying live organisms. Conversely, techniques that have been specifically developed for physiological imaging in clinical medicine, notably magnetic resonance imaging and positron emission tomography, inherently offer only a low spatial resolution and are merely suitable for obtaining information at the organ or tissue level. Although fluorescence microscopy based methods provide very high sensitivity down to the single molecule level while being at the same time compatible with live cell and tissue studies, scattering and limited penetration depth render these techniques unsuitable for imaging opaque specimens. There are also important differences regarding the type of quantitative information that

Table 1. Spatially Resolved Microanalytical Techniques for in Situ Imaging of Trace Metals in Biology[6−11]

analytical method	detection limit	spatial resolution (μm)	analytical depth (μm)	quantification
electron probe X-ray microanalysis (EPXMA)[6]	100−1000 μg/g	0.03	0.1−1	semiquantitative
proton beam microprobe (PIXE, RBS, and STIM)[6]	1−10 μg/g	0.2−2	10−100	quantitative (PIXE-RBS)
X-ray microprobe (SXRF, μXAS, μXANES)[6,7]	0.1−1 (SXRF), 100 (μXAS) μg/g	0.03−0.2	>100	quantitative
laser ablation−inductively coupled plasma−mass spectrometry (LA−ICP−MS)[6]	0.01 μg/g	15−50	200	semiquantitative
secondary ion mass spectrometry (SIMS)[6]	0.1 μg/g	0.05	0.1	quantitative
magnetic resonance imaging (MRI)[8]	mM to low μM	25−100	no limit	semiquantitative
positron emission tomography (PET)[8]	high pM	1000−2000	no limit	semiquantitative
autoradiography[9]	<0.01 μg/g	0.1	no limit	semiquantitative
autometallography[10,11]	nM	0.001−0.005 (EM)	0.01−1 (EM)	semiquantitative
optical fluorescence microscopy[8]	pM to nM	2000−3000 (in vivo), 0.2−0.5 (in vitro)	<1 cm	qualitative/ semiquantitative
visible light microscopy	low μM	0.2−0.5	0.01−1	qualitative

can be gained by each of these analytical techniques. For example, histochemical detection with chromogenic and fluorogenic dyes relies on a competitive exchange of the metal ion within its native environment, most likely coordinated to endogenous ligands. Depending on the exchange kinetics and thermodynamic affinity of the histochemical indicator, only a fraction of the total metal ion contents in a cell or tissue can be probed. Nevertheless, this kinetically labile pool is particularly interesting in the context of understanding the uptake, distribution, and regulation of trace elements at the cellular level, and in this regard, these methods offer unique opportunities to dynamically image metal ion fluxes in live cells with high sensitivity and spatial resolution. At the same time, organelles and proteins of interest can be readily labeled with genetically encoded green fluorescent protein tags,[12] thus providing direct insights into dynamic processes within a larger cellular and biochemical context. In contrast, similar correlative information is difficult to gain with the fully quantitative microbeam methods, which require xenobiotic elemental tags for identifying subcellular structures. Autoradiographic tracer experiments offer much improved resolution over PET; however, the technique is only applicable to fixed or frozen tissues and cells. Furthermore, tracer studies cannot provide direct information regarding the endogenous metal composition of cells or tissues and are therefore primarily limited to metal uptake, distribution, and release studies. Finally, mass spectrometric analyses are surface-based methods that destroy the sample while measuring its elemental composition. Clearly, only the combination of several analytical techniques and specific biochemical studies may lead to a fully comprehensive analysis of a biological system.

2. Histochemical Techniques

Histology is the branch of biology dealing with the study of microscopic anatomy of cells and tissues of plants and animals. Histological studies are typically carried out on thin sections of tissue or with cultured cells. To visualize and identify particular structures, a broad spectrum of histological stains and indicators are available. Among the most widely used dyes are hematoxylin and eosin (H&E), which stain nuclei blue and the cytoplasm pink, respectively.[13] The history of detecting biological trace metals by histological methods dates back more than 140 years. Although these techniques have been today mostly replaced by the much more sensitive modern analytical methods described in this review, histochemical approaches for visualizing metals mark the very beginning in the exploration of the inorganic physiology of transition metals. Given this special place in history, we deemed it necessary to briefly review some of the early achievements in this field.

2.1. Chromogenic Detection with Chelators and Ligands

Ever since the inception of Perls Prussian blue method for staining of nonheme iron, numerous indicators have been developed for the in situ visualization of trace metals in biological tissues and cells.[13] Due to their limited sensitivity, however, most of these techniques were only suitable for the diagnosis of pathological conditions typically associated with excess metal accumulations, thus preventing their application for routine staining of normal tissue. Furthermore, because the dyes are engaged in a competitive exchange equilibrium with endogenous ligands, histological stains are not suitable for the analytical determination of the total metal contents in tissues and thus are limited to the visualization of the histologically reactive fraction of loosely bound labile metal ions.

2.1.1. Histochemistry of Iron

The histochemical demonstration of labile iron reported by Perls in 1867 is among the earliest accounts describing the in situ visualization of a trace metal in biological tissues.[5] The method was originally described by Grohe, who observed the formation of a blue coloration when he treated cadaver tissues with potassium ferrocyanide in acidic solution.[14] Due to its low cost and simplicity, the technique is still used today for the histological visualization of nonheme iron. Some variations focused on optimizing the concentrations and proportions of the reagents,[15−17] among which Lison's protocol[17] appears to be most popular today. An intensification of Perls' staining can be obtained by exploiting the use of ferric ferrocyanide in catalyzing the oxidation of

Chart 1

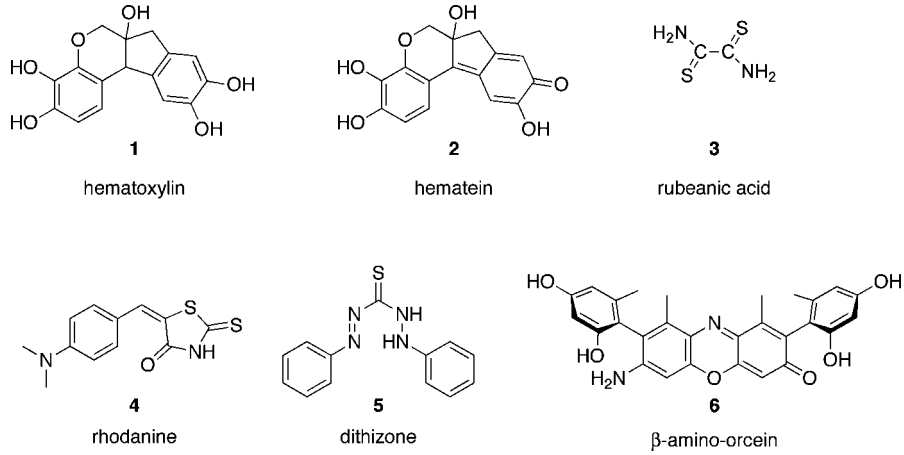

diaminobenzidine (DAB) to polymeric benzidine black by hydrogen peroxide.[18]

An alternative method employs the reaction of ferricyanide with Fe(II) resulting in Turnbull blue.[19] Since almost all of the Fe in tissues is in the ferric form, the staining procedure requires the in situ conversion of Fe(III) to Fe(II) with ammonium sulfide.[15] Due to often incomplete reduction, the method never gained much attention. More recently, an application of Turnbull blue, named the "perfusion Turnbull method" has been developed, where in vivo perfusion of acidic ferricyanide is followed by DAB intensification.[20] The direct in vivo perfusion avoids artifacts associated with tissue fixation, including the loss of loosely bound iron and oxidation of Fe(II) to Fe(III). Similarly, Perls method was modified by employing in vivo perfusion with acidic ferrocyanide. Both methods are capable of identifying organs and tissues containing histochemically reactive iron over a broad pH range, including the low endosomal pH.[21,22]

The history of iron histochemistry would be incomplete without mentioning Quincke's method, which employed ammonium sulfide for the precipitation of tissue iron as its sulfide.[23] A detailed account on the various techniques, including a comprehensive historical overview of nonheme iron chemistry, has been recently published.[24]

2.1.2. Histochemistry of Copper

The history of histochemical techniques for the identification of copper in a biological environment traces back to the late 19th century, where hematoxylin (**1**, Chart 1) was suggested as a stain for identifying the distribution of copper in diseased oysters.[25] The dye was later applied by Mendel et al. for exploring the distribution of inorganic constituents in the liver of *Sycotypus canaliculatus*.[26] Hematoxylin is a natural product isolated from the logwood tree. In its oxidized form, hematein (**2**), it combines with Al(III) or Fe(III) to give blue-purple colored pigments, which are still used as histological stains for cell nuclei. In 1939, Mallory and Parker further modified the protocol and emphasized the use of fresh ethanolic hematoxylin solutions to avoid interference from hematein formed upon prolonged storage.[27] Besides copper, hematoxylin forms colored pigments with a number of other transition metals. This lack of specificity prompted Okamoto in 1938 to explore alternative staining methods based on rubeanic acid (dithiooxamide, **3**),[28] which became one of the most widely used indicators for Cu. In alcoholic solution, rubeanic acid forms with Cu(II) a dark green precipitate of polymeric copper rubeanate. While the indicator also forms colored complexes with Ni(II), Ag(I), and Co(II), the corresponding precipitates can be visually distinguished based on their colors and further differentiated based on their solubility in acetate containing ethanol. With a detection limit of approximately 6 μM for Cu(II),[29] rubeanic acid is not sufficiently sensitive for visualizing labile copper levels present in normal tissue; however, it has been successfully applied to demonstrate copper in various tissues of Wilson's disease patients, including the liver,[30−32] central nervous system (CNS),[31] and kidney.[31,32] Recently, Lecca et al. further optimized the rubeanic acid method by incorporation of a microwave treatment, which resulted in better contrast and fewer artifacts.[33] Okamoto et al. explored the utility of two additional stains for the detection of copper, rhodanine (*p*-dimethylaminobenzylidene-rhodanine, **4**) and diphenylcarbazide.[34,35] Rhodanine forms a reddish brown precipitate with Cu(I) ions and gives a staining that follows a linear relationship with the metal ion concentration;[36] however, divalent copper salts do not react. As for the other indicators, the selectivity of diphenylcarbohydrazide toward copper was poor.[30] In 1945, Waterhouse introduced sodium diethyldithiocarbamate (DEDTC), which forms with Cu(II) a yellowish-brown precipitate. The limit of detection lies around 3 μM Cu(II) and is comparable to that of rubeanic acid.[37,38] Although the indicator has been successfully used for visualizing copper in different tissues, including liver and putamen,[30,39] the yellow color of the precipitate often resembles naturally occurring pigments inside cells, thus limiting its application in light microscopy. Dithizone (**5**) also forms a yellowish-brown complex with Cu(II) but offers only low sensitivity and selectivity.[40] Shikata et al. introduced the use of orcein (lacmus, litmus) for the histochemical staining of copper.[41] Orcein (**6**) is a mixture of phenoxazone derivatives extracted from orchella weeds. Later it was observed that it also stains copper-associated proteins.[42−44]

The methods described above often produced conflicting results[45] and were only applicable for detecting abnormally high levels of copper that is loosely bound in tissues. Some efforts focused on liberating bound copper with hydrogen peroxide[46] or concentrated hydrochloric acid.[31] Given the shortcomings of each method, it was recommended to apply typically a series of indicators to independently confirm the results.

2.1.3. Histochemistry of Zinc

The lack of visible color of zinc ions, both as solvated aqua complex and when coordinated to ligand or proteins, rendered the histological identification of zinc a challenging task. In 1905, Mendel and Bradley demonstrated for the first time the presence of labile zinc in hepatopancreatic tissues of *Sycotypus canaliculatus* using sodium nitroprusside followed by alkaline sulfide development.[26] Due to its low sensitivity, the protocol did not receive much attention at the time, despite the fact that the reaction was later demonstrated to be specific.[47] Important methods later developed for the histochemical detection of labile zinc include the dithizone (**5**) method (Chart 1), Timm's staining (section 2.3.1), and fluorescence-based approaches.[48,49] Okamoto introduced the dithizone method for the histochemical demonstration of zinc, which was employed as intravital staining to visualize zinc in islets of Langerhans found in the pancreas.[50−53] Dithizone reacts with Zn(II) to give a deep-red colored complex; however, similar complexes are also formed with a number of other transition metals. The specificity of complexation can be improved by adjusting the pH of the medium and the use of additional complex-forming reagents.[40] For example, one such modification employs a complex-forming buffer at pH 5.5 containing tartrate, thiosulfate, and cyanide, in which the dye combines predominantly with zinc, thus improving its selectivity by masking the interference of other metals. The dithizone staining technique has been extensively used for demonstrating zinc in a broad range of samples and tissues, including brain (hippocampus),[54−56] pancreatic islets,[57,58] prostate,[58] and blood cells[59] of dogs, humans, rabbits, and rats. Further modification of the method introduced an adduct formation of zinc−dithizone with pyridine resulting in an enhanced positive staining stable up to 1 week compared with the usual complex dissociation taking place within hours.[60] The presence of labile Zn(II) ions in brain tissues was first demonstrated by Maske et al. by means of intraperitonial injection of dithizone to form colored chelates,[61] although at that time the results were considered inconclusive because the method was believed to be nonspecific toward zinc. The report was later confirmed on the basis of in situ absorption spectroscopy of a dithizone-stained hippocampus tissue section and comparison with independently prepared reference samples of the Zn(II)−dithizone complex.[56] While dithizone staining is adequate for analyzing tissue with a high concentration of labile zinc, the pale and unstable staining, due to chelate decomposition upon exposure to heat, light, or solvents, further limits its application.[62]

2.2. Fluorescence Probes

Compared with chromogenic histochemical stains, fluorescent dyes offer much greater optical sensitivity and harbor the potential for observing biological processes at the single-molecule level.[63] Because of their small molecular size, synthetic indicators may passively diffuse across cell membranes and are thus well suited for the noninvasive imaging of cation fluxes in living cells. Given these attractive properties, it is not surprising that the development of new fluorescent probes and indicators represents a very active and steadily growing research area.[64] At present, fluorescent indicators have been developed for most biologically relevant metal cations, including calcium, magnesium, sodium, potassium, zinc, copper, and iron.[64,65] Furthermore, an increasing number of probes selective toward xenobiotic, toxic heavy metals have been described. Over the past decade, many excellent reviews summarizing these developments have been published, with topical areas covering both the principles and photophysics of probe design,[66−69] as well as comprehensive overviews on fluorescence detection of selected metal ions, most notably zinc[70−77] and mercury.[78] Rather than duplicate these efforts, this section has been limited to outlining a few cornerstones in the evolution of Zn(II)-selective fluorescence probes for biological applications, a particularly vital research area that best illustrates the rapid advances in this field.

For many years, dithizone was the only histochemical stain available for demonstrating Zn(II) ions in tissues.[48] In 1969, Mahanand and Houck described the first fluorescence indicator for the selective detection of Zn(II) in blood plasma and urine using 8-hydroxy-quinoline (**7**, Chart 2).[79] While the indicator formed stable complexes with many divalent metal ions, only binding of Zn(II), Mg(II), and Ca(II) led to a strong fluorescence increase, with Zn(II) displaying the highest binding affinity.[80] Similarly, a 2-methyl derivative of 8-hydroxy-quinoline was also described as a histochemical Zn(II) indicator.[81] Toroptsev and Eschenko explored the utility of several quinoline sulfonamide derivatives, structurally related to the 8-hydroxy-quinoline indicators, as fluorescence probes for Zn(II).[82−85] The bright-green fluorescence was found to colocalize with the dithizone staining in pancreatic beta cells and hippocampal mossy fibers. In the 1980s, Frederickson et al. explored the utility of another quinoline derivative, 6-methoxy-8-*p*-toluene sulfonamide quinoline (TSQ, **8**) as a histological indicator for Zn(II).[86,87] A comparison of TSQ with the established neo-Timm method demonstrated that the indicator is well suited as stain for demonstrating histochemically reactive Zn(II) in various tissues. In order to improve the water solubility and cellular retention, TSQ was later modified with a carboxylate group.[88−91] The resulting probe, zinquin ester (**9**), has been instrumental in elucidating the role of labile Zn(II) pools in a wide range of biological systems; however, the origin of the distinct vesicular staining pattern observed with Zinquin ester remains controversial. To address the question whether these zinc-rich vesicles, also referred to as zincosomes, might arise from a dye-induced sequestration of Zn(II), Wellenreuther et al. performed in situ microXANES (section 5.1.3) measurements with RAW264.7 cells.[92] The in situ data matched the X-ray absorption near-edge signature of isolated vesicles and implied that Zn(II) is present in complexed form with a coordination environment composed of sulfur, nitrogen (histidine), and oxygen donor atoms.

To avoid potentially damaging UV excitation, several fluorescein-based probes tethered to varying chelating units have been recently developed for excitation in the visible spectral range. For example, the ZnAF family of fluorescent probes developed by Nagano and co-workers combined the fluorescein platform with *N*,*N*-bis(2-pyridylmethyl)ethylenediamine as Zn(II)-selective binding unit. With a Zn(II) affinity of 2.7 nM, ZnAF2 (**10**) was successfully used for detecting synaptically released Zn(II) in hippocampal slices.[93,94] Further modifications with various chelating moieties furnished a series of indicators with a wide dynamic range for detecting Zn(II) from nanomolar to millimolar concentrations.[95] The fluorescent dyes revealed intriguing concentration differences of synaptically released Zn(II) in acute hippocampal slices.[95] In parallel, Lippard and co-workers devel-

Chart 2

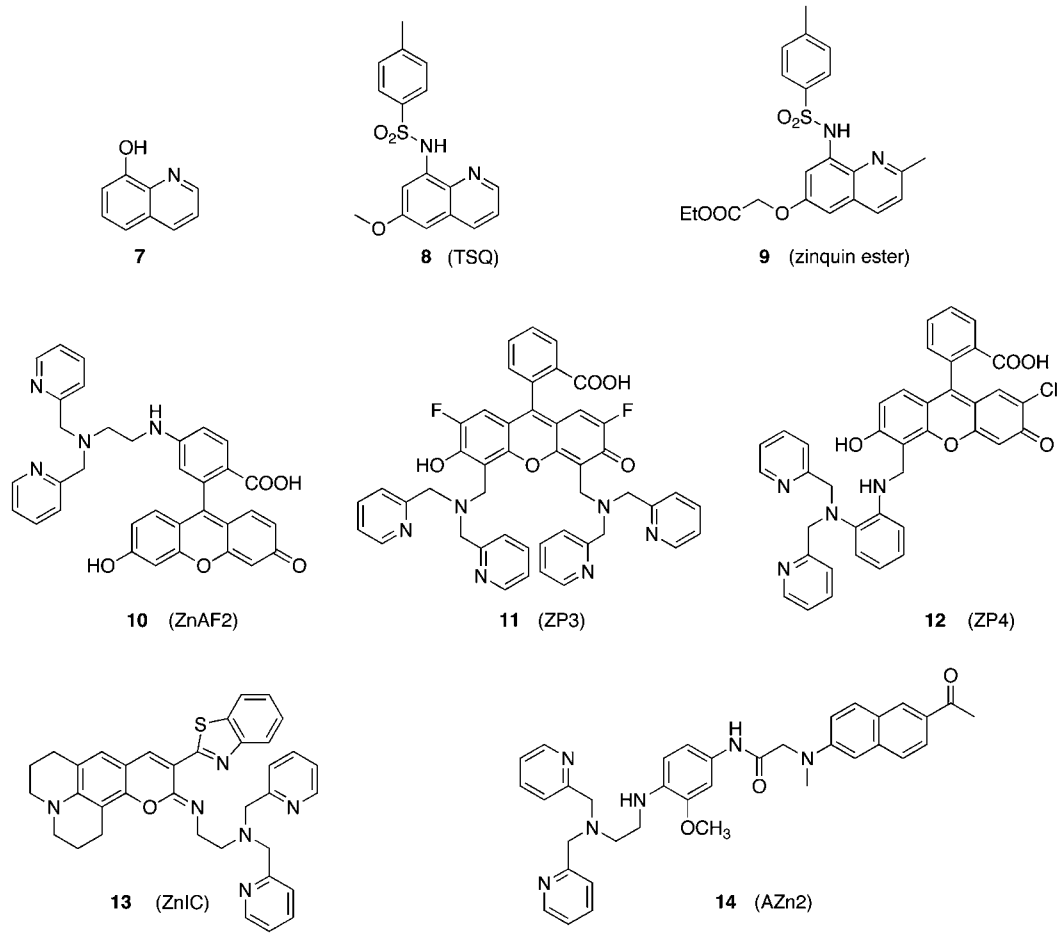

oped a large family of Zn(II)-responsive indicators, primarily aimed at unraveling the neurobiology of this metal ion. For example, the difluorofluorescein derivative ZP3 (**11**) was successfully utilized to image endogenous Zn(II) pools in hippocampal slices,[96] whereas the cell-impermeant indicator ZP4 (**12**) proved to be suitable for imaging extracellular Zn(II) and Zn(II)-damaged neurons.[97,98] A detailed review of this extensive body of work has been recently published.[77]

Several efforts focused on developing ratiometric probes for the detection of Zn(II) in biological systems.[76] Originally described by Tsien and co-workers for the dynamic visualization of Ca(II) fluxes,[99] ratiometric probes undergo a shift of the excitation or emission maxima upon binding of the analyte. By taking the ratio of the emission intensity at two different wavelengths, fluctuations due to uneven dye distribution, cellular uptake, or instrument-dependent factors are canceled out. For example, the iminocoumarin-based Zn(II) sensor, ZnIC (**13**), undergoes a red shift, from 543 to 558 nM, associated with an enhanced intramolecular charge transfer upon zinc binding at physiological pH. With a K_d of 1.3 pM, the sensor was successfully used for the ratiometric detection of Zn(II) in cultured cells and in rat hippocampal slices.[100]

The development of new imaging technologies typically requires also a tailored optimization of the indicator properties. With this goal in mind, Zn(II)-responsive indicators for application in two-photon excitation microscopy[101,102] and near-infrared (NIR) fluorescence imaging[103−105] have been developed. Due to the increased penetration depth of the low-energy infrared excitation, these two fluorescence microscopy techniques are particularly attractive for imaging thick tissues or potentially for whole animals studies. As illustrated in Figure 1, staining of rat hippocampal slices with the Zn(II)-responsive two-photon indicator AZn2 (**14**) revealed a characteristic staining pattern of histochemically labile Zn(II) pools. The fluorescence staining was reversed by addition of the high-affinity Zn(II)-chelator TPEN (Figure 1c), and a distinct increase in fluorescence intensity was observed upon stimulation with 50 mM KCl, suggesting the release of presynaptic Zn(II) stores (Figure 1e).

To this point, only few biologically oriented studies took advantage of the capabilities of these new fluorescent dyes. While the histochemical methods were limited to demonstrating labile Zn(II) in fixed specimens, with the inherently high detection sensitivity of fluorescence microscopy combined with a broad range of thermodynamic affinities, Zn(II)-responsive fluorescent indicators harbor great potential for visualizing dynamic Zn(II) fluxes with subcellular resolution in live cells and thus for elucidating important questions regarding the complex mechanism of cellular zinc homeostasis.

In contrast to the rich literature on Zn(II)-selective fluorescent probes, there are only a few reports on the detection of biological copper and iron, despite the fact that both metals are equally important trace elements within the cellular metallome. The fluorescence-based detection of these redox-active metals is particularly challenging due to competing metal-initiated fluorescence quenching pathways, for example through increased triplet conversion rates or energy transfer processes involving energetically low-lying metal-centered states. The adverse fluorescence quenching can be

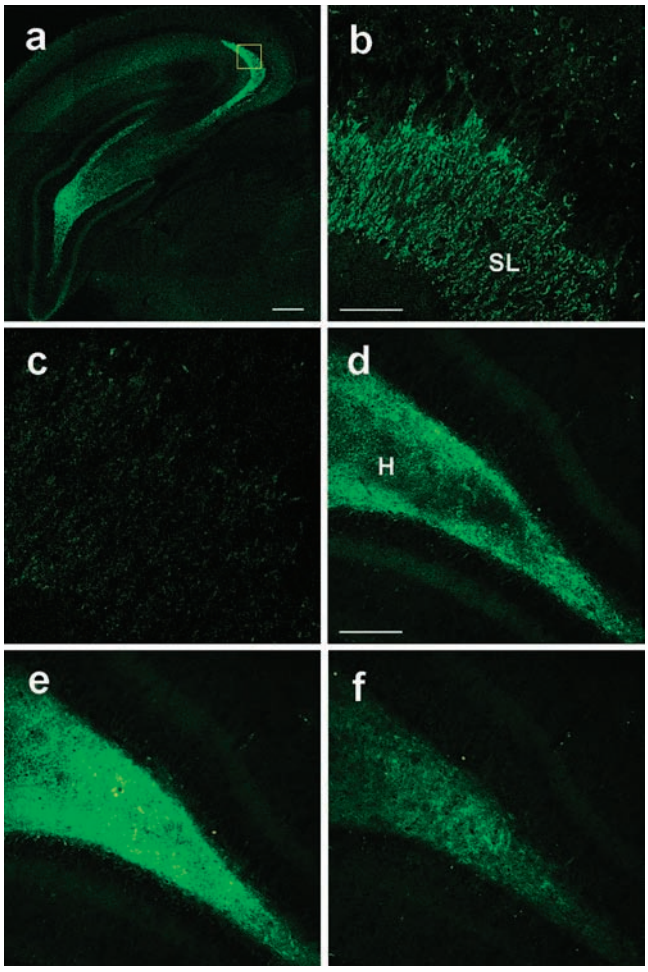

Figure 1. Two-photon excitation microscopy (TPM) images of a rat hippocampal slice stained with 10 μM AZn2 (**14**): (a) at a depth of ca. 120 μm with magnification 10×, scale bar = 300 μm; (b, c) magnification at 100× in the stratum lucidum (SL) of CA3 regions (yellow box in panel a) at a depth of ca. 100 μm before (b) and after (c) addition of 200 μM TPEN to the imaging solution, scale bar = 150 μm; (d−f) TPM images in the hilus (H) of dentate gyrus (DG) regions at a depth of ca. 100 μm before (d) and after (e) addition of 50 mM KCl to the buffer solution, scale bar = 300 μm, and (f) after addition of 200 μM TPEN to panel e sample. The TPEF images were collected at 500−620 nm with excitation at 780 nm using a femtosecond pulsed laser. Reprinted with permission from ref 101. Copyright 2008 Wiley.

minimized with a rigid fluorophore−ligand architecture, which electronically decouples the metal cation from the fluorescence emitter.[68,106] Following this concept, fluorescent probes for the detection of Cu(I) in cultured cells have been described.[107,108] A rigid probe architecture was also key in the design of a series of Fe(III)-selective probes, although the Fe(III)-induced fluorescence enhancements were only characterized in organic solvents.[109] In an alternative approach, Cu(II)- and Fe(III)-selective fluorescence enhancements were achieved through the metal-promoted ring-opening of nonfluorescent spirolactam rhodamine derivatives;[110,111] however, the sensing process is irreversible and might potentially also be initiated through an oxidative mechanism, thus complicating the interpretation of cellular imaging data. While at present the fluorescence detection of Fe and Cu in a biological environment poses still significant challenges, these initial successes clearly demonstrate its feasibility. Given that most biological laboratories are equipped with fluorescence microscopes, synthetic fluorescent probes remain particularly attractive for routine imaging of labile metal pools and will remain an active research area for developing materials with further improved selectivity and sensitivity.

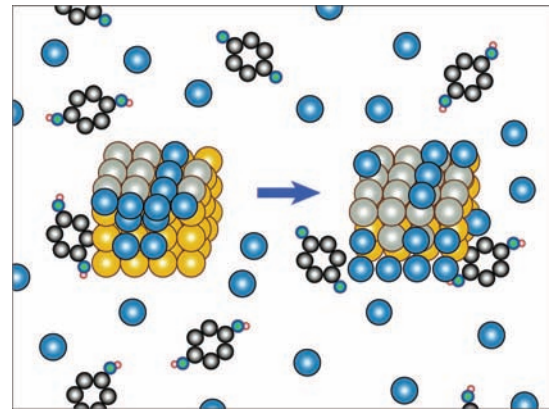

Figure 2. Principle of autometallographic silver enhancement (AMG). Electrons released from the reductant (hexagonal molecules) populate the valence band of the nanocrystal, thus increasing the probability for reducing silver ions that subsequently are integrated into the nanocrystal. As long as the AMG development proceeds, the nanocrystal will grow in size, that is, be silver-enhanced (hexagon molecules represent reducing agent; gold represents nanocrystals; blue represents silver ions; gray represents silver atoms). Reprinted with permission from ref 112. Copyright 2006 Elsevier.

2.3. Autometallography

A number of endogenous and toxic heavy metals form sulfide or selenide nanocrystals that can be autocatalytically amplified by reaction with Ag ions. The larger Ag nanocluster can then be readily visualized by electron or light microscopy. This property is the basis of all autometallographic amplification techniques, which evolved into an important tool in histochemistry.[112] At present, robust protocols for the silver-amplified detection of Au(0), Ag(0), Ag−S/Se, Hg−S/Se, Bi−S/Se, and Zn−S/Se nanocrystals have been established. Upon exposure to Ag(I), Hg(II), and Bi(III), organisms metabolically create in vivo composite sulfide and selenide nanocrystals that can be autometallographically detected. In addition, commercially available quantum dots are also autocatalytically active and may be used as histochemical labels. Of the endogenous metal ions, Zn(II) appears to be the sole cation that is converted to Zn−S or Zn−Se nanocrystals upon in vivo perfusion with sulfide or selenide ions, rendering autometallography (AMG) particularly attractive for visualizing Zn stores in tissues with high specificity. While it has been proposed that Cu, Fe, Al, and Pb can be also traced by AMG in tissues and cell cultures, the required high concentrations of sulfide and high pH mobilizes other metal ions from proteins. Under neutral conditions, none of these metals lead to formation of nanocrystals in the presence of sulfide, and neither are nanocrystals formed through metabolic accumulation.

As illustrated in Figure 2, in the autometallographic amplification process Ag ions adhere to the surface of the nanocrystal, where they are subsequently reduced to metallic silver by electrons released from a nearby reductant such as hydroquinone. The silver atoms continue to be incorporated into the original nanocrystal leading to autometallographic silver enhancement. This process continues as long as an adequate supply of both silver ions and reducing molecules is available (Figure 2).

The developer, which supplies the silver ions and reductant for the amplification process, is critical to the performance of AMG, and many groups devoted efforts to optimize the composition of developers. For example, the colloid gum arabic, a natural product employed in the original method, can lead to contaminations in the developer and was replaced by an industrial product sodium tungstate at pH 5.5.[113−116] For the analysis of ultrathin specimens, the AMG emulsion technique has been developed, which utilizes the "gum arabic silver lactate developer" or its improved variety "cellulose silver lactate developer".[117] In this technique, the tissue sections are first immersed in a silver-containing emulsion and are then exposed to a chemical developer containing the reductant. Because the fluid will pass through the emulsion, it will be enriched with silver ions, and thus the fluid penetrating in the tissue section will function as AMG developer.

As outlined in the following section, AMG has been predominantly used for the histochemical detection of labile zinc in tissues and to a lesser degree for visualizing other transition metals. A comprehensive review detailing the technique and protocols as well as their applications has been recently published.[117]

2.3.1. AMG Detection of Zinc

The AMG technique originally described by Timm in 1958 was geared toward the general detection of heavy metals in tissues;[118,119] however, the method has been later optimized for the selective detection of labile Zn(II) ions. As described in the previous paragraph, the AMG staining relies on the formation of a metal sulfide precipitate in the tissue during fixation by exposure to sulfides, followed by a silver developing process resulting in the deposition of elemental silver at metal localized sites. Haug et al. utilized this method by substituting the immersion of the tissue in hydrogen sulfide purged alcohol, as in the original Timm's method, with buffered sodium sulfide and successfully demonstrated labile Zn(II) in the hippocampal mossy fiber system.[120] The autometallographic detection of histochemically reactive Zn(II) ions played a critical role in elucidating the mechanism of Zn(II) translocation into synaptic vesicles, a process that is mediated through the zinc transporter-3 (ZnT-3).[121,122] Timm's original method has been modified over the years, most notably by Danscher and co-workers, who greatly improved its selectivity and sensitivity toward Zn(II).[117]

For example, the neo-Timm method is based on perfusion with a 0.1% solution of sodium sulfide, which avoids surplus sulfide ions that typically lead to false staining via the formation of Ag−S nanocrystals, and development with silver lactate, which undergoes fast dissociation to produce high levels of Ag(I) ions in the developer.[116] Further modification included an in vivo Timm's method employing intravenous injection of sodium sulfide followed by AMG development permitting the visualization of in vivo formed Zn−S nanocrystals.[124] The in vivo selenium method was later developed as a greatly improved Zn(II) specific protocol, where the sulfide treatment was replaced by intravital administration of selenide. Presumably due to the increased resistance of zinc selenide nanocrystals toward decomposition at low pH, this method improved the selectivity and broadened the utility of zinc AMG for use with live animals.[125,126] As illustrated in Figure 3, histochemically reactive Zn(II) in zinc-enriched neurons (ZEN) in a rat brain slice were captured with great detail, revealing highly ordered glutaminergic ZEN terminals.[123]

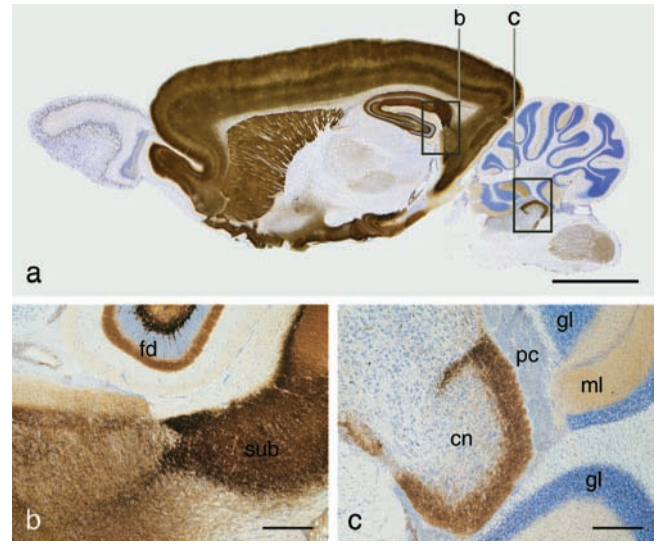

Figure 3. Histochemically reactive Zn(II) in zinc-enriched neurons (ZEN) in a rat brain slice: (a) Micrograph of a 30-μm-thick sagittal cryostat section of rat brain from an animal treated with sodium selenite and allowed to survive 1.5 h before being sacrificed by a transcardial perfusion with glutaraldehyde, detected with AMG and toluidine blue. The framed areas are magnified in panels b and c, bar = 5 μm. (b) ZEN terminals in the telencephalon, all believed to be glutaminergic, are highly ordered. The different shades from yellow to black are caused by the sizes and amounts of ZnSeAMG grains in the ZEN terminals. Small terminals with only one or two ZEN vesicles stain yellow, while huge ZEN boutons with many zinc-enriched synaptic vesicles stain black primarily because nearby AMG grains flow together, causing an increased absorption of light. Abbreviations: fd, fascia dentata; sub, subiculum. Bar = 300 μm. (c) The cochlear nucleus stains well; note also the yellow AMG staining of the molecular layer of spinocerebellum. Abbreviations: ml, molecular layer of spinocerebellum; gl, granular layer; cn, cochlear nucleus; pc, choroid plexus. Bar = 300 μm. Reprinted with permission from ref 123. Copyright 2005 Histochemical Society.

2.3.2. AMG Visualization of Metals Other than Zinc

2.3.2.1. Gold. Although gold compounds are being used for treatment of various diseases, most notably rheumatoid and psoriatic arthritis,[127] still little is known about their mechanism of action or biodistribution. AMG can be used to trace gold in tissues from individuals treated with gold-containing drugs,[128] where they appear to preferentially accumulate in lysosomes.[115,129−131] Other applications of AMG-based gold detection include the tracing of gold accumulation around gold implants used as a remedy for osteoarthritis[132] and enhancing colloidal gold particles associated with antibodies or enzymes as part of immunohistochemistry (see also section 5.3.2.2).[133]

2.3.2.2. Silver. AMG has been successfully used to trace silver in tissues with exposure to silver from different sources, for example, silver nitrate in throat swabs or amalgam fillings. The silver ions released as a result of the decomposition of silver-containing molecules in the lysosome can form silver−sulfur nanocrystals, which can be visualized by AMG.[134] The silver ions are also known to react with selenium to form silver−selenium nanocrystals, a suitable target for AMG identification.[135]

2.3.2.3. Mercury and Bismuth. Because mercury metabolically accumulates in lysosomes, leading to formation of

mercury−sulfide and mercury−selenide nanocrystals, this metal cation can be readily detected by AMG.[136] To assess the toxic effect of mercury in the central nervous system, Moller-Madsen and co-workers elucidated the detailed distribution of AMG-detectable mercury in the brain and in spinal cord of rats exposed to inorganic, organic, and vaporous forms of mercury.[137,138] Similarly, AMG was also applied to bismuth as demonstrated by experiments successfully conducted in mice exposed to bismuth subnitrate.[139] In light of the increasing utility of this metal in various fields of science, this method may serve as a valuable tool for exploring the in vivo distribution and toxicology of bismuth.[140]

2.3.2.4. Copper. The utility of Timm's stain for the demonstration of copper in normal tissues remained somewhat controversial, in part due to difficulties creating nanocrystals by exposure of copper to sulfide at physiological pH or by in vivo exposure to selenium.[117] Nevertheless, among traditional histochemical detection methods, the AMG detection of copper appears to be the most sensitive approach according to a study that focused on the demonstration of hepatic copper for the diagnosis of Wilson's disease.[141] Despite the lack of specificity, numerous reports in the literature describe the application of AMG for visualizing copper in tissues.[119,142,143] To improve the selectivity toward copper, washing with dilute acid[144] or trichloroacetic acid[145] was proposed, procedures thought to remove other competing metals. Another modification employed the formation of silver dithizonate from copper dithizonate formed by the reaction between tissue copper and magnesium dithizonate.[118] Application of this method after washing with trichloroacetic acid permitted the histological demonstration of copper in various tissues of normal rats.[146]

3. Radioisotope Imaging Techniques

Radioactive isotopes represent the cornerstone of nuclear medicine and have found widespread use in other branches of life sciences. Their application as sensitive biochemical markers can be traced back to the work of George de Hevesy in the early 20th century, who initially attempted to isolate a radioactive isotope of lead, at the time known as radium-D, from hundreds of kilograms of lead chloride.[147] Because he was not able to separate the two isotopes, he reasoned that the atomic number and not the atomic weight is responsible for the chemical properties of an element. Taking advantage of this observation, he used radium-D for the first time in 1913 as isotope tracer to determine the solubility of lead sulfide and chromate in water[148] and in 1923 to study the uptake and metabolism of lead salts into plants.[149]

A broad range of radioisotopes are available today as tracers for radioanalytical experiments; most notably ^{3}H, ^{14}C, ^{35}S, ^{32}P, ^{125}I, and ^{131}I are routinely used as isotopic labels in biochemical research. Radioactive isotopes have also secured an important place in studying the uptake and distribution of biologically relevant transition metals. An overview of metal isotopes commonly used in biochemical research and nuclear medicine is provided with Table 2. Although many of these radionuclides have been successfully used as biolabels to trace proteins or other molecules of interest, the following discussion focuses primarily on studies concerned with the inorganic physiology of the metal cations themselves. Because all naturally occurring transition metals of biological relevance are composed of stable isotopes, radiation-based detection is restricted to tracer studies aimed at quantifying the uptake, distribution, and release of metal ions and their complexes. In this context, it is important to note that radionuclide imaging techniques can provide little or no information regarding endogenous transition metal levels and their distribution under normal physiological conditions.

3.1. Autoradiography

Taking advantage of their decay emission, the distribution of radionuclides in biological specimens can be directly visualized by exposing a photographic film or emulsion in close contact. Because the radionuclide-containing specimen itself is the source of radiation, the technique is referred to as autoradiography.[150] In 1867, Niepce de Saint-Victor gave the presumably first account of autoradiography, in which he described the blackening of an emulsion of silver chloride and iodide by uranium nitrate and tartrate.[151] Curiously, this discovery is older than the knowledge of radioactivity itself, which was pioneered much later by the work of Henri Becquerel in 1896 and the Curies in 1898. For many decades, autoradiographic imaging as a biological technique evolved only very slowly, mostly due to the limited set of naturally occurring radionuclides, such as radium, thorium, or uranium, all of which were of little biological interest. With the invention of the cyclotron by Lawrence in 1930 and the large scale production of radionuclides in nuclear reactors, a broad spectrum of radioisotopes became available. Table 2 gives an overview of metal isotopes that have been used as tracers in biochemical research.

While early autoradiographic methods were limited to larger specimens, where the photographic film was simply pressed against fixed or freeze-dried sections for exposure, newer techniques involving liquid emulsions have been developed that are compatible with cellular or subcellular studies at the light and electron microscopic levels.[150] The resolution of an autoradiograph depends on the thickness of the specimen containing the radionuclide, its distance to the photographic emulsion, the thickness of the emulsion layer, and the radiation emitted by the radionuclide. Short-range radiations such as α or low-energy β radiation offer typically the best contrast. The detection sensitivity depends on the exposure time, which in turn varies as a function of the activity and energy of the radionuclide as well as the sensitivity of the photographic emulsion. In combination with transmission electron microscopy, autoradiography may offer a spatial resolution around 0.1 μm.[152]

3.1.1. Zinc Transport and Distribution in the Brain

Autoradiography has played a particularly important role in studying the transport, distribution, and function of Zn ions in the brain.[153,154] Perfusion experiments with $^{65}ZnCl_2$ provided first insights into the trafficking of Zn(II) ions across the blood−brain or blood−cerebrospinal fluid barrier in rats.[155−157] The data revealed slow Zn uptake of approximately 20 nmol/day across cerebral capillaries and an even lower rate of 0.2 nmol/day across the choroid plexus.[157] The autoradiographic distribution of ^{65}Zn showed low levels in white matter but relatively high levels in choroid plexus, cerebral cortex, and particularly the dentate gyrus.[157] A similar distribution pattern was reported in an earlier histochemical study with the Zn-responsive fluorescent probe TSQ.[158] Takeda et al. also concluded based on autoradiographic experiments with $^{65}ZnCl_2$ that the metal was gradually taken up by the brain via the cerebrospinal fluid in the

Table 2. Metal Radionuclides Used in Nuclear Medicine and Life Sciences.[a]

radioisotope	half-life	decay mode [b]	stable isotope product
^{22}Na	2.6027 y	ε; γ (1275)	^{22}Ne
^{26}Al	717 000 y	ε (18%); β^+ (82%; 1173); γ (1809)	^{26}Mg
^{45}Ca	162.61 d	β^- (256)	^{45}Sc
^{45}Ti	3.08 h	ε (15%); β^+ (85%; 1040); γ (720)	^{45}Sc
^{51}Cr	27.7025 d	ε; γ (320)	^{51}V
^{54}Mn	312.12 d	ε; γ (835)	^{54}Cr
^{59}Fe	44.50 d	β^- (466, 274); γ (1099, 1292)	^{59}Co
^{57}Co	271.74 d	ε; γ (122, 136)	^{57}Fe
^{60}Co	5.271 y	β^- (318); γ (1173, 1332)	^{60}Ni
^{63}Ni	100.1 y	β^- (66.9)	^{63}Cu
^{60}Cu	23.7 min	ε (7%); γ (1792, 1333, 826); β^+ (93%; 1981)	^{60}Ni
^{61}Cu	3.33 h	ε (39%); β^+ (61%; 1215); γ (283, 656)	^{61}Ni
^{64}Cu	12.70 h	ε (44%); β^+ (17%; 653); γ (1346); β^- (39%, 579%)	^{64}Ni (61%) ^{64}Zn (39%)
^{67}Cu	61.83 h	β^- (562, 468, 377); γ (185, 93)	^{67}Zn
^{65}Zn	244.06 d	ε; γ (1115)	^{65}Cu
^{69m}Zn [c]	13.76 h	IT, γ (439)	^{69}Zn (56.4 min) → ^{69}Ga
^{66}Ga	9.49 h	ε (44%); β^+ (56%; 4153); γ (2752, 1039)	^{66}Zn
^{67}Ga	3.26 d	ε; γ (93, 185, 300)	^{67}Zn
^{68}Ga	67.71 m	ε (12%); β^+ (88%; 1899); γ (1077)	^{68}Zn
^{73}As	80.30 d	ε; γ (54)	^{73}Ge
^{76}As	1.0778 d	β^- (2962, 2403); γ (559, 657)	^{76}Se
^{75}Se	119.79 d	ε; γ (121, 136, 264, 400)	^{75}As
^{86}Rb	18.64 d	β^- (1774); γ (1077)	^{86}Sr
^{86}Y	14.74 h	β^+ (32%; 1221); γ (1077)	^{86}Sr
^{90}Y	64.1 h	β^- (2280); γ (2186)	^{90}Zr
^{99m}Tc [c]	6.01 h	IT; γ (141)	^{99}Tc (2.11E5 y) → ^{99}Ru
^{109}Cd	461.4 d	ε; γ (88)	^{109}Ag
^{115}Cd	53.46 h	β^- (1110, 582); γ (336, 527)	^{115}In
^{110m}Ag [c]	249.76 d	IT; γ (118)	^{110}Ag (24.6 s) → ^{110}Cd
^{111}In	2.81 d	ε; γ (171, 245)	^{111}Cd
^{113}Sn	115.09 d	ε; γ (392, 255)	^{113}In
^{137}Cs	30.08 y	β^- (514); γ (662)	^{137}Ba
^{141}Ce	32.51 d	β^- (582, 436); γ (146)	^{141}Pr
^{152}Eu	13.54 y	ε; γ (122, 964, 1112, 1408); β^- (696); γ (344, 779)	^{152}Sm (72%) ^{152}Gd (28%)
^{154}Eu	8.59 y	β^- (841, 571); γ (123, 248, 723, 1005, 1274)	^{154}Gd
^{153}Sm	46.50 h	β^- (808, 704, 635); γ (70, 103)	^{153}Eu
^{186}Re	3.72 d	β^- (93%, 1070, 932); γ (137); ε (7%); γ (123)	^{186}Os (92%) ^{186}W (8%)
^{188}Re	17.00 h	β^- (2120, 1965); γ (155)	^{188}Os
^{203}Hg	46.59 d	β^- (213); γ (279)	^{203}Tl
^{203}Pb	51.92 h	ε; γ (279)	^{203}Tl
^{212}Pb	10.64 h	β^- (331); γ (239)	^{212}Bi

[a] Data taken from the National Nuclear Data Center (NNDC) of the U.S. Department of Energy (http://www.nndc.bnl.gov, Aug. 2009). [b] Decay energies in parentheses provided in units of kiloelectonvolts. Percentage values refer to the branching ratio if more than one decay pathway is present. Decay mode abbreviations: ε, electron capture; β^-, β particle emission; β^+, positron emission; γ, gamma-ray emission; IT, isomeric transition. [c] Metastable isotope isomer.

choroid plexus.[159,160] The study showed that ^{65}Zn was largely concentrated in the choroid plexus of rats 1 h after intravenous injection of $^{65}ZnCl_2$ and then slowly distributed in the hippocampus and cerebral cortex region. Because the choroid plexus is the site of cerebrospinal fluid (CSF) production, the experiments suggested that Zn is transported via CSF into the choroid plexus. The half-life of elimination of ^{65}Zn ions from the rat brain is in the range of 16−43 days,[161] with the longest being associated with the amygdala region consisting of high-density zinc-containing neuron terminals.[162]

The major carrier protein for labile zinc in the plasma is serum albumin and the other components of exchangeable zinc are the amino acids histidine and cysteine.[163] In order to assess the role of serum albumin as a transporter of zinc to the brain, autoradiographic images of ^{65}Zn distribution in the brain of Nagase analbuminemic rats (NARs) were compared with normal rats.[164] NARs have been found to have a genetic mutation that results in a lack of serum albumin.[165] The study demonstrated that ^{65}Zn distribution in the NAR brain is similar to that in normal rats and suggested that albumin may not be essential for Zn transport into the brain.

In order to understand possible roles of histidine in Zn transport to the brain, ^{65}Zn−His complex or $^{65}ZnCl_2$ was injected intravenously into rats.[166,167] In both cases, autoradiographic imaging of brain tissue sections revealed similar ^{65}Zn distribution patterns, indicating that histidine does not block Zn uptake; however,^{65}Zn−His injection resulted in overall lower Zn levels compared with $^{65}ZnCl_2$. Despite the similarities in coordination chemistry, intravenously injected ^{109}Cd(II) was not significantly transported into the brain according to a set of autoradiographic experiments.[168,169] Detailed binding studies demonstrated that the affinity of Cd(II) to serum proteins is substantially higher compared with that of Zn(II) and that Cd(II) is not mobilized from proteins by histidine at concentrations present in the plasma.[169] Based on these observations, the authors propose that the Cd(II) impermeability is due to the avid binding of Cd(II) to plasma proteins.

Infants and school-age children are particularly susceptible to dietary Zn deficiency and malnourishment, often leading to altered growth and behavior problems.[170] Several autoradiographic studies were aimed at elucidating possible roles of Zn in brain development and function. For example, imaging of ^{65}Zn distribution in the brains of neonatal, young,

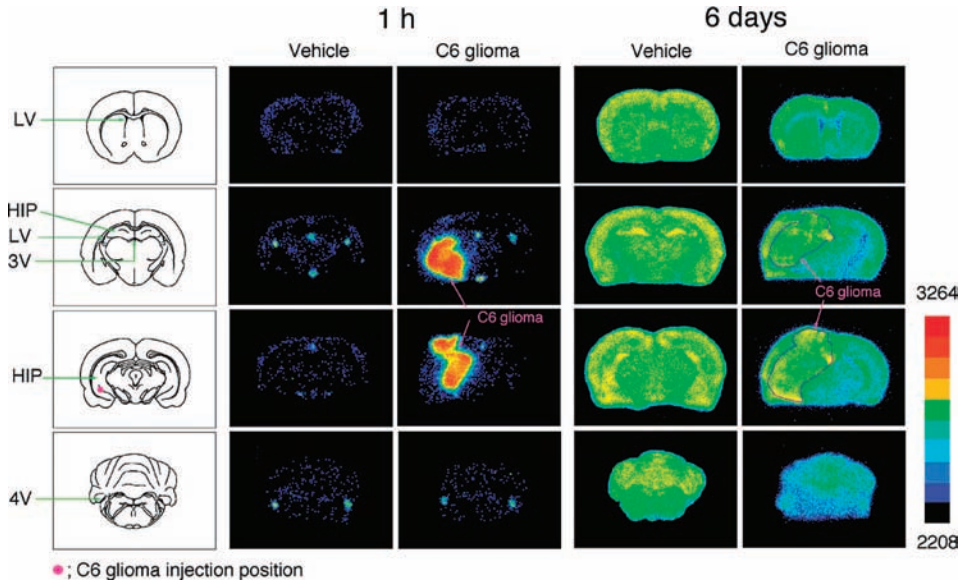

Figure 4. ^{65}Zn imaging of brain tissue sections implanted with C6 glioma cells. $^{65}ZnCl_2$ was intravenously injected into rats 14 days after injection of vehicle (control) or C6 glioma cells into the hippocampus ($n = 4$). Autoradiography was performed on selected coronal slices 1 h and 6 days after injection of $^{65}ZnCl_2$. Each experiment was performed four times, and the autoradiograms obtained were almost identical. The schemes (left-hand side) show maps of the rat brain. Abbreviations: LV, lateral ventricle; 3V, third ventricle; 4V, fourth ventricle; HIP, hippocampus. Reprinted with permission from ref 183. Copyright 2003 Elsevier.

and aging rats indicated that Zn is highly demanded in the neonatal brain by the cerebellum, which develops rapidly after birth.[171] While older rats showed an approximately 2-fold higher total Zn concentration, a more even distribution between the cerebellum and the cerebral cortex was found. A direct relationship between dietary zinc and zinc homeostasis in the brain evolved from a study where rat brains were examined for endogenous Zn level and uptake of Zn after they were fed a zinc-deficient diet for 12 weeks.[172] The endogenous zinc concentration in the hippocampus was significantly decreased in the brain of rats fed a zinc-deficient diet compared with that of controls. After intravenous administration of $^{65}ZnCl_2$, Zn uptake into the brain was significantly higher in Zn-deprived compared with control rats.

Epilepsy is a common neurological disorder manifested by uncontrolled seizures. Several studies directly indicate that alteration of zinc homeostasis in the brain may be associated with epileptic seizures.[173−175] To study changes in Zn distribution under induced seizure conditions, Takeda et al. intravenously injected $^{65}ZnCl_2$ into epilepsy (EL) mice, an animal model of genetically determined epilepsy.[176] While uptake of zinc by the brain is normal in EL mice, autoradiographic analysis revealed overall reduced Zn concentrations in the brain of seized EL compared with control mice. The concentration of ^{65}Zn was notably decreased in the piriform cortex and the amygdaloid nuclei complex during convulsion. In a related study, epileptic seizure was induced in normal mice by treating with kainate,[177] an experimental model for studying temporal lobe epilepsy.[178] In agreement with above results, autoradiographic imaging demonstrated that ^{65}Zn concentrations in the brain of kainate-treated mice were much lower compared with normal mice.

Dietary zinc deficiency also impacts tumor growth and malignant proliferation,[179−181] an observation that prompted Takeda et al. to study ^{65}Zn uptake in tumors.[182] Following subcutaneous implantation of ascites hepatoma (AH7974F) cells into the dorsum, $^{65}ZnCl_2$ was intravenously injected, and the ^{65}Zn distribution was autoradiographically assessed in the whole animal. While the study revealed significantly higher Zn concentrations in the tumor compared with brain tissue, the highest Zn concentrations were found in the liver. In a similar study, following implantation of C6 glioma cells into the hippocampus, ^{65}Zn uptake in the tumor 6 days after the injection of $^{65}ZnCl_2$ was more pronounced than in other brain regions (Figure 4).[183] Based on these results, the authors propose that ^{69m}Zn, a short-half-life γ-emitter (Table 2), might be utilized for the evaluation and viability of brain tumors.

3.1.2. Manganese Transport and Distribution in Brain

Similar to Zn, Mn is also required for proper brain function and development; however, chronic exposure to Mn is toxic and has been linked to neurodegenerative disorders.[184] Approximately 80% of the total Mn in the central nervous system is found in the active site of glutamine synthetase, an enzyme that catalyzes the conversion of glutamic acid to glutamine.[185] After intestinal absorption, dietary Mn is transported to the liver prior to delivery to the brain.[186] The blood−brain and blood−cerebrospinal fluid barriers are two barrier systems in the brain that are critical to normal functioning and have been implicated in various neurodegenerate diseases.[187] Similar to other trace metals, the blood−brain barrier constitutes the main supply route for Mn to the brain. Autoradiographic studies revealed that Mn enters the brain from the blood mainly across the cerebral capillaries and the cerebrospinal fluid.[159,160] Within 1 h postinjection, the metal accumulated in the choroid plexus, and after 3 days, it redistributed to the dentate gyrus and CA3 of the hippocampus.[159] The biological half-life for elimination of ^{54}Mn from the brain was determined to be in the range of 51−74 days.[161] A study with rats varying in age between 5 days and 95 weeks also underscored the importance of Mn in the developing brain.[188] As already observed for Zn, ^{54}Mn uptake was highest for the neonatal age group. The highest Mn concentrations were found in the hippocampal CA3, the dentate gyrus, and the pons, thus

contrasting the aging brain, with ^{54}Mn being located in the inferior colliculi, olivary nuclei, and red nuclei.[188] These findings strongly suggest that Mn serves a dual role in both brain development and its normal function.

Despite the similarities of Mn uptake into the brain, the transport mechanisms and involved proteins appear to be different. There is evidence that transferrin (Tf), the principal Fe carrier protein, might also be involved in Mn transport to the brain,[189,190] although non-protein-bound Mn enters the brain more rapidly than Tf.[191,192] Given the presence of Tf receptors on the surface of the cerebral capillary endothelial cells,[193] it is conceivable that Tf-bound Mn is released within the cells and subsequently transferred to the abluminal cell surface for extracellular release into the interstitial fluid. To examine the role of transferrin in the Mn distribution in the brain, ^{54}Mn concentrations were autoradiographically monitored after intravenous injection under three different conditions: untreated aqueous $^{54}MnCl_2$, pH 8.6 buffered $^{54}MnCl_2$, which has a higher affinity for transferrin, and transferrin-bound ^{54}Mn(III).[194] One hour after injection, both $^{54}MnCl_2$ and buffer-treated $^{54}MnCl_2$ were found to be concentrated in the choroid plexus region. After 6-days, all three tracers were distributed in inferior colliculi, red nuclei, and superior olivary complex; however, the radioactivity from transferrin-bound ^{54}Mn(III) was the lowest of all three substrates. The results suggest that Mn is transported into the brain by a pathway that is not solely dependent on transferrin. Another study with hypotransferrinemic mice, an animal model with low plasma transferrin concentration,[195] came to a similar conclusion that Tf is not required for Mn transport across the blood−brain barrier.[196]

3.1.3. Iron Transport and Distribution

In the brain, iron is mostly concentrated in oligodendrocytes and may be required in myelin synthesis.[197] The Fe transport protein Tf is presumed to be directly involved in delivery of Fe across the blood−brain barrier through receptor-mediated endocytosis as described in the previous section.[198,199] While transferrin is mainly expressed in the liver, a substantial amount of the protein is also found in the brain.[200] Iron saturation of plasma transferrin is one of the hallmarks of hereditary hemochromatosis, an iron overload disorder that leads to abnormal iron deposition in tissues, especially the liver.[201] The pathological condition of hemochromatosis can be simulated by iron saturation of transferrin with ferric chloride in citrate buffer. Following this protocol, Takeda et al. tested the effect of ^{59}Fe saturation of transferrin on its delivery into the brain by autoradiographic imaging.[202] The study showed that 24 h after injection of $^{59}FeCl_3$ into the bloodstream, the ^{59}Fe concentration in the brain of iron-loaded mice was lower compared with untreated control mice, except within the choroid plexus region, which showed an equal concentration. At the same time, the ^{59}Fe concentration in the liver was found to be four times higher compared with that in control mice. These results suggest that non-transferrin-bound iron is primarily absorbed by the liver, thus leading to a decrease in Fe delivery to the brain through the transferrin-mediated pathway. These findings agree with the observation that hereditary hemochromatosis is rarely accompanied by neurological disorders.[203]

The hypotransferrinemic (HP) mouse is a naturally occurring mutant with a point mutation or small deletion in the transferrin gene, resulting in <1% production of the normal circulating level of plasma transferrin. Takeda et al. used this animal model to study Fe transport to the brain under transferrin-deficient conditions.[204] The autoradiographic study was conducted with brain tissue of neonatal HP mice at 7 days of age and control mice, both of which were treated with a subcutaneous injection of $^{59}FeCl_3$. The results showed abnormal Fe accumulation in HP mice compared with control mice. At the same time, the clearance of ^{59}Fe from the blood was more efficient in HP mice compared with controls. Brain transferrin levels gradually decrease with age and are particularly low in the case of Alzheimer's or Parkinson's disease, both of which are characterized by Fe deposition in brain tissue.[205]

3.1.4. Whole-Body Autoradiography

Whole-body autoradiography is widely used as a tool for toxicological screening in the food and drug industry. For example, the interactions among infectious agents, nutrients, and xenobiotics have been studied to understand the effects of infections in food-producing animals. Ilback et al. showed that the distribution of xenobiotics in the body is altered during infection. During coxsackie virus infection, toxic xenobiotics, including Cd and Ni, distributed differently in the body of affected individuals compared with that of control groups. Whole-body autoradiography of virus-affected mice showed that Ni accumulated in the pancreas and heart,[206] whereas Cd was located in the kidney and spleen.[207]

Radioimmuno conjugates are used in cancer therapy but the success of this method depends on the therapeutic index, that is, the ratio of the dose of the therapeutic agent that causes the therapeutic effect to the dose that causes the death. Whole-body autoradiography is often used to assess adverse radiation effects of radioimmuno conjugates in healthy tissue. For example, being a pure β emitter causing less radiation hazard, ^{90}Y-based immuno conjugates showed great promise in radioimmuno therapy; however, whole-body autoradiography demonstrated that ^{90}Y was released from the radioimmuno conjugates and accumulated in the skeleton causing bone marrow toxicity.[208] In a similar study, whole-body autoradiography was used to assess samarium-153 uptake from radioimmuno conjugates by liver and bone.[209]

3.2. Positron Emission Tomography (PET)

As the name suggests, positron emission tomography (PET) is an imaging technique based on the detection of positron-emitting radionuclides, which are typically introduced as tracers attached to biologically active molecules.[210] The annihilation process of an emitted positron with a nearby electron produces two 511 keV photons, which are simultaneously emitted in opposite directions. By coincidental detection of the photon pairs using a series of X-ray detectors arranged around a ring, the spatial position of the tracer can be determined, and after sufficient acquisition time, an image of the 3D distribution of the radiotracer can be reconstructed. With a spatial resolution of about 5 mm for current human scanners, PET is substantially less sensitive compared with autoradiographic imaging; however, the technique is minimally invasive and can be used for clinical imaging of physiological processes in patients, whereas autoradiographic imaging is a purely histological method. The most frequently used PET isotopes are ^{11}C, ^{13}N, ^{15}O, and ^{18}F. Due to their short half-lives ranging only between 3 and 110 min, the production of these tracers requires highly efficient syntheses

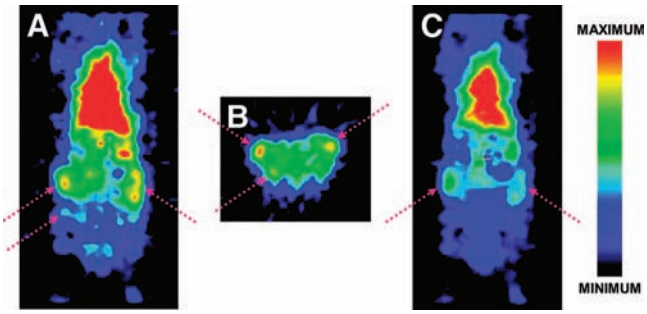

Figure 5. Positron emission tomography (PET) using ^{45}Ti as tracer nuclide. Two coronal microPET image slices (A, C) and one transaxial slice (B) of female BALB/c mouse bearing EMT-6 tumors (denoted by arrows) in both legs (right-hand side, one large tumor; left-hand side, two small tumors) injected with 27.72 MBq (750 μCi) ^{45}Ti−transferrin, imaged 1 h 40 min after injection. Reprinted with permission from ref 216. Copyright 2005 Society for Nuclear Medicine.

and purification techniques.[211] While the majority of metal nuclides are β or γ emitters, a few decay by positron emission and can be used for PET (Table 2). The following section provides an overview of metal isotopes that have been used for PET. Although these isotopes have been primarily used as radiopharmaceuticals or tracers,[212] they also offer an opportunity to directly study their physiology in whole organisms.

The nephrotoxicity and myelotoxicity of platinum-based anticancer drugs initiated a search for alternative organometallic complexes with similar activities. As a result, several titanium compounds are being investigated as potential antitumor drugs (see also section 5.2.2.2).[213] With a half-life of 3.08 h and a low positron emission energy comparable to the widely used isotope ^{18}F, ^{45}Ti is well-suited as a PET imaging nuclide (Table 2); however, very little is known about the biological chemistry of titanium compounds. Because titanocene dichloride rapidly hydrolyzes in aqueous solution to form insoluble polymers, Ti(IV) has been bound to transferrin, which under normal conditions is only 30% saturated with Fe(III) ions. Calorimetric studies demonstrated that transferrin binds Ti(IV) with even higher affinity than Fe(III).[214] A series of biodistribution and PET studies, conducted with ^{45}Ti-labeled transferrin in BALB/c mice implanted with mammary carcinoma tumors (EMT-6), revealed that the labeled transferrin was stable in vivo and taken up by the tumor (Figure 5).[215,216]

Copper offers three positron-emitting isotopes, ^{60}Cu, ^{61}Cu, and ^{64}Cu, all of which emit γ rays that are within the data acquisition window of PET. Unlike ^{60}Cu and ^{61}Cu, ^{64}Cu decays also by electron capture (44%) and β^- emission (39%), which results in Auger electron emission (Table 2). For this reason, this isotope has also the potential to be used as a therapeutic radionuclide. Because Cu(I) and Cu(II) complexes typically undergo rapid ligand exchange reactions, the design of kinetically inert complexes suitable for in vivo applications is very challenging. An extensive review of copper chelators and their applications as radiopharmaceuticals has been recently published.[217]

The combination of several imaging modalities harbors great potential for gaining multiple analytical information on the same system. Most recently, Berezin et al. combined a copper chelator with a cyanine fluorescence dye and demonstrated a radioactivity-synchronized fluorescence enhancement with the decay of ^{64}Cu(II) to its daughter nuclide ^{64}Zn(II).[218]

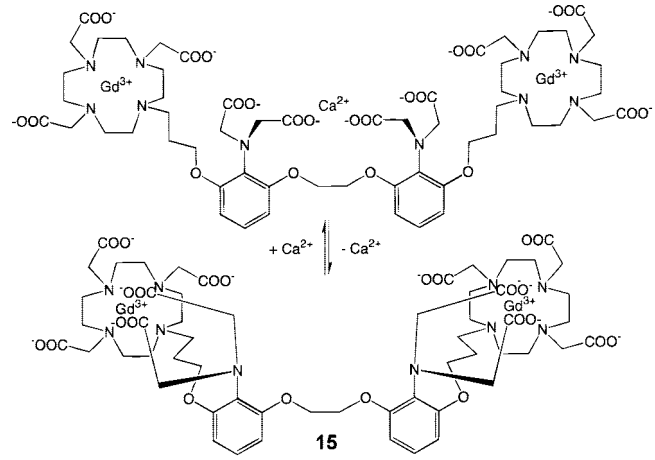

Figure 6. Schematic illustrating the switching mechanism of the Ca(II)-responsive MRI probe DOPTA−Gd (**15**). Binding of Ca(II) to the DOPTA ligand induces a conformational change, which in turn increases the relaxivity of water due to the additionally available coordination sites at the Gd(III) centers.[226]

With a short penetration range of approximately 10 μm and a maximum β^- emission energy of 2.28 MeV (Table 2), ^{90}Y is widely used as a therapeutic reagent in nuclear medicine.[219] Because the isotope does not emit γ rays, internal doses and the localization of ^{90}Y-labeled radiopharmaceuticals are difficult to assess, a shortcoming that has been successfully addressed with PET using the positron-emitting radionuclide twin ^{86}Y.[220−224]

4. Magnetic Resonance Imaging (MRI)

Similar to positron emission tomography (PET) and computed tomography (CT), magnetic resonance imaging (MRI) is a widely used medical imaging technique for the in vivo visualization of the structure and physiology of the human body or animals. MRI provides three-dimensional images of intact opaque tissues, but unlike PET and CT, the technique does not rely on ionizing radiation and offers a much improved contrast. The technique is based on a NMR signal predominantly arising from hydrogen atoms of water present in the tissue, and the signal intensity originates from the longitudinal ($1/T_1$) and transverse ($1/T_2$) relaxation rates of water protons aligned in a strong magnetic field. The relaxation rates of protons can be enhanced by using contrast agents (CA), typically composed of a paramagnetic metal ion such as Gd(III), which accelerate T_1 through direct interaction of the unpaired electrons with the water molecule.[225] While a vast research effort has focused on the development of improved contrast agents and bioconjugates for targeted imaging,[225] the detection of metal ions by MRI has received much less attention. Analogous to chromogenic or fluorescence indicators, MRI probes rely on a competitive binding of the metal cation bound to endogenous ligands and, for this reason, can provide only information regarding dynamic changes of kinetically labile cations.

To design an MRI probe for the detection of metal cations, binding of the analyte must alter the T_1 relaxation time of water interacting with the Gd(III) contrast agent. Based on this premise, Meade and co-workers successfully designed the first Ca(II)-responsive contrast agent, **15**, for MRI imaging.[226] As illustrated in Figure 6, binding of Ca(II) results in a rearrangement of the coordination sphere around

Gd(III), which increases the relaxivity of water due to the additionally available binding sites. Upon saturation with Ca(II), the relaxivity increased from 3.23 to 5.76 mM^{-1} s^{-1} but showed minimal changes in the presence of Mg(II) or with pH fluctuations around physiological conditions. This design principle spurred subsequently the development of numerous probes for the detection of biologically important metal cations, including K(I), Mg(II), Ca(II), Zn(II), and Cu(II), as reviewed in the following section.

4.1. Magnesium, Potassium, and Calcium

Also based on a BAPTA chelating unit, Dhingra et al. designed an extracellular Ca(II) probe with Ca(II) stability constants ranging between log $K = 1.9$ and 2.7.[227] The probe exhibited an approximately 50% increase in relaxivity in the presence of Ca(II) in a medium that resembled extracellular brain fluid. The reversibility of binding was demonstrated by addition of EDTA, which sequestrated Ca(II) thereby reducing the relaxivity to the initial value of the free probe.[228] The EDTA- and diethylenetriaminepentaacetic acid-derived Gd(III) complexes **16** and **17** (Chart 3) showed a modest increase in relaxivity in the presence of Ca(II), an observation that was ascribed to an increase in hydration number as well as a Ca(II)-induced rigidification of the complex.[229] Hifumi et al. modified the Gd(III)-chelating unit with either a bis-15-crown-5 ether moiety (**18**) for potassium sensing or a charged β-ketoacid (**19**) for the detection of Mg(II) or Ca(II). The compounds exhibited a decrease in longitudinal relaxivity resulting from a change in the second hydration sphere of the Gd(III) complex. Binding followed a 1:1 stoichiometry with a log K of 3.2 for K(I) in the case of KMR-K1 (**18**) and 2.33 and 1.91, respectively, for Mg(II) and Ca(II) in the case of KMR-Mg (**19**).[230]

4.2. Zinc

Hanaoka et al. modified a Gd(III)-diethylenetriaminepentaacetic acid complex with dipicolylamine moieties to construct the Zn(II)-responsive MRI contrast agent **20**, which expressed a decrease of the longitudinal relaxivity upon the addition of Zn(II).[231] A modified design, **21**, where one of the pyridine groups was replaced with a carboxylate, showed a similar selectivity toward Zn(II).[232] Meade and co-workers developed the Zn(II)-responsive contrast agent **22**, which produced an increased relaxivity upon saturation with Zn(II). In analogy to their original design,[226] coordination of the acetate groups to Zn(II) promoted the binding of water to the Gd(III) ion and thus an approximately 2-fold increase of the relaxivity for the dinuclear Gd(III)−Zn(II) complex. With a Zn(II) dissociation constant of 0.2 mM, the probe should be suitable to detect Zn(II) concentrations as low as 100 μM.[233,234] Based on a porphyrin ligand platform, Lippard and co-workers designed a Zn(II)-responsive dual fluorescence and MRI probe (**23**). In its metal-free form, the probe can be used for the fluorescence detection of cellular Zn(II), whereas the Mn(III)-loaded form (**23**) turns into a MRI probe.[235] Zn(II)-binding induced a decrease in longitudinal and an increase in transverse relaxivity. A europium-based paramagnetic chemical exchange saturation transfer agent (**24**) (PARACEST) was also studied for the selective sensing of Zn(II) ions.[236]

4.3. Copper

Inspired by the design of the original Ca(II) probe by Meade and co-workers, Que et al. developed the MRI probe **25** for the selective detection of Cu(II) with micromolar sensitivity. Upon saturation with Cu(II), the longitudinal relaxivity increased from 3.76 to 5.29 mM^{-1} s^{-1}.[237] To improve the copper selectivity, the probe was further modified by tethering thioether receptors to Gd(III)−DO3A core via a pyridyl spacer. The modification resulted in increased selectivity, sensitivity, and turn on response, the best being CG2 (**26**) and CG3 (**27**), which exhibited a relaxivity change from 1.5 to 6.9 mM^{-1} s^{-1}.[238]

The design of MRI probes clearly represents a challenging exercise in coordination chemistry. While numerous creative solutions have been described for achieving substantial relaxivity contrasts, only a few reports describe the MRI detection of metal cations in cell culture. The dynamic in vivo imaging of labile cation fluxes has not been demonstrated yet and presumably poses additional challenges regarding the membrane permeability, biodistribution, and toxicity of these reagents.

5. Microprobe X-ray Fluorescence Imaging Techniques

X-ray fluorescence (XRF)-based imaging techniques rank currently among the most sensitive imaging modalities for detecting trace elements in biological samples with submicrometer resolution.[6,239−242] These methods rely on the direct excitation of the core−shell electrons of atoms, which subsequently relax with emission of photons. Because the emitted X-ray energy depends on the nuclear charge, the elemental composition of a sample can be precisely identified and quantified. Depending on the mode of excitation, XRF analytical techniques can be categorized into three different classes: electron beam, proton beam, and X-ray (photon) beam methods, each of which offers its own set of advantages and disadvantages. After a brief description of the physical principles and instrumentation of each ionization mode, the following sections offer an overview of a broad spectrum of biological questions that have been addressed with these microanalytical imaging techniques.

5.1. Physical Background and Instrumentation

5.1.1. Electron Beam Microprobe Methods

Scanning electron microscopes (SEM) and scanning transmission electron microscopes (STEM) are commonly equipped with an energy dispersive X-ray detector, thus directly enabling electron probe X-ray microanalysis (EPXMA or EPMA) of frozen or freeze-dried cryosectioned specimens.[243] Because EPXMA can be combined with SEM or STEM within a single instrument, the technique is particularly suited to correlate elemental distributions with the morphology and ultrastructure of cells and subcellular structures. By using a focused beam of high-energy electrons, typically ranging between 5 and 30 keV, individual atoms in the specimen are nondestructively ionized and produce an X-ray emission spectrum that directly reflects the elemental composition within the excitation volume. By a scan of the electron probe in a raster pattern across the specimen, images showing the distribution of each element are obtained. While the electron probe diameter typically ranges between 1 and 10 nm, the spatial resolution of EPXMA is significantly

Chart 3

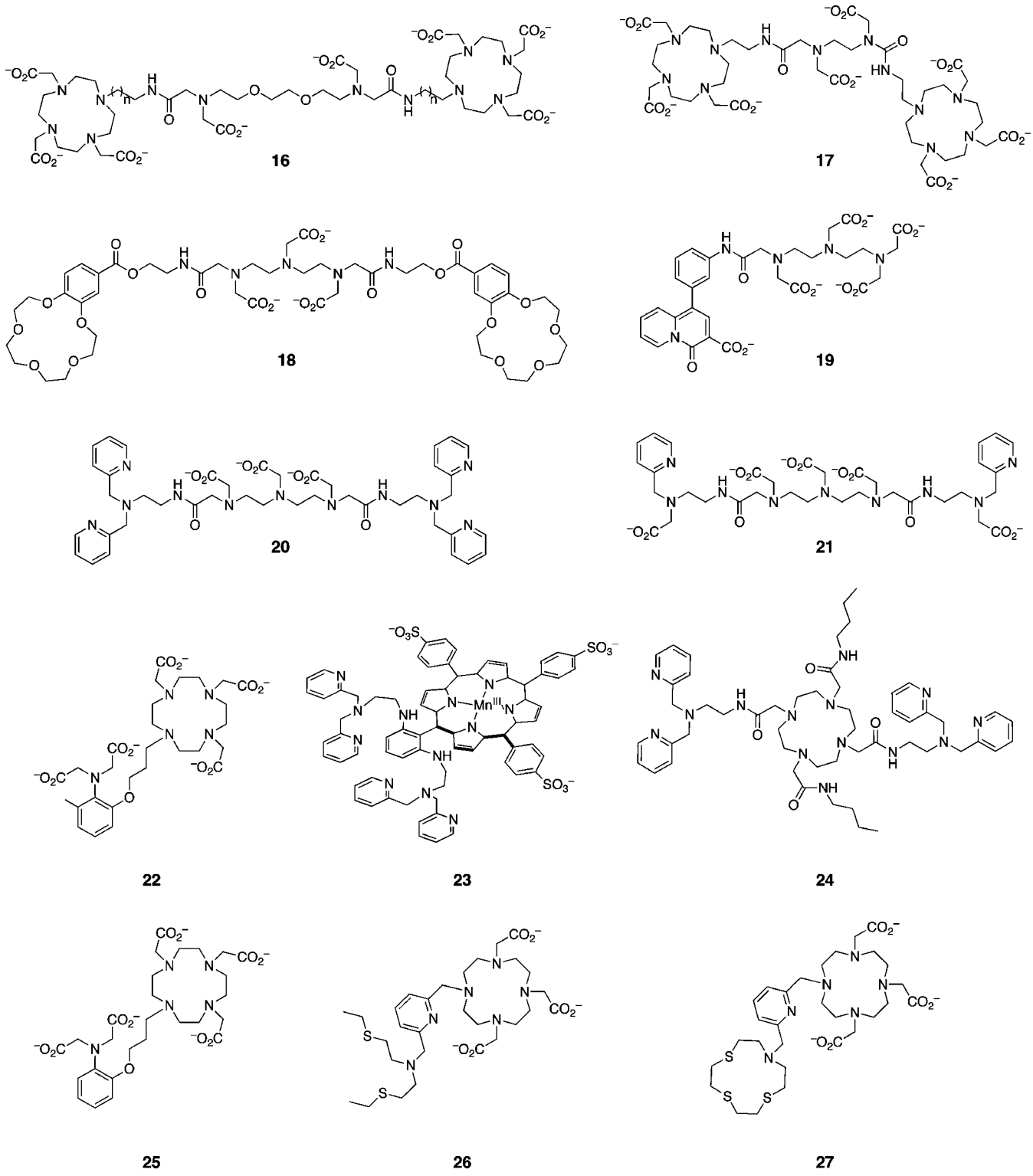

lower due to scattering of the electron beam. As the incident electrons enter the specimen, energy is dissipated through a range of different interactions with bound electrons and the lattice, a process that is commonly referred to as inelastic scattering. Because the individual energy losses are small, the electrons still induce the production of the characteristic X-rays and only gradually decelerate as a function of travel distance. At the same time, the path length of the emitted photons is generally much longer compared with the incident electrons, such that they have a good probability to leave the specimen and reach the detector. For this reason, the probe excitation volume for EPXMA is much larger than the size of the incident electron beam, and as a consequence, the spatial resolution is significantly decreased compared with SEM. In principle, the technique is suitable to simultaneously detect all elements heavier than C with a maximum spatial resolution of 30−40 nm; however, in thick specimens, electron scattering is greatly increased, which results in much larger excitation volumes of several micrometers up to 10 μm.[244] The detection limit of EPXMA of thin sections ranges between 100 and 1000 μg/g, which corresponds to a sensitivity in the low millimolar concentration range.[245] By

use of appropriate standards and application of matrix corrections, accuracies of typically 3−5% or better can be achieved. Despite the relatively low sensitivity, the technique is well-suited to study the localization of many of the biologically important diffusible elements such as Na, Mg, K, Cl, and Ca.[244,246] To preserve their physiological distributions, specimens are fixed through rapid immersion freezing, typically followed by freeze-drying. The removal of water not only reduces radiation damage but also increases the portion of the biologically relevant elements over the dry mass matrix and thus the detection sensitivity.[245] In contrast, EPXMA of low-abundance trace metals such as copper or cobalt in thin sections is more challenging and requires X-ray microanalytical methods with greater sensitivity as discussed in the following sections.

5.1.2. Proton Beam Microprobe Methods

Proton microprobe methods use a proton beam, usually in the 2−4 MeV range, generated by a small accelerator and focused by either electric or magnetic fields to attain elemental distribution maps of samples.[247] The essential components of the proton microprobe setup comprise a scanning system, an irradiation chamber, where several detectors and devices can be connected, and adequate data collection modules. The most common proton beam method is based on particle-induced X-ray emission (PIXE),[248] which is often combined with Rutherford backscattering spectrometry (RBS) and scanning transmission ion microscopy (STIM) for quantitative elemental analyses and identification of structural features within the sample.[249] RBS relies on measuring the energy of protons backscattered by atomic nuclei,[249] which allows for determining the organic composition (C, N, and O) of the sample, and thus permits the simultaneous detection of both low and high atomic number (Z) elements when combined with PIXE.[250] RBS imparts the opportunity to separate the atomic masses of elements present and to determine their profile distribution as a function of the energy detected at a sensitivity of a few atom percent for low Z elements and <100 ppm for high Z elements. STIM uses the energy loss of protons passing through the sample to produce structural images based on variations occurring in the electron density of the sample, thus enabling 3D reconstruction of sample images. STIM allows quantitative elemental mapping of samples while producing highly resolved structural images.[247]

Achieving penetration depths up to 100 μm with average beam diameters of 1 μm, proton beams are well-suited for acquiring quantitative elemental distribution maps of biological samples, including whole cells and tissue sections, thus offering enhanced sensitivity over electron microprobe methods.[247] PIXE is a multielemental technique with particularly high sensitivity (1−10 μg/g) for elements $20 < Z < 35$ and $75 < Z < 85$,[251] thus effectively covering all biologically relevant elements as well as elements commonly employed in labels and metallopharmaceuticals. The emitted X-rays are typically analyzed by an energy-dispersive silicon drift detector, which can be operated at room temperature,[252] and the resulting intensities may be converted to elemental concentrations.[253] Because the physical processes involved in generating the X-ray emission are well understood, PIXE analyses do not require standards for quantitative elemental imaging. Spatial resolutions of 200−300 nm are commonly achieved with a PIXE−RBS setup,[254] although a resolution down to 50 nm has been realized with a STIM setup at the Research Centre for Nuclear Microscopy, National University of Singapore.[255] PIXE thus offers a number of advantages over electron probe methods, including the ability to simultaneously detect over 20 elements at a sensitivity enhanced up to 100-times that of EPXMA with essentially no background contributions and no major sample preparation requirements.[256] Furthermore, unlike EPXMA, PIXE maintains the capacity to obtain fully quantitative elemental distribution maps when combined with RBS and STIM, making it particularly attractive for analyzing biological samples at high spatial resolutions.[256]

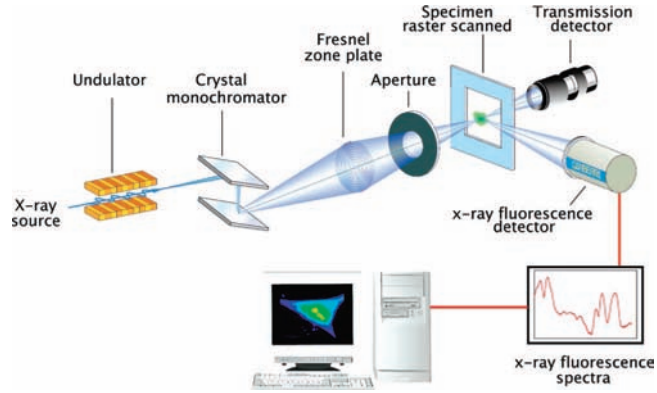

Figure 7. Schematic diagram illustrating the components of an X-ray fluorescence microscope. A crystal monochromator is used to select the energy of the incident X-ray beam, which is focused with a Fresnel zone plate on the specimen. The emitted X-rays are collected with an energy-dispersive detector, thus allowing for simultaneous multielement analysis. Raster scanning across the specimen area yields then quantitative elemental maps, as illustrated on the computer monitor. The purpose of the transmission detector is to help orient the sample on the scanning stage. Reprinted with permission from ref 240. Copyright Elsevier 2007.

5.1.3. X-ray Beam Microprobe Methods

Instead of using a proton beam for producing the excited atomic state, synchrotron X-ray fluorescence microprobes (SXRF or microXRF) rely on spatially coherent high-brilliance X-rays as excitation source. Like PIXE and EPXMA, SXRF uses the detection of the emitted X-rays to achieve spatially resolved elemental distribution maps. The transition energies associated with electronic relaxation are equal to the difference between the inner and outer shell binding energies specific for individual elements. The number of X-ray photons emitted scales directly as a function of atomic abundance, thus allowing for a straightforward determination of individual element quantities. Recent advances in X-ray optics permit focusing of hard X-rays down to 30−150 nm spot sizes, using either a Kirkpatrick−Baez mirror system,[257−259] refractive lenses,[260−262] or a Fresnel zone plate.[263] Raster scanning of the specimen and acquisition of the entire X-ray spectrum yields spatially well-resolved, quantitative topographical maps for a wide range of elements, including most biologically relevant transition metals (Figure 7). Hard X-ray microprobes offering submicrometer resolution have been developed at the Advanced Photon Source (APS, Argonne National Laboratory, Chicago, IL), the European Synchrotron Radiation Facility (ESRF, Grenoble Cedex, France), and Spring-8 (RIKEN, Hyogo, Japan). For example, the instruments at APS use a crystal monochromator to select the energy of the incident photons, which are then focused with a Fresnel zone plate as focusing device to produce an excitation spot of less than 0.15×0.15 μm^2.

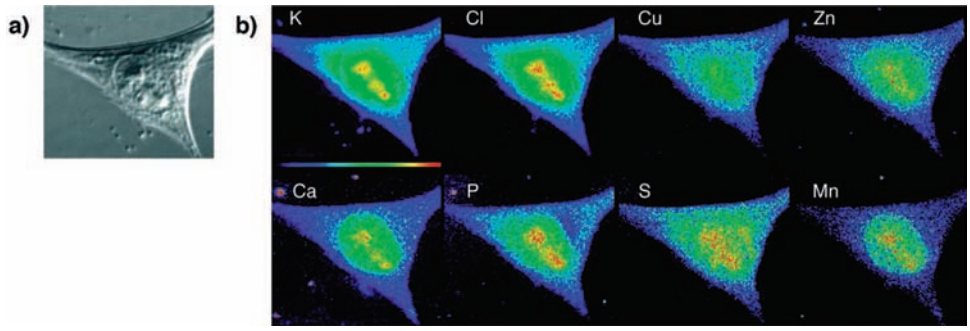

Figure 8. MicroXRF imaging of mouse fibroblast cells grown on 200 mesh EM gold grids coated with a Formvar-carbon thin film: (A) DIC image of in-air-dried cell; (B) raster-scanned microXRF topographical maps for selected elements (excitation at 10 keV, pixel size 0.3 μm, integration time 1 s/pixel). Reprinted with permission from ref 265. Copyright Elsevier 2006.

The emitted X-rays are analyzed with an energy-dispersive detector with detection limits ranging from 5×10^{-20} to 3.9×10^{-19} mol/μm^2, which corresponds to a few thousand atoms within an irradiated spot.[264]

By offering a penetration depth of up to 1000 μm and routine spatial resolutions down to 100 nm, synchrotron radiation induced X-ray fluorescence imaging (SXRF) is especially useful for analyzing biological specimens.[6,239−242] For example, the analysis of individual whole cells is possible without the need for cryosectioning. As illustrated with the analysis of a NIH 3T3 mouse fibroblast cell (Figure 8), a single raster scan with an incident X-ray energy of 10 keV simultaneously produced quantitative maps with subcellular resolution for selected biologically relevant elements.[265] Adherent cells can be directly grown on X-ray fluorescence compatible substrates such as Formvar-carbon films[266,267] or silicon nitride (Si_3N_4) windows.[268] Viability studies with mouse fibroblast cells grown on these ceramics showed neither cytotoxic effects nor morphological changes.[269] To improve cell adherence, commercially available windows are best pretreated with 0.01% polylysine solution.[265]

The absorption of hard X-rays is not only characteristic for a specific element but also the element oxidation state and local coordination environment. Biological X-ray absorption spectroscopy (XAS) has evolved into an invaluable tool to characterize the structure and function of metal sites in metalloproteins.[2,270] While the technique is routinely applied in transmission mode to characterize purified metalloproteins, typically as bulk samples at millimolar concentrations, XAS spectra can be also acquired in fluorescence mode by scanning the incident photon energy across the X-ray absorption edge (XANES) of the element(s) of interest and collecting the emitted photons. By using a submicrometer-focused synchrotron photon beam as excitation source, the technique offers sufficient sensitivity to perform XANES in situ at specific subcellular locations, thus providing valuable insights into the speciation of biological metal ions in their native environment.[271] Given these advantageous features, it is not surprising that X-ray microprobe methods have contributed to numerous research studies in geochemistry, cosmochemistry, environmental science, materials science, and, more recently, biology and medicine.

5.2. Metal Ions in Various Diseases and Medical Conditions

5.2.1. Cancer Diagnosis and Disease Progression

The development of various types of cancer is directly associated with the age-related accumulation of oxidative damage to DNA, proteins, and lipids induced by reactive oxygen species (ROS).[272] Both redox- and non-redox-active metals participate in the generation of ROS under metal excess and limiting conditions or in cases of genetically linked disturbances of metal homeostasis. Thus, significant research efforts were devoted to elucidating the distribution and speciation of metals in cancer development and progression.

5.2.1.1. Angiogenesis and Cancer Progression. Angiogenesis is a physiological process that leads to formation of new blood vessels from existing vasculature. While angiogenesis is vital to normal growth and development, it plays a particularly critical role in tumor development.[273] Because tumor progression is limited without adequate supply of oxygen and nutrients through the host vascular system, the suppression of angiogenesis has evolved as an important target for cancer treatment strategies. The depletion of copper has been shown to inhibit angiogenesis in a broad range of cancer types; however, the underlying reasons for the copper sensitivity remain elusive.[274] To gain insights into the role of copper in angiogenesis, Finney et al. utilized X-ray fluorescence microscopy to image cellular copper stores in microvascular endothelial cells. These experiments revealed a massive relocalization of copper from intracellular compartments to the tips of cell filopodia and across the plasma membrane.[275]

5.2.1.2. Breast Cancer. Breast cancer is the most common form of cancer in Western women.[276] Farquharson and coworkers applied SXRF to investigate the quantity and spatial distribution of trace metals in breast tissue slices with primary invasive ductal carcinoma.[277−279] The studies revealed an increase in all measured metal concentrations, particularly for Zn and Cu, in the tumor areas of the studied samples. Further analysis of the X-ray absorption near-edge structure (XANES) indicated that Cu is present as a mixture of its monovalent and divalent oxidation states, for both normal and cancerous tissue.[279] Interestingly, the data suggested that the cancerous tissue contains a higher fraction of Cu(I) compared with normal tissue. Additionally, SXRF analysis of the metal distributions revealed a similar pattern for Ca, Cu, P, S, and Zn, while Fe maintained a uniquely different distribution.[278] Similar results were obtained in two independent studies that used SXRF to elucidate quantitative metal distributions in breast carcinoma tissue samples.[280,281] The results indicated also increased amounts of Ca, Cu, and Zn in areas of the cancer clusters and a different spatial distribution for Fe compared with Ca, Cu, and Zn. A combined X-ray fluorescence microtomography (XRFCT) and X-ray transmission microtomography (CT) system was

implemented at the Brazilian Synchrotron Light Source (LNLS) and applied to investigate the spatial distribution of Zn, Cu, and Fe in breast cancer tissue samples.[282−285] Cylindrically shaped tissue samples with 1.5−2 mm thickness were scanned over 180° with a beam focused to 200 μm. Although tissue self-absorption prevented the acquisition of quantitative elemental information, tomographic reconstructions revealed the qualitative 3D distribution of Fe, Cu, and Zn.

5.2.1.3. Prostate Cancer. Despite substantial efforts in screening and early detection, prostate cancer is still the most common noncutaneous human malignancy and is the second most lethal tumor among men.[286] The concentration of zinc in human prostate tissue is higher compared with any other soft tissue in the body,[287] and there is compelling evidence suggesting that altered prostate zinc homeostasis is an important factor in the development of prostate malignancy.[288] To investigate the potential causal effects of Zn in prostate cancer development and progression, SXRF was utilized to image the distribution of Zn in malignant tissue versus control samples.[289] The study revealed significantly lower amounts of Zn in cancerous tissue compared with normal tissue and striking differences in the correlation of Zn and Ca densities, suggesting that Ca might play a significant role in the ability of the cell to accumulate Zn.

5.2.2. Anticancer Drugs

Although cisplatin is one of the most widely used metallopharmaceuticals for cancer treatment;[290] its clinical application is limited by dose-associated toxic side effects and increasing resistance of various cancer cell types. Conversely, the kinetic inertness and thus increased stability of Pt(IV) drugs offer ways to overcome some of the difficulties associated with Pt(II)-based drugs.[291] Hence, the characterization of the uptake and biodistribution of metal-based anticancer drugs is critically important for understanding and minimizing the underlying toxicity.[290] In this context, XRF methods have provided already a wealth of information regarding the spatial distribution of metal-based drugs in both cellular and animal models.

5.2.2.1. Platinum-Based Anticancer Drugs. The intracellular distribution of cisplatin and other platinum-based anticancer compounds has been the focus of several studies, including a PIXE analysis of human lung cancer and ovarian adenocarcinoma cell lines[292,293] and the SXRF analyses of human head and neck squamous carcinoma (SQ20B) cells,[294] as well as human ovarian cancer (A2780) cells.[295,296] The reports uniformly demonstrated that Pt was localized predominantly within the nucleus. Furthermore, X-ray absorption near-edge spectra confirmed intracellular reduction of Pt(IV) drugs to Pt(II) upon entering the cells,[296,297] thus supporting a reductive activation mechanism for this type of anticancer drugs. Another set of investigations focused on elucidating the inorganic physiology of cisplatin resistance developed by a number of cancer cell types. For example, an SXRF study of the platinum distribution in human ovarian adenocarcinoma cells treated with cisplatin or other platinum-based drugs revealed a 50% decrease in Pt uptake by the drug-resistant compared with nonresistant cells.[298] To unravel the mechanism of drug resistance in melanomas, one of the most aggressive forms of cancer, Chen et al. studied the sequestration of cisplatin in epidermoid carcinoma cells using SXRF. Drug-resistant cells accumulated Pt preferentially in melanosomes, which appeared to contribute significantly to multidrug resistance through increased melanosome-mediated drug export.[299] Most recently, Alderen et al. demonstrated for the first time that X-ray fluorescence tomography is suitable to visualize the three-dimensional distribution of Pt drugs in multicellular tumor spheroids.[300] Radial distribution profiles of the tomograms revealed limited penetration into the tumor with higher accumulation of Pt in cells closer to the surface. No significant differences between Pt(II)- and Pt(IV)-based drugs were observed.

5.2.2.2. Non-Platinum-Based Anticancer Drugs. In addition to platinum-based drugs, several other transition metal complexes have been shown to be effective against various cancers.[301] For example, metallocene sandwich complexes of the type Cp_2MCl_2 composed of the cyclopentadienyl anion (Cp^-) and various transition metals, including Mo, Nb, Ti, and V, have shown antitumor activity. Chinese hamster lung cells treated with Cp_2MoCl_2 or Cp_2NbCl_2 revealed striking differences in the subcellular localization of the drugs. While the SXRF Mo map showed a broad cellular distribution with some nuclear localization, the Nb drug appeared to localize in hot spots throughout the cell.[302] Consistent with earlier studies, the SXRF data implied distinctly different uptake and targeting mechanisms to be responsible for the cytotoxicity of the metallocene complexes.

Similar to Pt(IV), kinetically inert Co(III) complexes might be suitable as hypoxia-activated pharmaceuticals in cancer treatment.[303] Resistance to chemotherapeutic agents is mainly found in tumor cells that grow under anaerobic conditions. Under these conditions, Co(III) complexes might be reduced to the corresponding labile Co(II) species, followed by dissociation of a cytotoxic ligand.[304] Bonnitcha et al. assessed the fate of various Co(III) complexes in human ovarian carcinoma cells based on changes in XANES spectra.[305] Because the X-ray absorption near-edge structure of Co complexes is very sensitive to changes in the coordination shell, reliable oxidation state assignments based on XANES are difficult to achieve.[306] Nevertheless, the XANES spectra indicated changes in the coordination environment, implying intracellular reduction of some of the complexes.[305]

While the metalloid arsenic (As) is responsible for mass poisonings associated with contaminated drinking water, at the same time, its toxicity has been exploited in the antileukemia drug Trisenox (As_2O_3).[307] Patients treated with Trisenox showed As accumulation in hair localized at the periphery.[308,309] In an effort to understand details behind the mechanism of Trisenox toxicity, HepG2 cells were exposed to high doses of arsenite (1 mM) or arsenate (20 mM) and subsequently imaged by SXRF.[310] The thin-sectioned cells showed As accumulation in the euchromatin region of the cell nucleus, suggesting that As was targeting the DNA or proteins involved in DNA transcription. From XANES and EXAFS spectra of bulk cell samples, it was concluded that As was predominantly present as a trisulfur species.[310]

5.2.3. Neurodegenerative Diseases

The central nervous system (CNS) is comprised of the brain and spinal cord and functions as the body's information gatherer, storage center, and control system.[311] While the brain serves as the center for cognitive and motor function, the spinal cord communicates messages from the body to the brain and vice versa. Although the brain accounts for only 2% of the total human body mass, it consumes 20% of the oxygen absorbed through respiration. Compared with other regions of the body, the brain contains also significantly

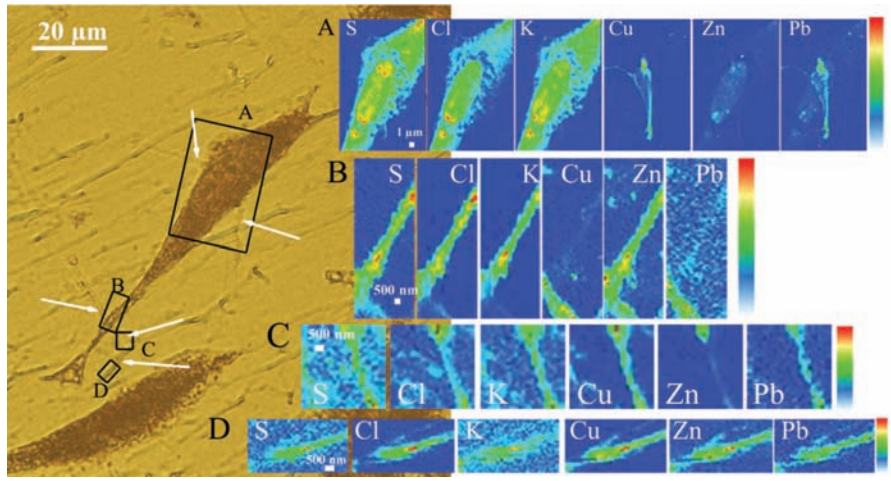

Figure 9. SXRF elemental imaging of neurites with submicrometer resolution.[317] Left panel shows an optical image of PC12 cells after cryofixation and freeze-drying. Cells were cultured with 300 μM iron during 24 h and treated with NGF. The black squares show the areas analyzed by synchrotron nanoprobe X-ray fluorescence. White arrows show thin neurite-like processes. Right panels show X-ray fluorescence images of chemical elements in the cell body (A), in the main ramification (B), and in thin neurite-like processes (A, B, C, D). The color scale bar indicates intensity of X-rays, which increases from blue to red.

higher concentrations of metal ions.[312,313] It is therefore not surprising that many neurological disorders are associated with metal imbalance in the nervous system.[4,314] While the accumulation of redox active transition metal ions is believed to induce oxidative stress through generation of free radicals,[272] the relationship between metal ion imbalance and the pathology of neurological disorders remains largely elusive. Synchrotron radiation based imaging techniques offer new opportunities to visualize and quantify transition metal ions at the subcellular level, and thus may greatly help in unraveling the role of metal ions and their speciation in neurobiology.[315]

5.2.3.1. Neuronal Processes. Early PIXE studies of different brain regions of individuals without neurological disorders pointed toward an important relationship between the trace element profile of a brain structure and its function.[316] The small size of individual neurites, thin tendrils growing from neurons, poses significant challenges for imaging elemental distributions with subcellular resolution. By focusing the synchrotron radiation with two elliptically shaped mirrors in Kirkpatrick−Baez geometry, an exceptional spatial resolution of 90 nm was recently achieved with the nanoprobe at the European Synchrotron Radiation Facility (ESRF).[317] Rat pheochromocytoma (PC12) cells were used as an in vitro model of dopaminergic cells to study changes in metal distribution upon nerve growth factor (NGF) stimulated differentiation. While P, S, Cl, K, and Zn were distributed quite uniformly throughout the cells, Fe was excluded from the nucleus and localized in granular dopamine vesicles. Upon differentiation, the generated neurites accumulated substantial amounts of Cu, Zn, and Pb (Figure 9).[317] In a similar SXRF study by the same authors, dopaminergic cells were shown to accumulate Fe within dopamine-containing vesicles, while inhibition of dopamine synthesis resulted in decreased vesicular storage of Fe.[318]

Reinert et al. utilized micro-PIXE to investigate the elemental composition of perineuronal nets (PNs), a specialized extracellular matrix (ECM) implicated in scavenging redox-active transition metals to protect neurons against oxidative stress.[319,320] Upon exposure to excess Fe, the PNs of 6 μm rat brain tissue sections accumulated more Fe compared with any other ECM component. Further Mössbauer spectroscopic investigations revealed that the Fe was bound in its trivalent oxidation state to the PNs.[321] Neuromelanin, a dark colored pigment synthesized within specific catecholamine-producing neurons in the human brain, is also believed to play a role in metal binding and radical scavenging. SXRF analysis of neuromelanin in substantia nigra tissue sections displayed higher metal concentrations in mature compared with developing brain samples.[322] High-resolution spatial distribution maps revealed Fe-rich microdomains that colocalized with S, Ca, Cu, Zn, and Se in an age-dependent manner. Micro-XANES analysis of Fe localized in these microdomains were characteristic of Fe(III) and paralleled the spectral signature of ferritin.[322]

5.2.3.2. Parkinson's Disease (PD). Parkinson's disease (PD) is the second most common neurodegenerative disease, affecting more than four million people.[323,324] Entailing loss of motor and sensory functions, as well as memory impairment, the pathological hallmark of this disorder is a pronounced reduction of dopaminergic neurons from the substantia nigra (SN) resulting in decreased dopamine production within the basal ganglia.[324] While there is contradicting evidence that direct occupational exposures to metals poses a risk factor for PD,[325] several studies have shown alterations in Cu and Zn homeostasis and accumulation of Fe within the SN.[326,327] In an effort to unravel details of altered metal homeostasis in PD, a number of investigations have applied SXRF imaging to quantitatively assess changes in the distribution of Fe, Cu, and Zn within Parkinson's disease models compared with control cases.

Three different ion beam techniques, particle-induced X-ray emission (PIXE), backscattering spectrometry (BS), and scanning transmission ion spectrometry (STIM) were combined to accurately quantify Fe accumulation in dopaminergic cells.[251] The data indicated an interaction between Fe and dopamine within neurotransmitter vesicles and underscored the importance of Fe in promoting neurodegeneration in Parkinson's disease. In a similar study, PIXE, RBS, and STIM were applied to analyze metal distributions within the SN of brain tissue sections from both old and young monkeys.[328] With increasing age, Fe accumulated in the form of iron-rich deposits within specific regions of the SN. Another set of investigations employed PIXE and rapid-scanning SXRF to quantitatively image differences in metal distributions of brain tissue slices from PD and control

patients.[329−331] In agreement with earlier findings, the scans revealed pronounced increases in the total amount of Fe present within regions of the midbrain and SN of PD patients.

Transgenic mice carrying knockouts in the two iron regulatory proteins, IRP1 and IRP2, develop a progressive neurodegenerative disease that resembles the features of human PD.[332] Histochemical investigations indicated high levels of ferritin in axonal tracts of the knockout mice. The direct 3D visualization of ferritin by electron tomography revealed an even more detailed picture with excess ferritin being localized to vesicular compartments inside the axon in the form of invaginations within the oligodendrocyte cells.[333] At the same time, ferritin was surprisingly absent from axons of degenerating neurons, suggesting that ferritin trafficking was compromised at early stages during pathogenesis.

A series of investigations focused also on elucidating changes in the oxidation state and speciation of Fe in PD pathogenesis. An SXRF/XANES study of brain tissue sections from PD primate models showed that Fe accumulated within neuromelanin granules in its divalent oxidation state.[334] In an earlier investigation of human brain tissue sections of PD patients, a similar accumulation of Fe in neuromelanin granules was found; however, the XANES data implied a shift toward its trivalent oxidation state.[335] Although the data from these reports appeared somewhat conflicting, they nevertheless implied that changes in Fe distribution and speciation play an important role in PD progression. While neuromelanin may function as protector against free radicals by scavenging potentially toxic metal ions (section 5.2.3.1), it has been also speculated that the pigment may potentiate free radical production in the presence of excess redox-active metals. A PIXE study of the metal ion distribution and contents in neuromelanin containing neurons showed no differences between the iron concentrations for PD and those of control tissue samples.[336]

According to recent SXRF studies, transition metals other than Fe may also contribute to PD pathogenesis.[337−340] For example, abnormal accumulation of Cu and Se was found inside neurons of the SN of human brain tissue sections from PD patients.[338] No differences in the speciation of copper between PD and control samples were found in a recent XANES microbeam study.[340] The data suggested that the bulk of copper inside SN neurons is coordinated in a tetrahedral environment in its divalent oxidation state. In a comparative study of SN from tissue representing PD, amyotrophic lateral sclerosis, and control cases, Chwieji et al. found that areas of high Zn content correlated with the location of the SN neuron bodies, while Br levels within the white matter of the SN were slightly elevated.[339] Multivariate cluster analysis of SXRF data confirmed significant differences in trace metal accumulation in SN of brain tissue from PD patients compared with either amyotrophic lateral sclerosis patients or a control group.[339]

5.2.3.3. Alzheimer's Disease (AD). Alzheimer's disease (AD) is the most common form of senile dementia and affects approximately 26 million people worldwide.[341] AD manifests gradually with progressive and irreversible cognitive decline first experienced in the form of memory impairment at the early stage of the disease and a decline of motor and sensory functions at later stages. From studies of postmortem AD brains, the pathology of AD progression is characterized by an accumulation of insoluble Aβ amyloid peptides (Aβ), neurofibrillary tangles, neuropil threads, and neuronal losses. An increasing body of literature indicates that Aβ amyloid formation is central to AD pathogenesis.[342] Furthermore, abnormal interactions of Aβ with neocortical metal ions, especially Zn, Cu, and Fe, might play an important role in amyloid formation and toxicity.[343,344]

While early reports on metal imbalance in AD pathogenesis were limited to elemental analysis of bulk autopsy samples,[345,346] more recent X-ray-based imaging investigations added critical information regarding the spatial distribution of trace elements in specific regions of the brain.[347] Lovell et al. utilized micro-PIXE to quantify the amount of Cu, Fe, and Zn levels at a spatial resolution of 5×10 μm^2 in neuritic plaques and surrounding neuropil in the amygdala of AD patients.[348] Compared with a group of age-matched control patients, Zn, Cu, and Fe were significantly elevated in the AD neuropil, and even higher concentrations were found within the plaques. A recent PIXE analysis was combined with STIM and RBS ion beam techniques to accurately quantify the Zn, Cu, and Fe levels in unstained, freeze-dried brain sections of a transgenic AD mouse model (CRND-8).[349] In agreement with the earlier study, the data revealed a 2- to 3-fold increase of the Zn, Cu, and Fe level compared with surrounding tissue. Ishihara et al. explored the utility of SXRF to analyze the intraneural elemental composition in brain tissue from AD patients.[350] The study revealed a correlation between Zn and Ca levels over a large concentration range. To improve the reliability for SXRF imaging of the distribution of metal ions in small amyloid plaques, brain tissues were processed by laser capture microdissection (LCM), a lesion-specific tissue procurement technique.[344] This approach has the advantage that small tissue pieces can be analyzed, thus improving the elemental quantitation by minimizing the background from surrounding tissue.

The combination of different imaging modalities is particularly advantageous for simultaneously identifying the location and analyzing the elemental composition of AD plaques and brain tissues. For this purpose, Miller et al. integrated an epifluorescence module within a SXRF microprobe beamline and directly identified metal accumulation within Thioflavin S stained AD plaques with a precision of 2−5 μm.[351] To circumvent histochemical staining of the specimens, a process that might introduce artifacts, synchrotron Fourier transform infrared microspectroscopy (FTIRM) was combined with an SXRF microprobe.[352] Amyloid plaques are associated with an elevated β-sheet content, which can be identified by FTIRM on the basis of the characteristic amide absorbance around 1630 cm^{-1}.[353] The study demonstrated a strong correlation between an elevated β-sheet content in AD plaques and the accumulation of Cu and Zn in "hot spots", thus strongly supporting the association of metal ions with amyloid formation in AD. In a recent study, susceptibility weighted magnetic resonance images (SWI) were correlated with SXRF Fe maps of brain tissue from a transgenic mouse model for AD (tgCRND8).[354] Furthermore, the combination of high-resolution transmission electron microscopy (HR-TEM), energy-dispersive X-ray spectroscopy (EDX), electron energy-loss spectroscopy (EELS), electron tomography, and electron diffraction was used to characterize the iron-rich plaque core in three dimensions.[355] The data indicated the predominant presence of magnetite and maghemite, thus suggesting abnormal Fe biomineralization processes within the plaque and a disruption of the trafficking of the Fe storage protein ferritin.

5.2.3.4. Amyotrophic Lateral Sclerosis (ALS). Amyotrophic lateral sclerosis (ALS) is a fatal progressive neurological disease observed primarily in adults and is characterized by the degeneration of the cortical and spinal motor neurons.[356] A person with ALS initially experiences weakness and spasticity, which continually worsen until death, usually within 3−5 years of the initial diagnosis. Although ALS, like other neurological diseases, is very complex and details surrounding its pathogenesis remain elusive, there is compelling evidence that trace metal ions are central to the processes leading to neurodegeneration.[4,338,357] Initial SXRF studies of the metal topography in human spinal cord tissue sections from ALS patients pointed toward significant increases in the total amounts of Ca, K, Fe, and Zn within motor neuron bodies compared with surrounding tissue,[358,359] thus supporting the potential role for these metals in ALS progression. These findings were confirmed by a later study; however, quantitative analysis indicated that there were no general abnormalities in the elemental accumulation between ALS and control specimens.[360]

5.2.3.5. Menkes and Wilson's Disease. The disruption of cellular copper trafficking is central to both Menkes and Wilson's disease,[361] underscoring the importance of maintaining the delicate homeostatic balance of copper. On the one hand, copper is essential to a multitude of cellular processes, including mitochondrial respiration, antioxidant defense, neurotransmitter synthesis, connective tissue formation, pigmentation, peptide amidation and iron metabolism; on the other hand, copper excess may facilitate the production of reactive oxygen species through Fenton type reactions.[362] Correlative light microscopy and X-ray fluorescence imaging experiments indicated the presence of a labile copper pool in the late Golgi and mitochondria of cultured NIH 3T3 mouse fibroblast cells.[107] The two copper transporting ATPases, ATP7a and ATP7b, are key elements in controlling the overall copper balance in the human body. Mutations in ATP7a or ATP7b disrupt this balance, resulting in copper deficiency as in the case of Menkes disease or copper overload as in Wilson's disease.[363]

Despite the overall copper deficiency in the body, Menkes patients accumulate copper in the kidney. Analysis of the trace element distribution with PIXE in kidney tissue sections of the brindled mouse, a model of Menkes disease carrying homologous mutations, revealed increased copper concentrations within the proximal tubules compared with control samples.[364] Additionally, the Fe distribution appeared nonuniform in both genotypes, with a substantially higher Fe concentration in proximal compared with distal tubules.

In an effort to elucidate the speciation and distribution of tetrathiomolybdate (TTM), a promising copper chelator for treating Wilson's disease,[365,366] Zhang et al. used a combination of X-ray absorption spectroscopy and SXRF imaging to analyze the liver and kidney of a TTM-treated animal model of Wilson's disease.[367] The XAS spectra of TTM-treated rat liver and kidney indicated the presence of three- and four-coordinate Cu(I)−S species. In kidney, most copper appeared to be present as multinuclear Cu−Mo complexes, whereas the liver samples pointed also toward the presence of non-cluster-bound Cu. A pronounced accumulation of Cu was observed in the cortex of the kidney for TTM-treated rats with a high degree of correlation between Mo and Cu. The results were consistent with a mechanism in which copper is bound by TTM in the liver, and then in part mobilized to the kidney.

5.2.3.6. Hereditary Retinal Degeneration. Hereditary retinal degeneration (HRD) is characterized by a progressive deterioration of photoreceptors. Immunohistochemical studies indicated anomalies in the Fe transport protein transferrin in retinas of dystrophic rats. Preliminary PIXE analysis of freeze-dried thin sections of rat retinas from various stages of the disease revealed a high Ca content in the choriocapillaris and retinal pigmented epithelium, strongly contrasting the uniform distribution observed in control retinal layers.[368] While the impetus for these studies was the investigation of Fe distribution, the data analysis was hampered due to difficulties in separating intracellular Fe from heme-Fe in vascularized areas. In two follow up studies, Fe was found to be unevenly distributed throughout the rat retina, with highest concentrations being present in the choroid and retinal pigment epithelium and the inner segments of the photoreceptors.[369,370] The distribution pattern of Fe in the outer retina correlated with the immunolocalization of ferritin.[370] The Fe content increased as a function of disease development. Similar temporal changes were found for Cu, Zn, and Ca, implying potential roles for these metals in the disease progression.

5.2.4. Atherosclerosis and Cardiovascular Disease

5.2.4.1. Atherosclerosis. Atherosclerosis, a systemic disease of medium and large blood vessels, claims more lives in the developed world than all types of cancer combined.[371] Atherogenesis is represented by endothelial dysfunction, vascular inflammation, smooth muscle cell migration to the inner arterial wall (intima), and a buildup of lipids, cholesterol, and cell debris within the intima.[371] Several transition metals, in particular redox-active Cu and Fe, have been implicated as key players in atherogenesis,[372,373] although results concerning the nature of their individual roles have been controversial.[374−376] As previously discussed for diseases involving metal imbalance, noninvasive XRF analysis has been particularly helpful in uncovering relationships between disease progression and abnormal trace element levels.

To explore whether coronary artery wall calcifications start at an early stage of atherosclerosis, Roijers et al. used a combination of proton beam techniques to study the Ca distribution and calcification of entire artery cross sections.[377] The observed Ca/P ratios indeed indicated that the formation of calcium phosphate granules occurs early in atherosclerosis. Furthermore, the implied correlation between increased plasma cholesterol and iron accumulation in human coronary arteries[372] prompted the same authors to analyze the spatial distribution of Fe in lesions of aortic tissue from LDL-receptor-deficient mice, an animal model of atherosclerosis.[378] The results revealed that Fe accumulated in lesions characterized by lipid accumulation and necrotic material compared with Fe present in the fibrous cap and macrophages. Besides Fe accumulation, ICP-MS data also implied the presence of increased Cu levels within human coronary arteries.[372] By combination of PIXE, STIM, and RBS techniques, the spatial distribution of Cu in addition to Fe was analyzed.[379] Similar to the previous study, Fe accumulation was observed within atherosclerotic lesions from New Zealand white rabbits fed on high cholesterol diet for 8 weeks; however, the lesions appeared to be depleted in Cu compared with the adjacent artery walls. In addition, the Cu levels were found to be approximately 30 times lower compared with Fe, suggesting a predominant role for Fe rather than Cu in atherogenesis.

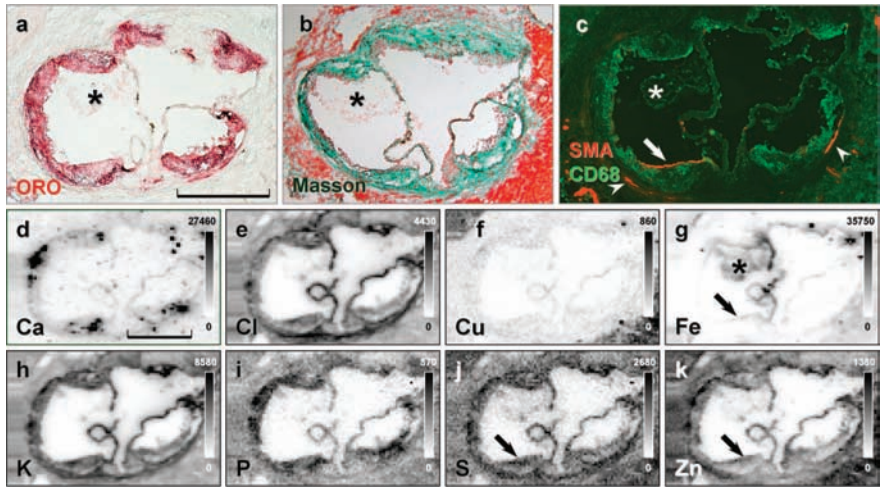

Figure 10. Histochemical and SXRF analysis of atherosclerotic plaques.[384] Consecutive sections of aortic root of apoE/LDLR$^{-/-}$ mouse stained with oil red-O (a) and Masson's trichrome (b) and double-immunostained for smooth muscle actin (red) and CD68 (green) (c). General distributions of calcium (d), chlorine (e), copper (f), iron (g), potassium (h), phosphorus (i), sulfur (j), and zinc (k) obtained by micro-XRF in adjacent section. Atherosclerotic plaques are labeled with oil red-O (a); smooth muscle cells are present in media (c, arrowheads) and in intima (c, arrow). Notice the high accumulation of Fe, S, and Zn in intimal smooth muscle (arrows in g, j, and k). Collagen fibers are stained green in Masson's trichrome (b). A blood clot (asterisk) present in the aortic lumen shows a very high concentration of iron (g). Scale bars = 500 μm. Gray-scale intensity bars show numbers of counts.

Provoked by a shortage of effective treatment and preventative measures and prior observations of low serum levels of Zn in atherosclerosis patients,[380,381] a study using a combination of PIXE, STIM, and RBS focused also on imaging the Zn distribution in atherosclerotic lesions from New Zealand white rabbits.[382] Consistent with previous findings that Fe plays a major role in atherogenesis, the results not only indicated a 7 times higher Fe content in early atherosclerotic lesions compared with adjacent arterial walls but also revealed that Fe chelation successfully stopped atherogenesis. Present at only low levels in lesions, Cu was again suggested to play no significant role in disease progression. Furthermore, Zn was depleted in lesions and also showed an anticorrelation with local lesion development, thus indicating a possible indirect protective effect for Zn.[382] Likewise, PIXE, STIM, and RBS data from an earlier study focusing on Zn and Fe showed the characteristic increase in Fe and decrease in Zn levels in lesions from New Zealand white rabbits,[383] thus further supporting a major role for Fe, potentially through free radical generation, and perhaps a protective role for Zn in atherogenesis.

Despite the fact that trace element content in atherosclerotic plaques has been the subject of many investigations, a comprehensive analysis of the overall elemental composition has been conducted only very recently.[384] For this purpose, SXRF combined with histological staining were applied to investigate the quantitative spatial distributions of multiple elements in lesions from apolipoprotein E and LDL receptor double-knockout (apoE/LDLR$^{-/-}$) mice, an animal model of atherosclerosis.[385] Results showed sulfur in areas occupied by macrophages and smooth muscle cells, while Fe was mostly concentrated in cardiac and smooth muscle, blood clots, and adjacent coronary vessels (Figure 10). Cu existed at higher amounts only in cardiac muscle and was relatively depleted in plaques. Additionally, Ca showed significantly higher levels in mineral deposits, mostly located in the aortic media. Zn, again, was relatively low in lesions but was more concentrated in smooth musculature, in cardiac muscle, and in mineral concretions like Ca. This comprehensive study offered intriguing insights into the morphology-specific elemental speciation of atherosclerotic plaques and may spur further investigations to evaluate possible dietary and pharmacological treatments of atherosclerosis.

ApoE-deficient mice were used to explore whether the ratio of Zn to Fe concentrations might be applied as an indicator of atherosclerosis progression. By applying a combination of PIXE, STIM, and RBS, Minqin et al. determined the quantitative metal distributions in the carotid artery walls of mice fed with a high fat diet.[386] Consistent with the studies described above, the data showed that high concentrations of localized Fe correlated with an increased degree of atherosclerosis, while high levels of Zn were associated with inhibition of the disease. Interestingly, treatment of mice with probucol, a common atherosclerotic drug,[387] resulted in increased Zn levels and Zn/Fe ratio in carotid arteries of ApoE$^{-/-}$ mice.[386]

Given their strategic location between blood and tissue, vascular endothelial cells (ECs) have a large array of physiological functions including cholesterol regulation, lipid homeostasis, signal transduction, immunity, inflammation, and hemostasis.[388] Alterations of endothelial function precede the development of atherosclerotic plaques and contribute to plaque perpetuation as well as to the clinical manifestations of vascular disease.[389] Endothelial dysfunction is characterized by the general inability of ECs to produce nitric oxide under conditions of oxidative stress induced by increased intracellular levels of H_2O_2;[389] however, the effects of increased intracellular H_2O_2 on global metal distributions remains largely unexplored in endothelial cells. To assess the consequences of H_2O_2 exposure on the elemental speciation, SXRF studies were conducted on porcine aortic endothelial cells (PAEC). The data indicated that H_2O_2 exposure resulted in cell membrane damage and significant increases for P, K, Ca, Fe, Cu, and Zn compared with untreated control cells. The enhanced mobilization of metal ions in response to H_2O_2 exposure, mainly from the cell cytoplasm into the extracellular space, might explain the increased levels of metal ions in atherosclerotic plaques.[390]

5.2.4.2. Cardiovascular Disease. Atherosclerosis ultimately results in coronary artery disease (heart attack) or cerebrovascular disease (stroke), collectively termed cardiovascular disease, because of lesion disruption and a conse-

quent decrease in blood flow to the heart and the brain.[371] A large body of research implies that transition metal ions, particularly Fe, Cu, and Zn, play a major role in cardiovascular disease. Not only do these metals serve as cofactors in metalloproteases known to participate in lesion disruption,[391] but their serum levels have been demonstrated to directly correlate with the disease status.[392] Stroke is the third leading cause of death and the leading cause of disability in developed countries. The disease is intimately linked with increased intracellular oxidative stress[393] as well as with changes in the quantitative distribution of metal ions.[393−395] Despite major advances in understanding of stroke risk factors and progression, few approved and effective therapies exist.

Recent findings imply that neuroglobin (Nb), a protein of the globin superfamily expressed in the brain, might potentially be involved in protecting neurons from ischemic insults.[396] To assess whether Nb might diminish the cellular response to experimental hypoxia−reoxygenation (H/R) injury, Duong et al. overexpressed Nb in cultured human neuronal cells and quantitatively analyzed alterations in the subcellular metal distributions by SXRF.[397] Control cells experiencing H/R injury showed increases in cytosolic Ca, Fe, Cu, and Zn accompanied by significant decreases in ATP, while Nb expressing cells were able to maintain cellular ion homeostasis at constant ATP levels.

The neurological events preceding and resulting from serious brain trauma can be assessed by a number of magnetic resonance imaging methods (MRI).[398] For example, the reduced apparent diffusion of water in the ischemic core results in an increased signal intensity in diffusion-weighted MR images. Another approach is based on the delayed increase of the longitudinal relaxation time (T_1) associated with the deposition of Mn ions during ischemia;[399] however, other processes such as lipid accumulation and tissue calcification may also result in a signal intensity delay of T_1-weighted images.[400] To resolve this issue and to further explore the origin and mechanisms of the delayed T_1 signal increase, the elemental distributions in the brain of rats subjected to 15 min transient focal ischemia were determined by SXRF, and the data were correlated with changes in relaxation time and the accumulation of MRS-visible lipids.[401] Two weeks after the ischemic insult, an increased T_1-weighted signal intensity was observed in regions of the ipsilateral dorsolateral striatum, accompanied by accumulation of Mn, Ca, and Fe. No evidence was found for accumulation of MRS-visible lipids or hydroxyapatite precipitation.

Given the previously observed correlation between the extent of Fe accumulation in lesions with atherogenesis progression, Langheinrich et al. employed a combination of synchrotron-based micro-CT (2 μm^3 voxels at 16 or 20 keV) and SXRF to obtain spatial distributions for Fe and Cu and thus to test whether the Fe deposits might serve as markers of intraplaque hemorrhage in the double-knockout apoE/LDLR$^{-/-}$ mouse model[385] of atherosclerosis (section 5.2.4.1).[402] By taking advantage of the specific photon-energy dependent attenuation coefficients, Fe and Ca deposits were directly distinguished on the basis of two CT scans acquired at different energies. The method was independently validated by micro-XRF experiments. The study indicated that Fe deposits within lesions originated from intraplaque hemorrhage. Furthermore, calcifications colocalized with Fe deposits and occurred in lesions with intraplaque hemorrhage without supporting chondrocyte-like cells. The authors concluded that Fe, which was detectable by simple 64-slice CT dual-energy imaging, could be used as an indicator of hemorrhaged lesions.[402]

5.2.5. Other Diseases Linked with Abnormal Metal Homeostasis

5.2.5.1. Hemochromatosis. Hereditary hemochromatosis (HC) is an autosomal recessive disorder of iron metabolism physiologically represented by cirrhosis of the liver, skin hyperpigmentation, cardiac problems, and diabetes.[403,404] The classic disease is characterized by mutations of HFE, a major-histocompatibility-complex-like protein involved in Fe absorption, leading to abnormal intestinal Fe uptake and accumulation of Fe-rich deposits in various organs.[404,405] It still remains unclear how HFE regulates Fe absorption and whether the abnormal Fe accumulation might affect the distributions and homeostasis of other transition metals.

While substantially increased serum levels of transferrin and ferritin, two major proteins involved in Fe transport, may be used as indicators to assess Fe overload, liver biopsy is still the gold standard for accurately quantifying Fe and determining the disease progression. In the search for an alternative, less invasive method, Guinote et al. used a combination of PIXE and STIM to investigate the Fe distribution in skin samples of patients diagnosed with HC.[406] The data showed that Fe was especially pronounced in lower epidermal regions where it showed a distribution analogous with P, S, Cl, K, Ca, and Zn localizations.

The interconnection between Fe, Cu, and possibly Zn metabolism[407] was the impetus for investigating the interplay among these metals in cirrhotic liver slices from hemochromatosis patients.[408] SXRF scans with a focal beam diameter of 15 μm showed a substantial increase in Cu content around cirrhotic regeneration nodules primarily associated with lymphocytic infiltration. Fe accumulation appeared to result in a decrease of Cu but increase of Zn, demonstrating the biochemical dependency and interplay of these transition elements in HC.

5.2.5.2. Osteoporosis and Associated Conditions. Osteoporosis is a systemic skeletal disease, which imparts an increased susceptibility to fractures due to decreased bone mass and microarchitecture deterioration.[409] Osteoporosis primarily manifests in response to various pre-existing conditions including hyperthyroidism, menopause, mechanical damage from surgery, or joint disease. A complete phenotypic and genotypic characterization of osteoporosis is lacking and thus poses a limitation for designing effective preventative treatment methods.[409] Given the role for metals in bone mineralization and structural maintenance of tissue[410] as well as tissue remodeling by serving as enzyme cofactors,[411] XRF methods have been used in a number of cases to elucidate the potential roles for metals in osteoporosis pathogenesis under various pre-existing conditions.

Often serving as an active site for tissue remodeling, the bone−cartilage interface is of particular interest because of its high metalloproteinase composition and consequent content of divalent metal ions.[412] SXRF was used to investigate the quantitative metal distributions across the bone−cartilage interface of equine metacarpophalangeal joint sections with and without osteoporosis.[281] Ca and Zn were of particular interest because of data from a previous study, which showed a prominent localization of Ca and Zn within the tidemark and calcifying cartilage regions of this interface

in normal tissue.[413] Results showed Ca and Zn localized outside of the immediate area of the osteoarthritic lesion at the cartilage surface while major elemental loss was observed within the lesion implying important roles for these metals in disease pathogenesis.[281] Similarly, a combination of PIXE and RBS methods was applied to study quantitative metal distributions in human femoral head slices with joint disease. Consistent with above results, the study revealed significant increases in Zn, Ca, and P within the cartilage zone, with Zn especially pronounced at the bone−cartilage interface.[414]

Menopause, a process characterized by ovarian failure and a sharp decrease in estrogen, is often followed by the onset of osteoporosis.[415] Ovariectomy (OVX) in female rats represents an animal model of osteoporosis because a sharp decrease in estrogen plasma levels promotes skeletal changes often observed in early postmenopause.[416] SXRF was used to analyze differences in quantitative metal distributions occurring within femoral bone slices of normal and OVX rats.[417] The study showed significant decreases in Ca levels, surprisingly accompanied by corresponding increases in Sr content for OVX cases. Moreover, despite its chemical similarity with Ca, Sr showed a rather heterogeneous distribution overall with a preferential localization to the cortical bone, while Ca was most pronounced in the trabeculae.[417]

To elucidate the routes of bone and metal loss in osteoporosis, SXRF combined with computed tomography (XRFCT) was used to investigate quantitative metal distributions from the periphery to the center of femoral head slices obtained from menopausal women with osteoporosis.[418] Results revealed a substantial decrease in the major elements of bone composition, Ca, P, and K within the spongy and cartilage zones in osteoporosis cases. Moreover, Ca correlated very well with P and relatively well with Zn, Sr, and K in normal bone tissue. The authors concluded that Zn and Sr are necessary trace elements in human tissue composition and serve an important function in bone metabolism. A combined therapy entailing Ca and Sr might be therefore superior oversimple Ca therapy for osteoporosis patients.

Given the link between hyperthyroidism and osteoporosis,[409] SXRF was employed to investigate changes in bone mineral composition in Wistar rat femoral bone slices with hyperthyroidism.[419] The data showed Sr homogeneously distributed, unlike Ca, which preferentially localized to certain regions. Zn was more pronounced in the hyperthyroid group and showed a homogeneous distribution except in the cartilage zone where S was also more pronounced.

5.2.5.3. Dental Caries. Dental caries, the localized demineralization and destruction of dental hard tissues, is initiated by sharp decreases in local pH as a result of acidic metabolites of dietary sugars produced by bacteria.[420] Because microscopic alterations of the dental enamel surface that are responsible for caries formation precedes the bacterial invasion, an understanding of the early stages of caries is particularly important. Although metal ions have been previously implicated in caries-related processes,[421,422] a detailed understanding of their particular roles at early stages of the disease is lacking. To elucidate changes in metal ion distributions associated with early caries, Preoteasa et al. applied broad-beam PIXE at 4 μm resolution to obtain quantitative topographical maps of metals within an incipient lesion induced at the enamel surface by *in vitro* demineralization.[423] The study revealed a Ca-rich layer where Fe and Zn were concentrated in distinct pools for normal enamel.

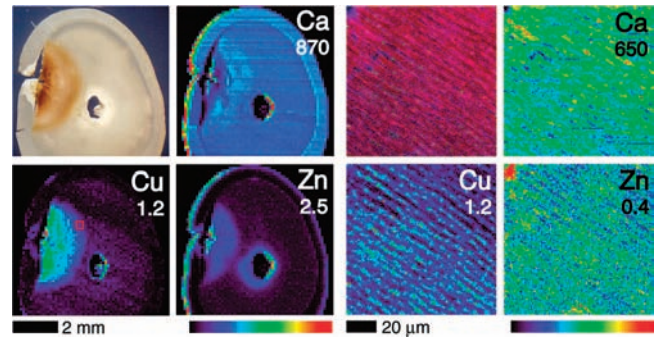

Figure 11. Optical micrograph (top left) and X-ray fluorescence (XRF) elemental distribution images of a 100-μm-thick section of an unrestored carious human tooth. Three-color overlay (top left; linear scale; Ca red, Cu green, Zn blue) and individual XRF elemental distribution images of a representative area (shown as a red square) of the carious front of the section. Maximum concentrations, in micrograms per gram, are shown below the elemental symbol for the XRF images. Reprinted with permission from ref 424. Copyright 2008 Springer Berlin.

Furthermore, enhancements for Fe, Cu, Zn, Pb, and Sr were observed at the surface compared with Ca after demineralization of the enamel, while Fe was almost completely lost and Zn was partially decreased in the inner enamel. The results indicated that the demineralization mechanism of incipient caries may depend on the inhomogeneous and anisotropic structure of enamel and that Fe and Zn are preferentially extracted from deeper locations by organic acids such as lactate.

Noninvasive methods for restoring demineralized dental tissue resulting from caries are highly desired, particularly in view of the quite invasive, rather painful, and expensive restoration procedures.[420] Given the importance of metal ions in dental caries progression,[425,426] the knowledge of specific alterations in metal ion composition might open new avenues for noninvasively intervening and treating dental caries. A recent SXRF imaging study unequivocally established alterations of the metal distributions in carious regions of human teeth (Figure 11),[424] showing increased amounts of Cu and Zn compared with unaffected areas. Specifically, Cu was transported and predominantly localized within dentinal tubules, whereas Zn displayed similar behavior but was more prevalent in the hydroxyapatite. While the mechanisms leading to increased Cu levels are not clear, the results from this study indicated that Cu may be potentially targeted to arrest the progression of dental caries.

In summary, XRF analysis of the metal ion topography in caries formation and progression has indicated major changes, especially for Fe, Cu, and Zn, pointing toward potential treatments for enamel restoration.

5.2.5.4. Epileptic Seizures. Although epilepsy is the most prevalent of serious brain traumas, the cellular mechanisms accompanying the pathologies and the clinical manifestations resulting from epileptic seizures remain to be fully characterized.[427] Several studies have suggested intimate links between alterations in metal homeostasis and the pathological mechanisms of epilepsy, although details regarding their individual roles have been conflicting.[173,428] In a recent study, SXRF was applied to determine the quantitative spatial distributions of metals in rat brain tissue following pilocarpine-induced seizures, the most commonly applied model of temporal lobe epilepsy.[429] Results showed regional specific changes for Ca, Cu, and Zn with Ca significantly more pronounced in distinct regions of the hippocampus and cerebral cortex of rats

experiencing seizures. Conversely, a major reduction in the levels of Cu and Zn occurred in independent regions of the dentate gyrus, a surprising result that contrasts earlier proposals that increasing concentrations of Zn and Ca are critical factors in excitotoxicity.[430] The authors attributed the Zn reduction to the fact that the analysis was performed after the seizure activity had already disappeared.

5.2.5.5. Infectious Diseases. The survival of pathogenic bacteria strongly depends on their ability to adapt to the challenging conditions of their host environment. To meet the necessary metal ion quota, infectious pathogens are particularly dependent on their host organisms.[431] The low Fe levels often observed in bacteria-containing vacuoles are presumably a result of the host's defense strategy.[431,432] In agreement with this picture, a detailed SXRF study showed that the Fe concentration decreased with time inside phagosomes of macrophages infected with *Mycobacterium smegmatis*; however, unexpectedly increased Fe concentrations were found for cells infected with the pathogens *M. tuberculosis* and *M. avium*.[433] The surprising increase of Fe was due to the pathogens ability to acquire Fe through the host's endocytic pathway as independently demonstrated by autoradiography of infected macrophages that were treated with ^{59}Fe-loaded transferrin.[433]

The malaria parasite, *Plasmodium falciparum*, causes the most severe form of malaria by inducing detrimental changes within the host's red blood cells (RBCs).[434] As the parasite matures, it develops disk-like structures at the RBC periphery, the Maurer's cleft system, which acts as a protein trafficking station reminiscent of the mammalian Golgi apparatus.[434] The identity of the proteins within the Maurer's cleft system, as well as the associated mechanistic pathways, is still unresolved. While primarily intended as a test system to evaluate Fresnel coherent diffractive imaging (CDI), a newly developed high-resolution X-ray imaging technique, Williams et al. studied the morphology of *P. falciparum*-infected RBCs and were able to identify small features such as Maurer's clefts with 40 nm resolution. Correlative SXRF images, although at significantly lower resolution, revealed regions of high Fe concentrations consistent with the subcellular localization of the hemozoin crystal. Furthermore, image reconstructions of Au-labeled surface and internal features of RBCs suggested the virulence factor, PfEMP1, trafficked to the RBC membrane via cytoplasmic organelles native to the host cell.[435]

5.3. Xenobiotic Trace Metals and Materials

5.3.1. Toxicology of Heavy Metals

5.3.1.1. Cobalt (Co). While Co is an essential trace element required for the formation of vitamin B_{12}, excessive administration leads to goiter and reduced thyroid activity. Occupational exposure to Co metal has been also reported to cause allergic dermatitis through direct skin contact.[436] Furthermore, exposure to radioactive ^{60}Co, a neutron activation product of ^{59}Co present in alloys, poses a principal risk for workers in the nuclear industry. At present, the molecular details representing the biochemical mechanisms of Co toxicity, transport, accumulation, and detoxification are still poorly understood.[436]

To directly assess Co-induced toxicity, the distribution and biochemical speciation of Co in human keratinocytes (HaCaT) exposed to Co(II) was studied by a combination of PIXE and RBS.[437] Keratinocytes are responsible for maintaining the architecture of the epidermis. Forming an environmental barrier required for survival, keratinocytes are consequently important in the pathogenesis of many diseases.[438] The ion beam data showed that exposure to excess Co(II) resulted in a dose-dependent accumulation of Co(II) predominantly within the cytosol. Areas with high Co and Fe levels were observed in the extracellular space, presumably caused from precipitation of sparingly soluble sphaerocobaltite ($CoHCO_3$).[437] Prompted by suggestions that Co-induced toxicity involves interference with DNA repair mechanisms,[439] Ortega et al. performed PIXE as well as SXRF analysis in tomography mode at the single cell level to elucidate the three-dimensional distribution of Co.[440] Human keratinocytes were incubated with 800 μM $CoCl_2$ for 48 h, and the Co distribution was analyzed by SXRF computed tomography (SR-XFCT) with excitation at 13 keV, requiring a total data acquisition time of 30 h. After reconstruction, the 3D imaging experiment confirmed effective internalization of Co as well as a more pronounced localization in the nuclear region. The PIXE data revealed that Co accumulated in the nucleus and in perinuclear regions of HaCaT cells thus indicating a possible direct interaction with genomic DNA and/or nuclear proteins. Moreover, exposure to excess Co resulted in a significant reduction of Mg and Zn levels in cells.[440] These results were consistent with previous implications of Co competing with Mg and Zn for their binding sites in DNA repair enzymes to induce its toxic effects.[439]

5.3.1.2. Hard Metal Lung Disease (HMLD). The toxic effects of Co have also been observed in workers exposed to hard metal, a material composed of tungsten carbide and cobalt typically used in the aircraft, automobile, and electrical industries.[436,441,442] Inhalation of dust particles containing hard metal can lead to a range of respiratory diseases, often referred to as hard metal lung disease (HMLD), which include occupational asthma parenchymal diseases such as interstitial fibrosis and giant cell interstitial pneumonitis. A large body of literature, recently summarized by Naqvi et al.,[443] illustrated the presence of homogeneously distributed particles composed of W, Ta, Co, Ti, and Fe in HMLD lung tissue samples. Interestingly, Co was only found in a small percentage of the cases, most likely due to metabolic solubilization. EPXMA was used to correlate the spatial distributions for, particularly, W and Co, as well as other metals with specific regions and structures in the mononuclear cells of tissue isolated from HMLD patients. Results showed W and Co with distributions most pronounced in centrilobular fibrosing lesions and peribronchioles closely associated with a number of selected macrophages.[444]

5.3.1.3. Chromium (Cr). Discovered by the French chemist Vauquelin in the ore crocoite (lead chromate) in 1798, chromium has found broad uses in metallurgy, leather tanning, and dye and textile production, as well as in the chemical industry.[445,446] Already in the late 1800s, it was recognized as a nasal carcinogen among chrome pigment workers. Extensive epidemiological studies showed that the exposure to hexavalent chromium directly correlated with the induction of lung cancer.[445] Instances of Cr-induced carcinogenesis have become more prevalent as a consequence of both occupational and environmental exposure to carcinogenic Cr(VI) compounds.[445,446] Conversely, trivalent chromium often begets positive physiological effects such as initiating insulin action, improving normal lipid metabolism, reducing the risk of cardiovascular disease, decreasing total serum cholesterol levels, and inducing weight loss and is

thus becoming increasingly incorporated into dietary supplements.[446] The apparently low toxicity of Cr(III) is presumably rooted in its preference of forming low-spin coordination compounds, which are kinetically inert toward substitution reactions. However, a number of studies have also reported adverse genotoxic effects of Cr(III) in cells, hence raising concerns regarding the safety of incorporating Cr(III) into dietary supplements.[446−449] Understanding the mechanisms involved in the intracellular biotransformation of chromium compounds is essential for both developing ways to offset Cr-induced toxicity and the safe administration of Cr(III) as a dietary supplement.

The mechanisms of Cr(VI)-induced toxicity might involve the production of organic or hydroxyl radicals by intracellular reductions of Cr(VI), or the direct reaction of metabolized Cr(IV) or Cr(V) intermediates with DNA or RNA to produce strand breaks or the formation of DNA−protein cross-links by kinetically inert Cr(III) species.[447] To gain a better understanding of the role of oxidation states in Cr-induced toxicity, SXRF was used to investigate the quantitative spatial distribution for Cr in thin-sectioned Chinese hamster lung cells exposed to either Cr(III), Cr(V), or Cr(VI) complexes.[450] The intracellular Cr distribution of cells treated with 100 μM Cr(VI) correlated with increased levels of Cl and P. Chromium was especially pronounced in hot spots colocalizing with P-rich areas, indicative of the nucleus, suggesting that the carcinogen is capable of targeting the DNA and potentially imposes genotoxic damage. Moreover, Cr was also observed in the perinuclear region, possibly representing acidic vacuoles. In contrast, cells treated with Cr(III) or Cr(V) complexes displayed only very low intracellular Cr concentrations.[450]

In a follow-up study, the distribution and speciation of the same complexes were analyzed in situ by micro-XANES.[451] Cells treated with Cr(VI) complexes revealed that the intracellular oxidation state was predominantly Cr(III); however, the reduction did not occur quickly enough to prevent Cr from entering the cell nucleus.

Given the enhanced carcinogenicity of insoluble versus soluble Cr(VI),[445] Ortega and co-workers used SXRF and XAS to elucidate the distribution and speciation of Cr in V79 Chinese hamster lung cells exposed to either soluble or insoluble Cr(VI) compounds.[452] In cells exposed to soluble Cr(VI) compounds, chromium showed a homogeneous distribution with significant localization to the cell nucleus. Upon excitation at 5993.5 eV, the pre-edge peak characteristic for Cr(VI) compounds, no Cr(VI) species were detected, suggesting rapid intracellular reduction. Cells treated with insoluble Cr(VI) compounds showed a homogeneous Cr distribution with pronounced nuclear localization. Contrary to the experiments with soluble Cr(VI) compounds, Cr(VI)-rich deposits were observed, suggesting increased carcinogenicity for insoluble Cr(VI) complexes.[452] A later study by the same research group confirmed the earlier results and additionally indicated that Cr(III) must originate from extracellular dissolution and reduction to chromate rather than from intracellularly engulfed Cr(VI) particles.[453]

Despite the stability of Cr(III) complexes toward ligand substitution, a change in oxidation state, for example by biological oxidants, could yield highly reactive species.[454] To ascertain whether redox cycling of chromium compounds is indeed feasible, Harris et al. investigated in situ the structure of Cr(III) complexes produced by intracellular reduction of Cr(VI). Specifically, SXRF and XANES were used to study the influence of incubation time on elemental distributions as well as the local chemical environment and oxidation state characteristic of metabolized Cr(VI) compounds within single human lung epithelial (A549) cells exposed to Cr(VI).[455] Treatment with 100 μM Cr(VI) for 20 min resulted in Cr primarily being confined to a small area of the cytoplasm in a region that colocalized with S, Cl, K, and Ca. Upon treatment for 4 h, Cr showed a homogeneous distribution throughout the cell, with enhanced concentrations in the nucleus and at the plasma membrane. Moreover, micro-XANES analysis of Cr hot spots suggested the presence of Cr(III) in a local environment of a polynuclear nature, which was ultimately confirmed by XAFS analysis.

5.3.1.4. Arsenic (As). Arsenic (As) is a metalloid responsible for arsenicosis, a chronic form of As-induced poisoning associated with contaminated drinking water consumed over long time periods.[456,457] Arsenicosis induces cancers of the skin (keratosis), kidney, bladder, lung and liver and black foot disease (gangrene).[456,457] At the same time, the antileukemia drug Trisenox (As_2O_3), which successfully cures 65−80% of patients with relapsed acute promyelocytic leukemia, paradoxically takes advantage of the As-induced toxicity (see also section 5.2.2.2).[307] Various other As derivatives are currently being explored for the potential treatment of leukemia and other malignancies,[458,459] thus underscoring the importance of elucidating the mechanisms governing As-induced toxicity. The mode of action responsible for As-induced toxicity is most likely dependent on the oxidation state of As metabolites, which predominantly occur as As(III) and As(V) species.[456,457] Recent studies by Hayaka et al. emphasized the importance of arsenic triglutathione [$As(GS)_3$] and glutathione-bound methylated intermediates in the biotransformation of arsenic (As_2O_3),[460] a finding that questioned the widely accepted metabolic pathway proposed by Challenger over 60 years ago.[461] Initial SXRF and micro-XANES experiments aimed at elucidating the in situ speciation of As in human ovarian adenocarcinoma cells exposed to Trisenox indicated that As predominantly existed in its trivalent oxidation state,[271] a result that agreed well with earlier studies based on atomic absorption spectrometry of bulk samples with separative techniques on hepatocyte carcinoma cells.[462] No significant differences in As levels were found between the cytosol, nucleus, and mitochondria. To further clarify ambiguities regarding the As speciation, Munro et al. applied SXRF and XAS to investigate the in situ speciation and subcellular distribution of As in HepG2 human hepatoma cells treated with 1 mM arsenite.[310] Arsenic accumulated in the euchromatin region of the nucleus, where it existed predominantly as an As trisulfur species; however, the XANES and EXAFS data provided no conclusive evidence for [$As(GS)_3$] as the predominant species and pointed toward protein-bound As species with more constrained symmetry.[310]

Central neuropathies, characterized by an impairment of neurological functions such as learning, short-term memory, and concentration, are directly linked with incidences of As exposure.[463] For example, rodents exposed to arsenic showed behavioral alterations and reduced locomotive activity.[464] Furthermore, there is evidence that Trisenox treatment might influence the balance of other trace elements in the body.[465] In particular, alterations in Fe metabolism might be responsible for the generation of intracellular ROS, which are the cause of oxidative stress.[466] To evaluate the potential roles of other trace metals in As toxicity, Rubio et al. utilized

SXRF to quantify the elemental distributions in brain tissue of Wistar rats that were chronically exposed to 100 ppm of sodium arsenite in drinking water over a period of 30 days.[467] Compared with control animals, the amount of As increased while the levels of Cl, K, and Fe decreased in brain tissue; however, the total As concentration ultimately reached a saturation point and diminished with further increased As dose. Furthermore, As showed a rather uniform distribution throughout the brain tissue, indicating a homogeneous blood irrigation of the brain. The elements Cl, K, Fe, Zn, and particularly Cu were redistributed and appeared increasingly uniform with increased As exposure.

Selenium, an essential trace element, is thought to interact with toxic elements such as As, Cd, Hg, Pb, or Bi to form insoluble complexes that precipitate into tissues, consequently preventing their toxic and carcinogenic effects.[468,469] Evidence directly supporting the aforementioned claim was provided by studies performed on rabbits showing a mobilization of Se to the liver and bile following exposure to arsenic.[470] The proposed antagonistic relationship between As and Se, where one modifies the toxic effects induced by the other,[471] prompted Berry and co-workers to directly analyze their interaction at the subcellular level in rat kidney cells using EPXMA combined TEM.[472] According to these studies, As and Se concentrated and precipitated in the lysosomes of renal cells in the form of insoluble selenide (As_2Se_3), which over time was secreted, thus providing direct evidence for the proposed detoxification mechanism at the metabolic level.

While other studies demonstrated that organoselenium compounds effectively counteract the As-induced increase in cancer risk,[473,474] the mechanism of organoselenium action was primarily thought to mimic the antioxidative action observed for vitamin E.[469] An alternative mechanism in combating high levels of As might involve the formation of the seleno-bis(*S*-glutathionyl)arsinium ion followed by biliary excretion.[475] These data prompted Burns et al. to study the distributions and speciation of As and Se in the skin and liver of hairless (HR-1) mice exposed to excess As and Se.[476] The K-edge XANES data were indeed consistent with the presence of the seleno-bis(*S*-glutathionyl)arsinium ion in the liver, thus supporting the notion that this complex is responsible for the prevention of As-induced toxicity. Furthermore, As exposed mice showed elevated As levels in the hair follicles and epidermis regions of the skin and a diffuse distribution in the liver. Conversely, supplementation with organoselenium compounds resulted in a marked suppression of As accumulation, with undetectable levels of As in skin and only low levels in the liver of mice exposed to As.

The cellular and subcellular distribution of selenium itself has not yet been investigated in detail. Most recently, SXRF imaging was used to specifically investigate the role of Se in spermatogenesis. High-resolution scans revealed a dramatic Se enrichment specifically in late spermatids.[477]

5.3.1.5. Cadmium (Cd). Primarily found in zinc-containing ores, Cd is widely distributed in the earth's crust at concentrations ranging from 0.1 to 1 ppm.[478] The metal is commonly used in batteries, in pigments, for electroplating and coating, as stabilizer in plastics and alloys, and in the green and blue phosphors of color TV tubes.[478] While significant exposure to Cd occurs primarily for people with jobs involving mining, smelting, processing, and battery manufacturing, nonoccupational forms of Cd exposure from various foods, tobacco smoke, and water also exist.[478] Short-term exposure to Cd leads to pulmonary irritation, while long-term exposure adversely effects the liver, kidney, and reproductive system, as well as other vital organs, often leading to cancer development.[478,479] The extent of Cd-induced organ toxicity depends on the dosage, route, and exposure duration.[479] The metal primarily accumulates in the liver and kidney, where it is mostly bound to metallothionein, a cysteine-rich metal-binding protein that has been implicated in zinc and copper homeostasis, redox metabolism, and heavy metal detoxification.[480,481] At present, the mechanisms of Cd-induced toxicity and its effect on the homeostasis of other transition metals remain mostly unexplored.

Motivated by an earlier report showing that oral administration of Cd resulted in alterations in several trace metals,[482] Nagamine et al. speculated that Cd interference with the homeostasis of essential metals might play a critical role in Cd toxicity.[483] Using a newly developed in-air micro-PIXE technique, they analyzed the elemental distribution in the liver and kidney of mice given chronic intraperitoneal injections of $CdCl_2$. In addition, expression levels of metallothionein (MT) were histologically assessed and correlated in the same tissue sections. Cd and Fe were significantly enhanced in the liver of Cd-exposed mice with Cd discretely localized in regions that were spatially correlated with Fe depositions. In the kidney of Cd-exposed mice, Cd localized in the tubular epithelia and in the tubular lumen, while Fe levels were significantly decreased. In the renal cortex, Cd deposits localized in regions distinctly different from areas of Fe hot spots. Furthermore, the spatial distribution of Cd correlated positively with focal accumulations of Ca and S observed in the liver and to a lesser extent in the kidney. Moreover, MT expression was significantly increased in both the liver and kidney of Cd-exposed mice. Taken together, the results indicated that nephrotoxicity was more prominent than hepatotoxicty, implying roles for Fe in resistance to hepatorenal toxicity induced by chronic Cd exposure.[483]

The severity of Cd exposure in the testis is evidenced by the occurrence of hemorrhagic necrosis of testicular tissue shortly following Cd exposure.[484,485] Given the previously observed alterations in Fe, Cu, and Zn levels in testicular tissue upon Cd administration,[486] Kusakabe et al. applied in-air micro-PIXE and atomic absorption spectroscopy to examine the distribution of Cd, Zn, Cu, and Fe in testicular tissue from rats exposed to $CdCl_2$.[487] The study revealed pronounced distributions for Cd and Fe in the interstitial tissues and seminiferous tubules of damaged tissue, probably the direct result of Fe flowing into the seminiferous tubules followed by disintegration of the blood−testis barrier (BTB). Cu accumulated on the testicular basement where Fe, Zn, and Cd showed major areas of colocalization within 12 h following exposure of rats to Cd. After 24 h, Fe and Cd were widely distributed in the seminiferous tubules where Cd was strongly colocalized with regions of Zn, and Cu accumulated in the seminiferous lumens.[487]

In the testis, the BTB consists primarily of tight junctions of Sertoli cells.[484] Given the aforementioned observations of major degradation of the BTB shortly after Cd exposure, Kusakabe et al. used AAS and in-air PIXE to further investigate the distribution of Cd, Fe, and Zn in Sertoli cells.[488] The data showed increased Cd and Fe and decreased Zn in the cytoplasm of Sertoli cells following exposure to Cd, suggesting that the major target of Cd toxicity was the cytoplasm while Fe presumably further enhanced the Cd-induced damage.

5.3.1.6. Mercury (Hg). In nature, mercury is present as metallic mercury or quicksilver, mono- and divalent inorganic compounds, and organomercury compounds. The metal is widely used in dental amalgams, pharmaceuticals, and cosmetics. As a result of human activity, Hg is widely distributed in the biosphere and can be found as a contaminant in food sources, most notably in fish.[489,490] While Hg exposure primarily results in adverse neurological effects during both prenatal and postnatal periods,[489,490] Hg-induced nephrotoxicity, clinically manifesting as acute tubular necrosis and immunologic glomerulonephritis, has also been reported.[489] While Hg-induced toxicity has been well characterized at the whole-animal level, tissue or cell-specific Hg accumulation and the potential alteration of trace metal homeostasis have not been thoroughly investigated.

In toxicological studies, the mode of cell death plays an important role. Depending on the concentration of a toxicant,[491,492] cell death may occur via necrosis, a relatively passive form of cell death caused by noxious stimuli, or by apoptosis, a physiological mode of cell death designed to immediately dispose of unwanted cells.[493] In view of the limited available information concerning metal-induced apoptosis or necrosis in cell culture models,[492] Homma-Takeda et al. investigated the mechanisms surrounding apoptotic and necrotic processes occurring in cells of kidney tissue isolated from Wistar rats following exposure to $HgCl_2$.[494] SXRF was used to determine the quantitative Hg distribution, while the extent of nephrotoxicity, necrosis, and apoptosis induction were monitored by alkaline phosphatase (ALP) activity in urine, morphological alterations, and the terminal deoxynucleotidyl transferase-mediated dUTP nick end-labeling (TUNEL) assay, respectively. The study revealed a dose-dependent fragmentation of renal DNA. Apoptotic cells resulting from Hg exposure contained a higher level of Hg and were primarily located in the proximal tubules, but not in the distal tubules, glomeruli, or medullary tubules. The site-specific accumulation of Hg in the proximal tubular cells appeared to be associated directly with the induction of renal apoptosis and necrosis.[494]

While adults are affected by the toxicity of methyl-Hg compounds, exposure *in utero* has particularly severe consequences, including microcephaly, cerebropalsy, seizures, and mental retardation.[469,495] Methyl mercury compounds are actively transported across cell membranes and might induce changes in cellular Ca(II); however, the specific reasons for their toxicity remain mostly unclear. To study the toxicity of MeHg in the context of embryonic development, Korbas et al. visualized by SXRF the localization of Hg and other trace elements in zebrafish larvae.[496] Following treatment of larvae with either ethyl or methyl mercury compounds, Hg concentrated primarily in the rapidly dividing lens epithelium at levels four times higher than those in other tissues (Figure 12). Overlay images of Hg, Zn, and S showed that the Hg-rich cell layer enclosed the lens interior, which had a high S content, while Zn was elevated in the retina. Consistently lower Hg concentrations were found in the brain, optic nerve, spinal cord, liver, and muscle. The data implied that Hg toxicity associated visual impairment may directly arise from contact with the ocular tissue rather than being caused by neurological effects.

There is clear evidence that amalgam fillings lead to increased levels of Hg in the kidney, blood, and urine in addition to other body regions, but questions concerning the toxicity induced by these Hg levels remain intensely debated.[497] Given that the majority of reports considered only the ingestion or inhalation of Hg from the surface of fillings as relevant modes of exposure, Harris et al. investigated whether the direct migration of Hg through the tooth into the bloodstream might constitute an alternative pathway.[498] SXRF and XANES were used to determine the quantitative spatial distributions for Hg, Ca, Zn, and Cu and to gain information on the chemical environment of Hg in sections of human teeth that were filled with amalgam for 20 years or longer. Hg and Zn were detected in locations several millimeters away from amalgam locations with Hg present at higher concentrations in the dentinal tubules and Zn homogeneously distributed. XANES data suggested a change occurred in the local chemical environment of Hg in the tooth compared with the environment observed in the amalgam

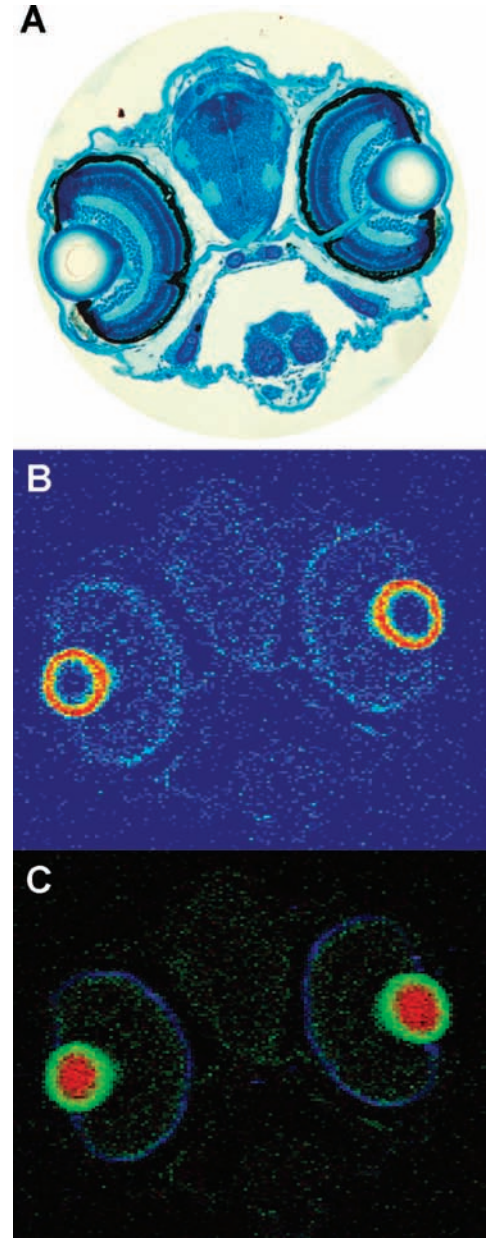

Figure 12. High-resolution elemental distributions of zebrafish head. Head section from zebrafish larvae treated with 100 μM MeHg−L-cysteine for 24 h: (A) histological image; (B) mercury distribution using X-ray fluorescence imaging at 2.5 μm resolution; (C) Hg (green) superimposed on S (red) and Zn (blue). Quantities of the different elements are plotted on arbitrary scales. Reprinted with permission from ref 496. Copyright 2008 National Academy of Sciences.

originally. The differing spatial distributions of Hg and Zn imply distinct transport mechanisms for the two metals. Importantly, the detection of Hg in areas of the tooth that once contained an active bloodstream and in the calculus indicated that both exposure pathways were indeed significant and should be considered in future toxicity studies.[498]

Acute infectious diseases are directly associated with alterations in the dynamics of essential trace elements such as Fe, Cu, Zn, and Se,[499] all of which are considered to be critical to the host's defense mechanisms.[500,501] Nonessential trace elements such as Hg may compete with essential trace elements in the target organs of infection via metabolic interactions, thus preventing them from fulfilling their protective roles.[469,495,502] As part of the general host response to coxsackievirus B3 (CB3) infection, the essential Se and nonessential Hg interact and affect inflammatory tissue lesions induced by CB3 infections.[503] ICP-MS and PIXE methods were applied to measure the spatial distributions for Hg and Se in the early phase of CB3 infection in brain tissue from normally fed female Balb/c mice, an animal model of CB3 infection.[504] ICP-MS results suggested elevated levels of Hg and Se were present in brain tissue of infected mice, although PIXE analysis failed to identify localized regions of these elements at concentrations high enough for detection. The authors subsequently proposed a homogeneous distribution for Hg and Se to explain the low PIXE signal and further proposed that the increase of Hg in the brain during infection may possibly influence the early pathogenesis of the disease.[504]

5.3.1.7. Lead (Pb). Lead (Pb) is a toxic heavy metal associated with a number of chronic diseases of the nervous, hematopoietic, skeletal, renal, and endocrine systems upon prolonged exposure.[505,506] Although substantial efforts have been made to reduce Pb exposure by eliminating leaded gasoline and leaded pipes in addition to reducing workplace exposure, Pb remains persistently present in the environment.[505] While the half-life time of Pb in the blood is only one month, it is around 20 years in the skeleton, where almost 95% of total body Pb accumulates.[505] Given the shortage of treatment options for Pb-induced toxicity, research geared toward understanding the mechanisms of Pb toxicity is of great importance.

The osteochondral unit has a highly complex structure designed to enable friction-free movements in articulating joints, to resist static and dynamic loads, and to transfer loads from articular cartilage to the underlying bone.[505] Motivated by previously identified correlations between Pb exposure and bone diseases, Zoeger et al. investigated the mechanisms of Pb-induced toxicity in the osteochondral unit.[507] Specifically, the spatial distribution of Pb, Zn, Sr, and Ca were assessed in the chondral and subchondral regions of bone tissue from normal humans. SXRF images at various geometries were correlated with backscattered electron (BE) images, providing the elemental and structural features of the tissue. Pb distinctly accumulated in the tidemark, the transition zone between calcified and noncalcified cartilaginous matrix, where it maintained fluorescence intensities 13-fold higher than those observed for Pb in the subchondral bone. Moreover, the distribution of Pb in the subchondral bone region strongly correlated with the observed distribution of Zn but was distinctly different from the localizations of Ca and Sr.

In a similar study, Zoeger and co-workers again used SXRF at various geometries and subsequent correlation with BE images to analyze the distribution of Pb together with Ca, Zn, and Sr at the cartilage−bone interface in femoral heads and patellae from normal humans at an enhanced spatial resolution.[508] The data likewise showed a highly specific accumulation of Pb at the tidemark, where it correlated very well with areas of Zn accumulation. Based on the established role for the tidemark region in osteoarthritis pathogenesis, Pb was further implied to be strongly associated with joint disease.[508]

Evidence suggests that Pb exposure results in adverse effects on mineralization processes of tooth enamel and developing teeth, processes often leading to dental caries formation.[509,510] Conversely, Zn has been suggested to play roles in the development and maintenance of dental tissue and hence must be maintained at certain levels by the body to avoid dental caries formation (see also section 5.2.5.3).[511,512] Moreover, Zn administration was shown to reduce the tissue and organ levels of Pb in animals.[513,514] Given the implied interplay between Pb and Zn in dental processes, SXRF was used to measure alterations in the distributions of the two metals during Wistar rat ameloblast differentiation from the presecretory to the early maturation stage.[515] Results showed higher levels of Zn in the nucleus than in the cytoplasm, while the Zn concentration in both the nucleus and cytoplasm were significantly higher during the maturation stage compared with the presecretory stage. Moreover, Pb concentrations could only be determined reliably in developing enamel given that a Pb signal above background was basically absent in ameloblasts.

Motivated by observations of Pb exposure leading to various adverse cognitive effects,[516] Zoeger et al. determined the spatial distribution of Pb along with other trace elements in human brain tissue sections using SXRF.[517] The data revealed that S, Ca, Fe, Cu, Zn, and Br localized in distinct regions, which clearly represented brain vessel structures, while Pb showed a heterogeneous distribution with isolated deposits located partially within the vessel wall and the brain tissue.

5.3.1.8. Lanthanum (La). Controlling phosphatemia, the abnormal accumulation of inorganic phosphates in the blood, is essential for the management of bone disease as well as the prevention of vascular calcifications with end-stage renal failure.[518] Current phosphate-binding agents, although effective, are often associated with severe adverse effects, thus advocating the development of alternative binders.[518] Lanthanum carbonate has emerged as an alternative, well-tolerated noncalcemic phosphate binder, which was more effective at reducing urinary excretion of phosphate.[518,519] The phosphate binding action of lanthanum carbonate involves ionic interaction and precipitation of phosphate complexes within the intestinal lumen, consequently preventing dietary phosphate absorption. The excretion of La occurs via the liver.[519] A number of studies were devoted to a more thorough characterization of the associated pharmacokinetics to evaluate the safety of lanthanum carbonate administration.

Patients with chronic renal failure (CRF) require adequate control of their phosphate metabolism. High doses of lanthanum carbonate may lead to impaired bone mineralization as a secondary process following phosphate depletion.[520] To study the effects of lanthanum carbonate treatment, Behets et al. used scanning SXRF to map the quantitative spatial distributions of Ca and La in bone samples from CRF rats.[521] Oral administration of lanthanum carbonate over 12 weeks to CRF rats resulted in bulk bone La concentrations up to 5

μg/g wet weight with La distributed at the edge of mineralized bone, at both actively mineralizing and quiescent sites, independent of the type of bone turnover. In the presence of hyperparathyroid bone disease, La likewise localized throughout the mineralized trabecular bone showing no apparent correlation with the osteoid or underlying bone pathology. Furthermore, the La distribution remained basically unaltered following a 2- or 4-week washout period. Taken together, the results implied no obvious relationship between the localization of La in bone and the presence of the mineralization defects,[521] thus further substantiating previous results.[520]

Oral treatment with lanthanum carbonate results in a sharp increase of La in the liver of CRF rats.[522] This observation prompted Bervoets et al. to conduct more detailed studies on the hepatic and gastrointestinal (GI) absorption of La in CRF rats using a combination of TEM, EELS, and SXRF.[523] The results revealed that liver La localized in the lysosomes and in the biliary canal, suggesting that La was transported and eliminated by the liver via a transcellular, endosomal−lysosomal−biliary canicular transport route. Oral administration of lanthanum carbonate to CRF rats resulted in a doubling of La liver levels, which plateaued at six weeks, compared with normal rats, while La levels in serum were basically identical for both groups. Upon intravenous administration of lanthanum carbonate, for bypassing the GI tract portal vein paths, La levels in the liver were effectively the same for each group, thus suggesting increased GI permeability or absorption of oral La exists in uremia. Furthermore, La levels in the brain and heart fluctuated around the La detection limit with long-term (20 weeks) treatment having no effect on organ weight, liver enzyme activities, or liver histology.[523]

5.3.1.9. Gadolinium (Gd). Because of their favorable paramagnetic properties, Gd(III) complexes are widely used as intravenous magnetic resonance imaging (MRI) contrast agents (see also section 4).[524] Extracellular Gd(III)-based contrast agents are typically composed of a macrocyclic ligand, such as DTPA (diethylenetriamine pentaacetic acid), that strongly chelates the otherwise highly toxic Gd(III) ion.[525] The increased use of Gd-based contrast agents in biomedical imaging also increased the demand for thorough toxicological studies detailing the biodistribution of these agents. With a biological half-life of approximately 30 min, the contrast agents are rapidly excreted by the liver and kidney; however, there is some concern that dissociated Gd(III) ions might deposit in tissues. For example, recent studies indicated that Gd-based contrast agents potentially constitute an important factor in the pathogenesis of nephrogenic systemic fibrosis (NSF).[526] To assess the cellular uptake and distribution of newly developed Gd(III)-based contrast agents, numerous studies have relied on the sensitivity and spatial resolution offered by in situ SXRF imaging.[527−529] While the inherent cell impermeability of most Gd(III) contrast agents is presumably an important factor for their fast distribution and clearance from the body, it poses at the same time limitations to dynamically visualize intracellular processes. To address these short-comings, Meade and coworkers developed a series of Gd(III) contrast agents[527,530] conjugated to polyarginine or stilbene cellular transduction domains acting as intracellular delivery vehicles.[531] SXRF images showed a substantial increase in Gd(III) fluorescence, which increased with increasing concentration, for all derivatives compared with cells incubated with Gd(III)−DOTA or Gd(III)−DTPA agents lacking the transduction domain.[527] Compared with the uniform distribution of the polyarginine conjugated complex, the stilbene derivative revealed a more punctate pattern, presumably due to its amphipathic nature and tendency to aggregate in aqueous media.[532] Surprisingly, a large variation was observed for Gd(III) concentrations within a given cell population suggesting the uptake of contrast agents was not necessarily homogeneous. The study demonstrated that polyarginine- and stilbene-functionalized Gd(III) contrast agents label three different cell lines sufficiently for observation via MRI. In a similar effort, Endres et al. investigated cell-permeable contrast agents that incorporated a cleavable disulfide linkage between the agent and the transduction moiety.[529] SXRF imaging revealed an increased cellular retention for two of the four compounds investigated, suggesting that this strategy might be suitable to further prolong image contrast and improve the overall efficacy of these contrast agents.

Ahlem et al. used EPXMA and SIMS (section 6.1) to assess the intracellular localizations of Gd and Tb in the liver and the intestinal mucosa of hepatic tissue from Wistar rats.[533] Gd and Tb concentrated in P-rich areas within the lysosomes of hepatocytes in areas close to the biliary canalicule following intraperitoneal administration, while intragastric administration resulted in Gd and Tb localizing in the lysosomes of the apical part of duodenal enterocytes. The observed concentration−precipitation mechanism in lysosomes of enterocytes was suggested to limit the diffusion of foreign particles through the digestive barrier, consequently allowing their elimination with apoptotic cells of the intestinal lumen.

Upon binding to large macromolecules, Gd(III) contrast agents experience an increase in relaxivity as a result of a decrease in rotational correlation time, which in turn improves the overall image contrast.[225] Steroids interact with specific nuclear receptors in the cell, are hydrophilic, and are relatively small in size, hence representing an attractive selection for achieving enhanced cellular uptake and retention and increased MR signal contrast.[534,535] SXRF results revealed that the incorporation of an aliphatic carbon linker between the steroid and the Gd(III) chelate dramatically enhanced cell permeability.[528] Furthermore, progesterone-modified Gd(III) contrast agents were shown to activate transcription of progesterone receptors. No apparent toxicity was observed to occur from these contrast agents, and MRI showed a prolonged relaxation time of nearby water protons, which resulted in a significant enhancement of the MR contrast signal.[528]

5.3.1.10. Uranium (U). Natural uranium (U) is a mixture of three radioactive isotopes, ^{238}U, ^{235}U, and ^{234}U, where ^{238}U is the most abundant nuclide contributing more than 99.2%. The isotope ^{235}U is of particular interest due to its ability to sustain nuclear chain reactions; however, it comprises only 0.72% of naturally occurring uranium and must be enriched to a level of 2−4% for use as nuclear fuel. Being significantly less radioactive, the remaining depleted uranium is increasingly used for civilian and military purposes, thus potentially creating new environmental and health problems.[536]

Upon internalization by the body, U rapidly transits via the bloodstream to target organs, mostly bones and kidneys, where it induces visible cell damage. Approximately 80% of the initial dose is excreted during the first 24 h postcontamination. Short-term exposure to U at high concentrations results predominantly in nephrotoxicity, while chronic

exposure leads to accumulation of U in the skeleton.[536] To investigate the mechanism of uranium nephrotoxicity, Carriere et al. studied the accumulation and redistribution of U after acute intoxication of rat renal proximal tubule epithelial cells.[537] Upon exposure to uranyl bicarbonate, the extracellular and intracellular precipitates were studied on thin sections of cells by TEM. PIXE and RBS data showed a positive correlation between U incorporation and cell toxicity. Furthermore, U was present as both a precipitate and a soluble form inside cells, potentially as a result of internalization of soluble U followed by partial precipitation or via two parallel internalization pathways.[537] On the basis of EXAFS data, the insoluble precipitates were identified as uranyl phosphate, whereas soluble U appeared to be mostly present as a carbonate complex.[538] Donnadieu-Claraz et al. investigated the distribution and speciation of U in the kidneys of rats chronically exposed to low levels of U present in drinking water.[539] With prolonged exposure time, EPXMA and EELS results revealed an increasing number of vesicles containing dense granular inclusions composed of iron oxides. While traces of U were detected, it was never associated with the Fe granules, suggesting that Fe homeostasis in the kidney might be affected by chronic U exposure. Evidence of acute and chronic U exposure inhibiting bone formation and impairing bone modeling and remodeling stimulated Milgram et al. to directly assess the chemical toxicity of uranium in rat osteoblastic bone cells.[540] While PIXE and RBS data revealed an increased resistance and greater accumulation of U compared with that in renal cells, U appeared localized as intracellular precipitates similar to those previously observed by SEM/EDS analysis.[537]

5.3.2. Nanoparticle Applications

Nanotechnology, a rapidly growing area of research, involves the investigation of structures and devices with lengths ranging from 1 to 100 nm.[541] The favorable optical, magnetic, and biological properties of nanoparticles (NPs) have paved new avenues for research in the fields of biology, chemistry, and biomedicine.[542] In particular, titanium dioxide (TiO_2) nanoparticles, semiconductor quantum dots (QDs), and Au nanoparticles offer distinctive optical and surface properties, which have been exploited in a broad spectrum of imaging, microscopy, biosensing, and therapeutic applications. Given that these NPs are composed of metal ions, a number of studies took advantage of the exquisite capabilities of in situ SXRF imaging methods aimed either at directly elucidating their biodistribution or at studying alterations in the homeostasis of other transition metals.

5.3.2.1. TiO_2 Nanoparticles. Titanium dioxide (TiO_2) nanoparticles have attractive photocatalytic and structural properties that offer widespread versatility in applications as disinfectants, as biological probes, as antitumor agents in diagnostic assays, and in gene targeting.[542] To generate materials with biological activity, the surface of the nanoparticles can be functionalized with proteins, nucleic acids, or other biomolecules. The resulting chemical−biological nanocomposites hold great promise as imaging labels, drug delivery vehicles, or gene therapy agents.

In search for new gene targeting agents with potential light-inducible nucleic acid endonuclease activity, Paunesku et al. combined 45 Å TiO_2 nanoparticles with short DNA oligonucleotide strands and investigated their biological activity in rat pheochromocytoma (PC12) cells.[543] SXRF images showed the TiO_2−oligonucleotide nanocomposites localized to the cell nucleus in regions with high concentrations of Zn and P, presumably the nucleoli. Additional biochemical experiments demonstrated that these nanocomposites retained both the bioactivity of the DNA and their light-inducible endonuclease-like properties. Encouraged by these results, Paunesku et al. created also TiO_2 nanoconjugates with oligonucleotides matching mitochondrial or nucleolar DNA and assessed their target specificity in human breast and prostate cancer cells and PC12 rat cells.[544] SXRF data revealed that each nanoconjugate was retained within its target compartment, either the mitochondria or the nucleoli. In a similar effort, Endres et al. assessed the applicability of DNA-labeled TiO_2 nanoconjugates functionalized with a Gd(III)-based MRI contrast agent for targeting mitochondrial-specific DNA sequences in cancer cells.[545] Following validation of the MR activity of the functionalized nanoconjugates, SXRF imaging revealed their target-specific localization to mitochondria in both PC12 and PC-3M rat cells. Such multifunctional nanocomposites are particular promising agents for targeting specific DNA sequences while simultaneously allowing visualization of their biodistribution in whole organisms. Given the lack of intrinsic fluorescence of TiO_2 nanoparticles, direct visualization of their intracellular distribution is not possible by conventional fluorescence microscopy. To overcome this shortcoming, Thurn et al. explored two fluorescence labeling approaches, either through direct covalent modification of the nanoparticle surface with Alizarin Red S (ARS), a red fluorescent organic dye, or by attaching tetramethyl rhodamine (TMR) to the oligonucleotide strand.[546] Prostate and breast cancer cells treated with ARS-modified nanoparticles revealed a punctate intracellular staining pattern, while cells treated with ARS alone showed no detectable signal, demonstrating that ARS conjugation to TiO_2 was required to obtain a significant intracellular fluorescence. Moreover, pretreatment of PC-3M cells with unlabeled TiO_2 nanoparticles, followed by fixation, and subsequent incubation with ARS also resulted in a strong fluorescence signal, rendering this approach particularly attractive for flow cytometry applications. Furthermore, in cells treated with the TiO_2−TMR-labeled DNA nanoconjugates, the ARS-labeled DNA component colocalized well with the SXRF Ti signal in both nuclear and cytoplasmic areas, strongly implying that the intracellular integrity of the nanoconjugates was preserved in malignant cells.[546]

Soft X-ray tomography is an absorption-based imaging technique that is capable of producing 3D images with a resolution of better than 50 nm.[547] In order to identify cellular structures of interest, target-specific labels are required that can be differentiated from their environment, for example, based on a specific X-ray edge absorption energy. Given that the L-edge absorption of TiO_2 lies between 450 and 470 eV, a range that falls directly within the "water window" region where cellular structures generate high-contrast images,[548] Ashcroft et al. investigated the applicability of tubulin-targeted TiO_2−streptavidin conjugates as labels in soft X-ray tomography.[549] Absorption images showed strongly absorbing granules representing the TiO_2 conjugates, which labeled the filamentous tubulin structures, as identified by the Ti and C maps, respectively. The observed granular pattern for the TiO_2 conjugate was previously observed for structures labeled with immunogold[550] and possibly resulted from steric hindrance between the bulky conjugates and the target molecules or from unconjugated streptavidin competing with the TiO_2−streptavidin complex for binding to the biotin-

tagged microtubules. Nonetheless, the data showed that TiO_2 nanoparticles are suitable as soft X-ray imaging labels, which might be further combined with other probes, such as gold clusters, for simultaneous multilabel imaging experiments.

5.3.2.2. Gold Nanoparticles. Colloidal gold particles have been extensively utilized as antibody labels in electron microscopy.[551] Because of their large size, the particles cannot diffuse across the lipid bilayer of the plasma membrane, not even after treatment with detergents generally used in immunofluorescence staining protocols. For this reason, colloidal gold particles are only suitable for postembedding immunolabeling of resin sections, ultrathin cryosections, or freeze-fractured preparations. To overcome these problems, ultrasmall gold clusters of approximately 1.4 nm size have been developed,[552,553] which can be covalently conjugated to antibodies and used in standard immunolabeling protocols. Following the same procedure used in autometallography (section 2.3), the clusters can also be converted to larger sized particles by means of in situ silver or gold enhancement.[554] In search for a suitable xenobiotic label for correlative optical fluorescence and SXRF imaging, McRae et al. explored the utility of FluoroNanogold (FNG)-conjugated antibodies.[265] The commercially available FNG-labeled antibodies combine a regular organic fluorophore with a 1.4 nm Au cluster. Standard immunofluorescence labeling of the Golgi apparatus or mitochondria produced SXRF elemental maps of Au that clearly marked the subcellular localization of the organelles without the need for Ag or Au enhancement. Optical fluorescence images and the respective SXRF Au maps showed good correlations, thus confirming the integrity of the FNG label after the sample preparation. Besides their utility as biolabels, gold nanoparticles have moved increasingly into the center of attention due to their unique properties, including large optical field enhancements and efficient photothermal conversion.[555] Given the outstanding sensitivity, SXRF imaging might prove to be particularly useful for investigating the biodistribution of gold-based reagents in nanomedicine applications.

5.3.2.3. Quantum Dots. Quantum dots (QDs) are luminescent semiconductor nanocrystals with a diameter ranging between 1 and 12 nm.[556] The small size gives rise to quantum confinement effects, which result in fundamentally different properties compared with bulk solids.[557,558] The physical confinement of excitons is responsible for remarkable optoelectronic properties, including high emission quantum yield and tunable, narrow emission profiles. Compared with traditional organic fluorophores, QDs were observed to be 100 times more stable against photodecomposition.[559] While their low solubility in aqueous media was initially prohibitive to biological applications, these limitations were overcome by modifying the surface of CdSe/CdS core−shell QDs with biocompatible, water-solubilizing functional groups or materials.[559,560] Recently, Corezzi et al. tested the utility of commercially available CdSe/ZnS core−shell QDs conjugated to antibodies as correlative labels for optical fluorescence and SXRF analysis.[561] Standard immunofluorescence protocols were employed for labeling the cancer marker, HER2 (human epidermal growth factor 2) on the surface of SKOV3 cancer cells as well as β-tubulin, a cytoskeletal protein. The subcellular locations of the proteins were revealed on the basis of the selenium elemental map with 100 nm spatial resolution. Because the Se emission line does not overlap with the emission of other biologically relevant elements, no additional spectral deconvolution was required.

5.3.2.4. Toxicity of Nanoparticles. With the increasing large-scale production and application of nanoparticles, studies designed to uncover their fate and impact on the human body and environment have become increasingly important.[562−564] At present, still little is known about the mechanisms of biological uptake, their toxicity, their chemical behavior, and their distribution in the environment. Given that a large fraction of nanoparticles contain metal ions, XRF is especially well-suited for exploring the biodistribution and speciation of these materials and studying their fate upon release into the biosphere.

The incorporation of TiO_2 and ZnO nanoparticles (often as small as 20 nm) in sunscreens as UV filters has raised concern regarding their potential penetration into the stratum corneum and accumulation in vital tissues, where they could impose a long-term burden on the immune system.[565,566] Prompted by evidence of dermal penetration by exogenous nanoparticles,[567] Lekki et al. used a combination of ion microscopy (PIXE, RBS, STIM) and autoradiography to quantify the transport of ^{48}V-labeled TiO_2 nanoparticles through the stratum corneum of both human and porcine skin.[568] The data revealed that particles penetrated as deep as 400 μm into hair follicles, suggesting a mechanical translocation rather than passive diffusion. No particles were observed in vital tissues nor in the sebaceous gland.

Ultrafine Fe_2O_3 nanoparticles have biological applications in MRI contrast enhancement, tissue repair, immunoassay, detoxification of biological fluids, drug delivery, and cell separation.[569] Evidence linking the inhalation of ultrafine particles with adverse respiratory effects and cardiovascular diseases has spawned major questions concerning their safety for industrial and medical applications.[564] The olfactory tract is considered a potential access point for inhaled foreign particles entering the brain by passing across the blood−brain barrier. Observations of significant increases in Fe in the mouse olfactory bulb (OB) and deep brain regions upon intranasal instillation of Fe_2O_3 nanoparticles prompted Wang et al. to perform a more detailed analysis of the distribution and chemical state of Fe in mice exposed to Fe_2O_3 nanoparticles.[570] The SXRF and XANES data revealed that the average Fe content in the exposed mice increased by 31% and was especially pronounced in the olfactory nerve layer, glomerular layer, and the external part of the anterior olfactory nucleus compared with control mice. In brain stem regions, Fe increased by 21% and was particularly elevated in reticular and trigeminal regions. Furthermore, XANES data suggested the Fe^{3+}/Fe^{2+} ratio increased in both the OB and brain stem upon exposure to nanoparticles. Taken together with histological observations of fatty neuron degeneration in a region within the hippocampus, these results implied exposure to Fe_2O_3 nanoparticles resulted in adverse side effects.[570]

The bioaccumulation and toxicological effects of nanoparticles were also investigated with *Caenorhabditis elegans* as a simple model organism.[571] According to SXRF scanning data, exposure of *C. elegans* to engineered Cu nanoparticles resulted in Cu levels concentrating particularly in the head and a region 1/3 of the way up the body from the tail. The nanoparticle exposure also led to increased K levels and a striking alteration in the distributions of Fe and Zn with increased accumulation in the proximal gonad.[571]

Carbon nanotubes (CNTs) are a new class of materials with unique electrical, mechanical, and thermal properties. More recently, CNTs have attracted attention as potential carriers for drug, gene, protein, or vaccine delivery, thus raising important questions regarding their biocompatibility and possible adverse health implications.[572,573] Exposure to single-wall CNTs has been shown to induce oxidative stress and apoptosis in human keratinocytes[574] and to impair zebrafish embryo development.[575] A SXRF study of murine macrophages exposed to CNTs revealed Fe-rich zones inside or close to the membrane compared with untreated control cells.[576] Additionally, Fe-rich regions colocalized with regions of elevated P, thus suggesting a possible interaction of CNTs with the nuclear or perinuclear regions. Surprisingly, an excess of Ca was observed in cells exposed to CNTs compared with control cells.

The increasing use of quantum dots (QDs) in the semiconductor industry and potentially also in nanomedicine will inevitably lead to their discharge into the environment.[577,578] A very recent SXRF study was devoted to investigating the potential toxicity of CdSe quantum dots capped with ZnS in aquatic organisms.[579] According to Se elemental maps, the QDs exclusively localized to the gut of the aquatic organism. Furthermore, Zn and Se were highly correlated, suggesting that the QDs had not been metabolized to an appreciable extent. The data implied that the core−shell CdSe/ZnS QDs pose no significant toxic threat to the aquatic organism.

5.4. Environmental Metal Speciation

Every living organism inevitably exchanges elements with its surrounding environment, which provides essential nutrients for growth and absorbs metabolic waste products. The overall trace element composition of an organism provides therefore direct information on the inorganic ecology of the organism itself and the surrounding chemical composition of the ecosystem. This information is particularly valuable when assessing the environmental impact of xenobiotics and toxic pollutants.

5.4.1. Bacteria

5.4.1.1. Metal-Reducing Bacteria. Investigations of metal ion accumulation in *Escherichia coli* using bulk methods revealed that these bacteria accumulate metals such as Fe, Cu, Zn, and Mn to levels several times higher than the concentrations present in regular growth media.[3] The values reported for the total amount of these metals present in bacteria lie between the low and high micromolar ranges. Kemner et al. applied SXRF and XANES methods to acquire quantitative elemental maps and chemical environment information, respectively, for *Pseudomonas fluorescens*, an aquatic Gram-negative bacterium.[580] The data surprisingly showed that an intracellular accumulation of Cr accompanied by cell death occurred upon exposure of planktonic microbes to 1000 ppm of potassium dichromate, whereas no change in the elemental composition happened for cells in surface-adhered biofilms under identical conditions. Additionally, XANES data suggested that Cr(VI) was reduced upon cellular uptake and that phosphate probably served as the counterion.

The intensely studied species of *Geobacter* and *Shewanella* dissimilatory metal-reducing bacteria (DMRB) have the ability to reduce various polyvalent metal ions such as Cr(VI), Fe(III), Co(III), U(VI), and Tc(VII) present either as soluble complexes or associated with solid-phase minerals.[581] An unusual behavior of these organisms involves their production of high-molecular-weight c-type cytochromes associated with the outer membrane, presumably granting them access to insoluble metal electron acceptors.[582] Evidence suggesting a rapid reduction of U(VI), a radionuclide contaminant, by DMRB portrays bioreduction as an attractive option for removing soluble U(VI) from contaminated groundwater.[583] An earlier report demonstrated that reduction and extracellular accumulation of UO_2 precipitates occurred at the outer membrane (OM) surface and within the periplasmic space of *Shewanella putrefaciens* strain CN32, suggesting that the outer membrane cytochromes (OMCs) played a role in UO_2 formation.[581,582] To acquire a better understanding of the role for outer membrane cytochromes (OMCs) in U(VI) reduction, Marshall et al. applied a combination of genetic, immunological, and microscopic analyses to investigate both wild-type and various mutant strains.[584] Results revealed a close association of the extracellular UO_2 nanoparticles with an outer membrane decaheme c-type cytochrome, MtrC (metal reduction) and OmcA in *Shewanella oneidensis* MR-1 cells. Deletions of *mtrC* or both *mtrC* and *omcA* genes significantly slowed the rate of reduction of U(VI), while SXRF imaging showed an altered distribution and density of U(IV) nanoparticles localized on the extracellular features. Furthermore, a mutant deficient in cytochrome c maturation was unable to reduce U(VI) thus revealing a requirement of c-type cytochromes for the reduction of soluble U(VI) carbonate complexes. Results from SXRF microscopy and EM immune-localization analyses revealed the presence of extracellular polymeric substance (EPS) material, which contained dense accumulations of UO_2 nanoparticles as well as the MtrC and OmcA decaheme c-type cytochromes; however, the production of the EPS appeared not to be required for U(VI) reduction since OMC mutants that produced very little UO_2-EPS were surprisingly capable of reducing U(VI).[584]

5.4.1.2. Radiation-Resistant Bacteria. An original, long-standing goal of radiobiology has been to explain the acute sensitivity of most organisms to ionizing radiation (IR). Conversely, a better understanding of the radiation-resistance mechanisms developed by certain species of bacteria might aid in generating new forms of protection for humans against atomic radiation.[588] The correlation of extreme IR-resistance with high Mn(II) levels in *Deinococcus radiodurans*[589] prompted Daly et al. to investigate quantitative metal ion distributions in this species using SXRF. The results revealed a global distribution for Mn, while Fe localized primarily outside of the cytoplasm in a region overlapping the septum between dividing cells, thus supporting the idea that proteins, rather than DNA, are the principal targets of biological action by radiation.[588]

5.4.2. Aquatic Organisms

Aquatic protists, like bacteria, accumulate elements from the environment.[7] Given their active participation in the biotransformation of elements in their environment, aquatic protists maintain elemental compositions that harbor valuable information about their inorganic ecology and the ambient chemical environment. Standard bulk analytical methods, while suitable for acquiring averaged elemental compositions, are unable to provide a detailed analysis of trace element speciation in single protist cells necessary to assess their

taxonomy and trophic function. In several studies, Twining and co-workers showed that the detection limit of SXRF was sufficient for acquiring detailed, quantitative elemental maps of individual aquatic protist cells. Furthermore, the integrity of SXRF data was confirmed by atomic absorption spectroscopy (AAS) studies on bulk samples that showed no significant variations compared with SXRF data on single cells.[7,264,590−592]

In 1911, Henze reported, for the first time, surprisingly high levels of vanadium(V) in the blood cells of a Mediterranean ascidian, *Phallusia mammillata*.[585] A number of species in the Ascidiae family accumulate V in their blood cells up to 350 mM, which corresponds to a value 107 times higher than that in seawater.[585] The unusual accumulation of vanadium by ascidians, also known as tunicates or sea squirts, is particularly interesting because ascidians belong to the phylum Chordata, which signifies an evolutionary link between the Invertebrata and the Vertabrata phyla.[585] Despite substantial research efforts, questions regarding the mechanisms of vanadium accumulation and its physiological relevance in ascidians remain unanswered.[585] Evidence suggesting that vanadium accumulates in the blood cells including signet ring cells, vacuolated amoebocytes, and bivacuolated cells of the *Phallusia mammillata* ascidian species prompted Ueki et al. to use scanning SXRF to directly observe the intracellular localization of vanadium in two vanadium-rich species, *Phallusia mammillata* and *Ascidia sydneiensis samea*.[586] Results suggested, for both freeze-dried and living blood-cell samples from both species, that V distributed uniformly in the vacuoles of signet ring cells and vacuolar amoebocytes, although V concentrations were significantly lower. The data thus implied that signet ring cells are the true vanadocytes. A similar study using a combination of SXRF and XANES further confirmed the uniform distribution of V in vacuoles of signet ring cells.[587] Additionally, XANES data implied that vanadium was present in a mixture of its +III and +IV oxidation states, thereby providing evidence directly supporting earlier studies based on bulk methods.

The freshwater crustacean *Daphnia magna* represents also a frequently used model organism to study environmental metal toxicity. For example, dynamic SXRF scans and XRF computed tomography of a dried specimen provided detailed 2D and 3D elemental maps revealing the impact of Zn exposure during a period of 1 week.[593] Studies on various hard tissues of marine organisms demonstrated the application of PIXE analysis of squid statoliths[594] and octopus stylets,[595] as well as SXRF mapping of marine sediment worm jaws[596] and fish otoliths[597] for acquiring quantitative metal ion distributions. Furthermore, investigations of metal accumulation and distribution patterns in multiple species of molluscs using techniques such as SIMS, EPXMA, ESI/EELS, and AMG were recently described in an extensive review.[598]

6. Mass Spectrometry Imaging Techniques

The development of new ionization techniques, most notably electrospray ionization (ESI) and matrix-assisted laser desorption/ionization (MALDI), opened the door to the in situ mass spectrometric detection and identification of large molecules in biological specimens.[599] By combination of microprobe analysis with localized ablation and ionization of the material, a two-dimensional image can be obtained representing the molecular composition of the specimen surface. With the ability to simultaneously detect a large number of molecules, imaging mass spectrometric techniques harbor a particularly bright future in unraveling the complex network of biological systems at a molecular level. While most current efforts in imaging mass spectrometry are geared toward a comprehensive analysis of proteins, lipids, and other biomolecules in biological samples, the in situ detection of metal cations is equally possible. At present, two imaging techniques, secondary ion mass spectrometry (SIMS) and laser ablation inductively coupled plasma mass spectrometry (LA-ICPMS), have been extensively used for this purpose as illustrated with the survey provided in the next two sections.

6.1. Secondary Ion Mass Spectrometry (SIMS)

In this technique, a focused primary ion beam is utilized to eject and generate secondary ions, which are analyzed with a mass spectrometer to determine the elemental, isotopic, and molecular composition of the specimen surface. After the first prototype SIMS instrument had been described by Herzog and Viehböck in 1949,[600] the technique was further developed in the early 1960s.[601,602] SIMS is multielemental with isotopic capability, characterized by detection limits of 0.1−1 μg/g in element imaging mode. Notably, the development of the NanoSIMS 50,[603,604] a high-resolution dynamic SIMS instrument with greatly improved sensitivity and selectivity, has significantly stimulated the applications of SIMS in bioimaging (section 6.1.4). With a lateral resolution as low as 33 nm, SIMS has been extensively employed in biology[605,606] and various other disciplines, including physics, medicine, environmental studies, and forensic sciences.[607−609]

6.1.1. Metal Ion Distribution in Chromosomes

Metal cations have been implicated in the regulation of the cell cycle. Furthermore, several studies have suggested that mono- and divalent cations such as Ca(II), Mg(II), Na(I), and K(I) are pivotal in maintaining higher order chromatin structure. Given the ability to obtain in-depth analytical information for reconstructing 3D images, several SIMS studies have been devoted to investigate the role of these cations in preserving the structural integrity of chromosomes.[610] While early attempts successfully demonstrated the association of these cations with individual chromosomes,[611] the first high-resolution analytical images of the cation composition of mammalian interphase and mitotic cells were reported only in 2001.[612] This study demonstrated that the cations Ca(II), Mg(II), Na(I), and K(I) play a role in maintaining the structural integrity of chromosomes through electrostatic neutralization of DNA and are hence involved in chromosome condensation. This study also provided evidence that Ca(II) might directly interact with topoisomerase IIα, a nonhistone binding protein localized at the chromosomal axis.[613] Consistent with the above predicted role of this cation, later studies showed an increase in Ca(II) concentrations toward metaphase followed by a decrease in anaphase.[614,615] To decouple cation−DNA interactions from cation−protein interactions, dinoflagelettes, a unicellular eukaryotic algae, offer an ideal model system,[616,617] because these species are known to be devoid of histone proteins.[618] Hence, SIMS images of divalent cation distribution in dinoflagelettes further supported the anticipated role of Ca(II)

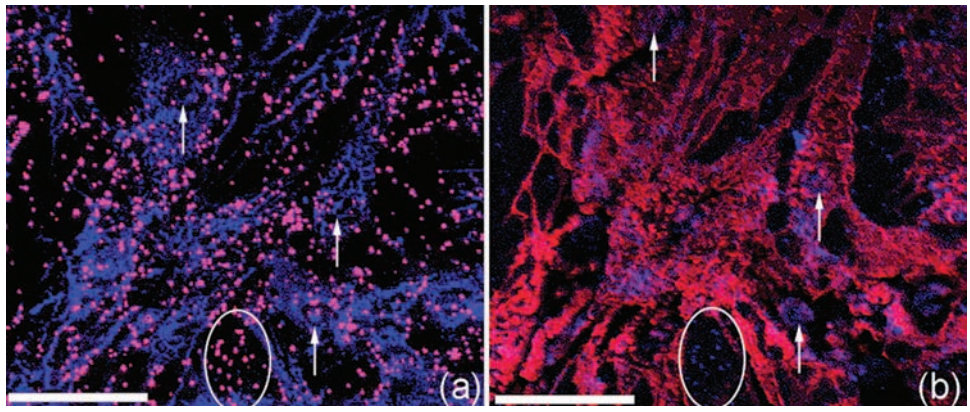

Figure 13. SIMS maps of fibroblast cells dosed with 50 ppm of dissolved Cr(III) and incubated for 7 h: (a) positive SIMS maps (blue Ca^+, red Cr^+); (b) negative SIMS maps (red CN, blue PO_2). Scale bar = 50 μm. Reprinted with permission from ref 636. Copyright 2006 Elsevier.

and Mg(II) ions to provide complete charge neutralization of DNA resulting in maximal DNA compaction.[619]

The capabilities of dynamic SIMS imaging were impressively demonstrated in a study in which karyotypes of all 46 human chromosomes were constructed based on high-resolution Ca(II) and Mg(II) SIMS images.[614] A comparison with the corresponding G-band ideograms for the complete human chromosome karyotype revealed that specific binding of Mg(II) to chromosomal "p" and "q" arm heterochromatic regions correlate with conventional G-bands. G-bands are banding patterns obtained with Giemsa stain following digestion of chromosomes with trypsin, and these bands are known to highlight AT-rich regions of chromatin. This study was further extended to investigate Ca(II) and Mg(II) banding patterns of the chromosomes of Indian muntjac deer (IMD) and BrdU-labeled polytene chromosomes from the salivary gland of the dipteran *Drosophila melanogaster*.[620] The latter study is particularly important because it revealed that the cation−DNA interaction is a fundamental process present throughout eukaryotic evolution.

6.1.2. Subcellular Distribution of Metal Ions

High-resolution SIMS measurements using stable isotope labeling have been also applied to investigate the subcellular locations of various metal ions. For example, SIMS imaging revealed the subcellular calcium stores in mammalian LLC-PK1 epithelial cells captured in interphase and various stages of mitosis.[621,622] These studies showed a redistribution of the interphase Golgi Ca(II) stores in prophase and prometaphase cells. In metaphase cells, a gradual and dynamic alignment of Ca(II) stores in both half-spindles can be observed prior to the onset of anaphase. In anaphase, the Ca(II) pool is concentrated in the spindle regions behind the daughter chromosomes and is the lowest in the central spindle region. In the telophase cells, calcium is stored in the pericentriolar material. In this study, SIMS images of $^{23}Na^+$ and $^{39}K^+$ have been also used to identify structurally damaged mitotic cells as revealed by the reduced K/Na ratios (vide infra).

SIMS has been particularly useful to elucidate the dynamics of Ca(II) transport due to its ability to simultaneously image both ^{44}Ca and ^{40}Ca isotopes within the same cell. By supplementation of the cell culture medium with ^{44}Ca, the dynamic uptake and distribution of extracellular Ca(II) was captured and distinguished from endogenous ^{40}Ca in cultured LLC-PK1 porcine kidney epithelial cells.[623] The Ca(II) distribution in healthy cells revealed higher levels of Ca(II) in the cytoplasm compared with the nucleus,[624] and the Golgi apparatus was thought to be involved in the intracellular calcium homeostasis.[625] This calcium sequestration in the Golgi apparatus has been shown to be sensitive to antigen stimulations.[626] SIMS was also useful to assess altered calcium regulation in malignant cells compared with normal cells. In a comparison between normal and breast cancer cell lines, it was observed that the thapsigargin-sensitive endoplasmic reticulum calcium pool was compromised in tumorigenic MCF-7 breast cancer cells.[627]

The analysis of a cell by SIMS imaging leads to gradual erosion of the cell surface, a feature that can be utilized for obtaining spatially resolved chemical information in three dimensions. Taking advantage of this feature, Chandra et al. explored the chemical composition of subcellular regions, such as the mitotic spindle, beneath the cell surface.[608] The study was conducted with human glioblastoma tumor cells and revealed depletion of Ca(II) stores in the metaphase spindle, thus contrasting the accumulation of Ca(II) in normal cells. In subsequent studies, these findings were utilized as a reference to assess the localization of ^{10}B atoms, used in boron neutron capture therapy (BNCT) of cancer, again in human glioblastoma tumor cells.[628−631] BNCT is based on the nuclear capture and fission reactions that occur when ^{10}B is irradiated with neutrons of the appropriate energy to yield high-energy α particles and ^7Li nuclei. In tissues, these particles have a short penetration range, and hence the success of BNCT is dependent upon the selective delivery of sufficient amounts of ^{10}B to cancer cell nuclei where they can damage DNA.[632] Thus, the determination of subcellular location of ^{10}B atoms is crucial in BNCT.

Reliable sample preparation in subcellular localization studies by SIMS is very important in order to avoid the artifactual redistribution of diffusible ions.[608,633−636] For example, Dickinson demonstrated the application of time-of-flight SIMS (TOF-SIMS) for the analysis of a frozen biological sample with submicrometer resolution (Figure 13).[636] Because cells establish gradients for diffusible elements such as Na^+ and K^+ between the intracellular and extracellular spaces, their ratio can be used as a criterion for successful sample preparation. For example, the intracellular concentrations of K^+ and Na^+ are approximately 160 mM and 15 mM, respectively, corresponding to a $^{39}K/^{23}Na$ ratio of approximately 10:1 as predicted for healthy cells.[605,637] Damaged cells have altered ionic composition due to exchange and diffusion of mobile intracellular ions with the

nutrient medium. Hence, a disturbance of the ionic distribution could be due to membrane leakage, indicating inappropriate sample preparation. An additional criterion for evaluating the state of a cell is the Ca(II) distribution, which should be low inside the cell, whereas in damaged cells, large quantities of Ca(II) can penetrate into the cytosol.[605,624]

6.1.3. Distribution of Metal Ions in Various Tissues

The ability of SIMS ion microscopy to provide subcellular images of elemental isotopes makes it suitable for studying ion transport in animal models. After injection of a stable isotope of the metal cation of interest into the bloodstream, its distribution in the tissue and cells of the target organs can be imaged with SIMS ion microscopy.

Magnesium ions are implicated in many physiological and biochemical processes, for example, as cofactor in various enzymatic reactions, particularly those catalyzed by kinases. Magnesium ions are also critical for regulating ion channels and cardiovascular functions.[638] The kidney is the primary organ for maintaining Mg(II) homeostasis in the body.[639] Killifish, a model for magnesium transport studies, were given intraperitoneal injection of ^{26}Mg(II); afterward, the isolated kidney tissue was imaged by SIMS ion microscopy.[640,641] These tracer studies showed that the renal proximal tubule is the main site of ^{26}Mg(II) transport, possibly involved in the secretion of magnesium from the fish body. These studies also indicated a probable role of the renal collecting duct in reabsorption of Mg(II) filtered in the kidney.

Intestinal epithelial cells have been implicated in dietary calcium uptake, transport, and maintainance of intracellular nontoxic levels of free calcium ions. Vitamin D has been proposed to stimulate calcium absorption in the intestine.[642] To study calcium transport and its vitamin D dependence, the stable isotope ^{44}Ca(II) was injected into the duodenal lumen of vitamin D-deficient and vitamin D-replete chickens followed by SIMS analysis of the isolated intestinal tissue.[643] In vitamin D-deficient chickens, ^{44}Ca(II) was mainly localized in the brush border region, the structure found on the apical surface of the columnar epithelial cells of the intestine, while the vitamin D-replete chickens showed normal absorption and distribution throughout the columnar cells. Based on this result, it was suggested that vitamin D increased the rate of transfer of Ca(II) from the apical to the basolateral membrane.

The capabilities of SIMS imaging were also exploited to study changes in sodium levels in the area postrema (AP) following total sleep deprivation (TSD).[644] AP is a circumventricular organ that maintains sodium homeostasis in the brain and regulates sympathetic functions.[645,646] It was expected that the sodium level in the AP would alter under TSD, a stressful condition, due to sympathetic activation. The result of the SIMS study indeed showed an increase in sodium levels in the AP region in TSD rats compared with the control group.[644]

6.1.4. NanoSIMS

With the introduction of the NanoSIMS 50 instrument by CAMECA, elemental bioimaging with a lateral resolution on the order of 50 nm combined with high sensitivity and specificity became possible. The increased resolution was achieved by orienting the primary ion beam in a normal position to the sample surface, a configuration that allowed for a much closer positioning of the primary focusing lens.[647] NanoSIMS is therefore well suited for imaging trace quantities of elements in a complex biological environment for elucidating metabolic pathways of living systems. Taking advantage of the high sensitivity, NanoSIMS has been also applied in numerous isotope tracer studies, for example, for studying the incorporation of iodine in thyroid,[648,649] the cellular distribution of melanoma targeting agents, iodobenzamide,[650,651] and the uptake of ^{131}I-labeled drugs in melanoma for developing a targeted radionuclide therapy.[652] The improved spatial resolution and sensitivity of nanoSIMS enabled imaging of uptake of isotopically labeled compounds in bacterial cells[653−655] and diatoms[656,657] at the single-cell level in order to understand microbial metabolism and to identify associated subcellular structures.[658] NanoSIMS has also been applied to biologically related geochemistry studies, for example, in elemental mapping and tracer studies of Archean fossils,[659] natural calcium carbonate samples,[660] and statoliths.[661]

Calcification of soft tissues occurs during pathological conditions and has important clinical implications. Although calcification occurs mainly in extracellular matrices,[662] calcium phosphate mineral can also deposit intracellularly. For example, Azari et al. investigated intracellular growth of hydroxyapatite (calcium phosphate) crystals in Madin−Darby canine kidney (MDCK) cells to elucidate the mechanism of intracellular calcification.[663] Elemental maps obtained using nanoSIMS were correlated with optical and electron micrographs. The correlation studies revealed that hydroxyapatite crystals grow within intracellular membrane-bound compartments and proteoglycan decorin was implicated in regulating intracellular calcification.

As discussed in section 5.2.3, iron progressively accumulates in the brain with age, as well as in brain areas affected by neurodegenerative disorders such as Alzheimer's disease (AD) and Parkinson's disease (PD).[664] Consequently, the brain becomes more vulnerable to iron-catalyzed free radical generation leading to increased oxidative stress[665] and myelin breakdown.[666] To elucidate whether iron accumulation might be due to dysfunction of the major iron-storage protein ferritin (Ft), Quintana et al. studied the subcellular distribution of iron, Ft, and hemosiderin (Hm), presumably a degradation product of Ft, in hippocampus region of AD-affected brains.[667,668] NanoSIMS was used to image the subcellular location of Fe. The resulting elemental maps were also correlated with optical and electron micrographs to identify the associated cellular structures. The study revealed that Fe-rich regions coincided with Ft or Hm rich regions observed by transmission electron microscopy (TEM). The findings suggested that Ft was dysfunctional in AD-affected brains with probable degradation to Hm and that a defect in the enzymatic oxidation of Fe inside ferritin (Ft) might be the cause of Fe accumulation in the brain to toxic levels. In a related study, Zukor et al. also combined nanoSIMS with other techniques to assess the effect of up-regulated heme oxygenase-1 (HO-1) on astroglial mitochondria.[669] Overexpression of HO-1, accumulation of Fe in astroglial mitochondria, and macroautophagy had been previously observed in AD- and PD-affected brains.[670,671] It has been proposed that overexpression of HO-1 may lead to the opening of the mitochondrial permeability transition pore in astroglia, which causes influx of Fe into the mitochondrial matrix prior to mitochondrial autophagy.

The greatly improved spatial resolution and sensitivity of nanoSIMS combined with its ability to simultaneously detect

five different ions spurred studies on an unusually broad range of biological specimens, including sea urchin teeth for understanding the structural features that enable the grinding of limestone,[672] the core of hairs from mummies discovered in the Taklamakan desert,[673] unicellular freshwater algae exposed to Cu,[674] colored hair to assess the deleterious effects of Cu and Ca when present at high concentrations,[675] and the leaves of a hyperaccumulator plant to assess the Ni localization.[676] Dauphas et al. also used nanoSIMS to investigate the ability of this technique to probe antigen−antibody recognition. In this study, an iron-containing antigen bound to an immobilized antibody was analyzed by nanoSIMS as a method to develop new antibody-based bioassays.[677]

6.2. Laser Ablation Inductively Coupled Plasma Mass Spectrometry (LA−ICP−MS)

Inductively coupled plasma mass spectrometry (ICP-MS) is one of the most widely used mass spectrometric techniques for the analysis of trace elements.[678,679] In this method, a plasma composed of ionized argon gas is used to decompose the vaporized sample into individual atomic ions, which are then separated on basis of their mass-to-charge ratio. Because the ion signal received by the detector is proportional to the initial concentration in the sample, the technique can be used for quantitative trace element speciation through calibration with known standards. Having the ability to distinguish between individual isotopes with high accuracy and precision, the technique is ideally poised for the quantitative determination of trace elements.[680] The method has been widely applied for the determination of trace elements in bulk samples, such as minerals, foods, radioactive waste, and medicinal and biological materials. With the development of new ionization techniques, improved separation systems, and more sensitive detectors, the direct in situ analysis of solid samples became possible. By using a focused laser beam, typically a Nd:YAG laser with $\lambda/4 = 266$ nm, the sample material can be directly ablated from the surface with high positional precision. The evaporated material is then transported with a carrier gas into an ICP-MS instrument for trace element analysis.[681] Since the inception of this technique in 1985,[682] laser ablation inductively coupled mass spectrometry (LA−ICP−MS) has been continuously developed and evolved into a powerful analytical method for imaging metal ion distributions in soft biological tissues.[683−686] Compared with other trace element imaging modalities, LA−ICP−MS offers a faster sample throughput while retaining high sensitivity and accuracy of the data.

The determination of trace element composition in biological samples by LA−ICP−MS was initially restricted to hard tissues, such as tree rings,[687−690] tree barks,[691] leaves,[692] teeth,[693,694] and mussel shells.[695−699] Soft tissues posed major challenges due to their high water content, which led to inefficient ablation and substantial sample alterations in commercially available ablation chambers. The problem was successfully addressed by Feldmann et al., who specifically designed a cryogenically cooled cell that allowed tissue ablation at temperatures below −60 °C.[700] The instrument allowed for the first time the direct analysis of soft tissue with 2−6% reproducibility and a spatial resolution of better than 200 μm. The same authors later used the technique to map the two-dimensional distribution of zinc and copper in thin sections of sheep liver with a focal spot size of 250 μm.[701] The approach was suitable to discern zonation of copper at very low concentrations. By using a further improved cooled ablation chamber, Becker et al. were able to map the two-dimensional elemental distribution in 20 μm thin sections of human brain tissue with a resolution of 50 μm.[702] A double focusing sector field ICP-MS allowed for simultaneous quantitation of ^{31}P, ^{32}S, ^{56}Fe, ^{63}Cu, ^{64}Zn, ^{232}Th, and ^{238}U in the hippocampus region. The data revealed an inhomogeneous layered structure of P, S, Cu, and Zn, while Th and U were more homogeneously distributed at much lower concentrations. In a similar study, LA−ICP−MS was used to detect differences in the trace element composition of rat brain tissue containing an implanted small-sized tumor.[703] The mass spectrometric data revealed lower concentrations of Cu and Zn in and around the tumor region compared with control tissue.

Stimulated by these early successes, LA−ICP−MS has evolved into a powerful microanalytical imaging technique and has been applied to an increasingly wider range of biological research fields, including trace element speciation in tissues, the imaging of xenobiotic probes and metal-containing drugs, proteomics, and environmental toxicology.[684] The following section offers an overview of recent developments organized according to topical areas.

6.2.1. Elemental Distribution in Brain Tissue

As a potentially complementary technique to focused ion beam methods, quadrupole LA−ICP−MS was applied to multielemental mapping of 100-μm-thick sections of rat brain tissue.[704] With a laser spot size of 60 μm and scan rate of 120 μm s^{-1}, the Cu, Zn, and Fe distribution in a whole 1 cm^2 thin section was quantitatively imaged within 2 h. In order to determine the reproducibility of LA−ICP−MS for quantifying trace elements in brain tissue, Zoriy et al. analyzed five neighboring thin sections of 20 μm thickness prepared from the same human brain tissue.[705] Depending on the analyzed element, a reproducibility in the range between 5% and 8% was reported. The reproducibility of a homogeneous synthetic standard ranged between 2.2% and 3.5%. Very distinct distribution patterns were found for Zn, Cu, and Pb in LA−ICP−MS raster scans of three different areas of healthy human brain tissue, the insular, central, and hippocampal regions.[706] Consistent with earlier reports, the highest concentrations of Zn and Cu along with the most distinct distribution pattern were found in the hippocampus (Figure 14). The distribution of Pb was found to be rather homogeneous for all three brain regions.

In a similar study, a distinctly different distribution of Cu, Zn, Pb, and U was found in tissue sections with brain tumor compared with adjacent healthy brain tissue.[707] To autoradiographically delineate the tumor area from healthy tissue, the sections were exposed to various tritium-labeled ligands specific toward receptors that are up-regulated in gliomas. Brain tissue exposed to cultured tumor cells revealed higher concentrations of Cu and Zn compared with control tissue, while P, S, and Fe were depleted.[708] To identify regions that preferentially bind to toxic metals, Becker et al. incubated rat brain postmortem tissue with uranium or neodinium salts at a concentration of 100 μg/g for 3 h.[709] Elemental maps acquired by LA−ICP−MS revealed that both metals have a high affinity toward white matter and low affinity toward gray matter. Analysis of the uranium isotope ratio ^{235}U/^{238}U revealed a structureless uniform distribution corresponding to the natural isotope ratio.

Besides the trace metal analysis of brain tumors, LA−ICP−MS has been also applied to investigate the contents

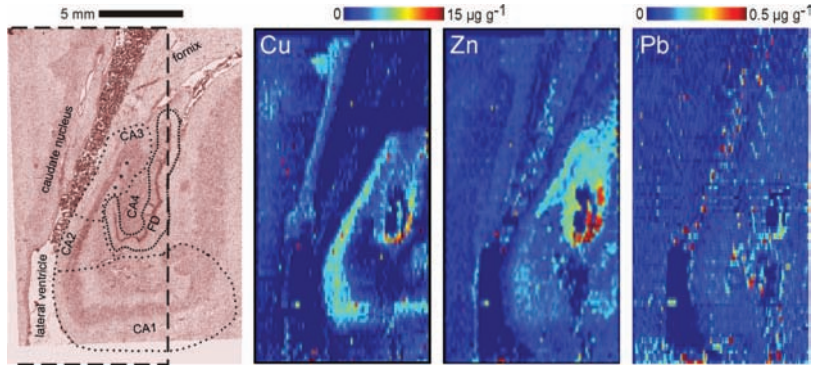

Figure 14. Distribution of Zn, Cu, and Pb in the hippocampus region measured by LA−ICP−MS. In a light photomicrograph (left) of an adjacent section stained by cresyl violet cortical regions are labeled (FC, fascia dentata circumscribed by a densely dotted line; CA1−4, cornu ammonis, part 1−4 circumscribed by loosely dotted lines, respectively; asterisks, stratum lucidum of CA3). Borders between these areas were determined by optical inspection. The dashed box open to the left indicates the overlap of the LA−ICP−MS images with this photomicrograph. Reprinted with permission from ref 706. Copyright 2008 Elsevier.

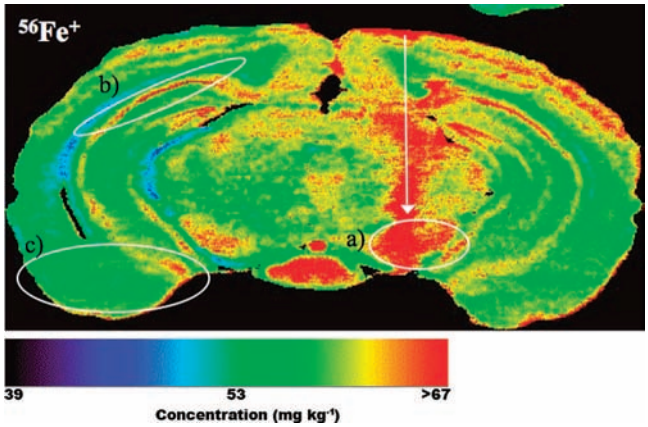

Figure 15. Quantitative ^{56}Fe imaging of 6-OHDA lesioned mouse brain at the level of the SN using LA−ICP−MS: (a) substantia nigra, (b) dentate gyrus, (c) amygdala and hippocampus. The needle track is shown by the white arrow. Reprinted with permission from ref 711. Copyright 2009 Royal Society of Chemistry.

of amyloid plaques in the brain tissue of a transgenic mouse model of Alzheimer's disease.[710] By using Eu- and Ni-conjugated antibodies against the amyloid precursor protein Aβ peptide, plaque deposits were identified and their elemental composition simultaneously determined. Consistent with PIXE and SXRF studies (see section 5.2.3), the data revealed increased concentrations of Cu, Fe, Zn, and Mg in plaques compared with surrounding nonplaque tissue. Consistent with earlier SXRF imaging reports (section 5.2.3.2), LA−ICP−MS revealed elevated Fe concentrations within the SN of mouse brain tissue, which was subjected to the neurotoxin 6-hydroxydopamine, a common animal model for Parkinsonism (Figure 15).[711] Accurate trace metal quantifications were achieved with matrix-matched tissue standards. The findings further underscore the importance of iron in understanding the mechanism of oxidative stress and cell death in Parkinson's disease.

6.2.2. Tumor Analysis in Various Tissues

Elemental mapping by LA−ICP−MS provided insights into differences between melanoma and adjacent nontumorous tissues.[712] The concentration of ^{31}P was substantially elevated within the tumor regions, a finding that was confirmed by histochemical staining and utilized to delineate the tumor boundary (Figure 16). The data revealed a marked increase in the ^{31}P/^{34}S ratio in the peritumoral lymphoid tissue compared with the metastatic tumor. The ^{31}P/^{66}Zn ratio decreased beyond the tumor boundary, indicating distinct biochemical changes of the peritumoral lymphoid tissue in response to the tumor.

6.2.3. Xenobiotic Elemental Labeling

To assess the utility of antibodies labeled with xenobic elemental tags in LA−ICP−MS, Seuma et al. imaged the distribution of two breast cancer-associated proteins in tissue sections.[713] With a focal diameter of 5 μm, the raster scan resolution and sensitivity was sufficient for fine scale mapping at the cellular level and allowed for quantitative assessment of the marker protein expression levels.

While the majority of soft tissue analysis by LA−ICP−MS has been devoted to elemental mapping of brain and tumor tissues, a recent report explored 14 μm thin sections of kidney tissue from a mouse treated with cisplatin. Ion intensities of ^{63}Cu, ^{64}Zn, and ^{196}Pt were simultaneously measured with 50 μm resolution, showing an inhomogeneous distribution with Cu enriched in the capsule and outer cortex, Zn in the inner cortex, and Pt in the medulla.[714] Most recently, LA−ICP−MS has been used to image deposits of calcium phosphate based crystals in knee cartilage and synovial fluid from arthritic patients.[715] Crystal deposits produced areas with high calcium and phosphorus intensities, which were observed for both the cartilage and synovial fluid samples. Further development of this technique will directly benefit the diagnosis of crystal-associated arthritis.

6.2.4. Environmental Toxicology

A detailed understanding of the distribution and accumulation of chemicals in the ecosystem is of critical importance to assess their environmental impact and potential toxic effects. LA−ICP−MS offers also the opportunity to directly quantify xenobiotic elements combined with naturally occurring trace elements at low levels in a wide range of organisms. For example, to test whether LA−ICP−MS is suitable for mapping of Se at the submicrogram per gram level in soft tissue, slugs were fed with either a placebo or solutions containing 1 mg/L selenium.[716] Longitudinal sections of 100 μm thickness revealed inhomogeneous distributions for Se as well as C, Cu, and Zn. The Se-treated animals showed Se enriched in the kidney and in the digestive gland compared with controls.

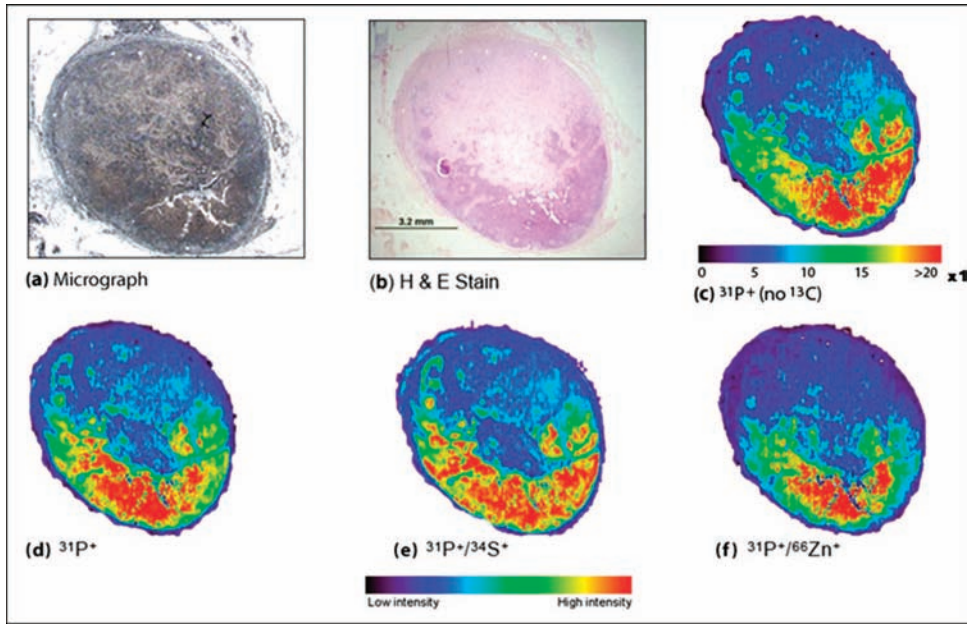

Figure 16. Sentinel lymph node partly replaced by metastatic melanoma (upper two-thirds of the ovoid-shaped lymph node): (a) photograph of slice before elemental imaging; (b) H&E stain; (c) $^{31}P^+$ image without ^{13}C normalization; (d) $^{31}P^+$ image; (e)$^{31}P^+/^{34}S^+$; (f) $^{31}P^+/^{66}Zn^+$. Reprinted with permission from ref 712. Copyright 2009 Royal Society of Chemistry.

A recent report explored the utility of LA−ICP−MS for quantitative imaging of nutrient and toxic trace elements in plants.[717] The leaves of the copper-tolerant plant *Elsholtzia splendens*, usually found in Cu mining areas of southern China, were imaged in order to study accumulation and distribution of trace metals.[718,719] The uptake and distribution of Cu was investigated by incubation with enriched ^{65}Cu isotope as tracer. Unsectioned leaves were directly analyzed by LA−ICP−MS and showed Cu accumulation via the petiole and main veins in the leaves concluding from the increased $^{65}Cu/^{63}Cu$ ratios.[718] The Cu-induced stress led also to accumulation of K, Mg, Mn, P, and S in the newly formed leaves. Similarly, the accumulation and distribution of Ag and Cu was studied in leaves of *Helianthus annuss L.* treated with 1 mM $AgNO_3$ for five days.[720]

6.2.5. Isotope Ratio Measurements

The ability to determine isotope ratios opens the door to a range of applications that are not accessible to X-ray imaging techniques. For example, the dynamics of trace element transport and distribution in biological systems can be analyzed through tracer studies with highly enriched isotopes, or the measurement of isotope ratio changes as a result of nuclear decay may offer geochronological insights over very long time scales.[721] For example, Becker and coworkers developed a staining technique based on isotope ratio measurement of $^{145}Nd/^{146}Nd$ and applied this to thin rat brain tissue section, which can be used to study different substructures of the brain.[722] In a similar study, LA−ICP−MS was employed to study heavy metal distribution in brain tissues for toxicological screening on the basis of determination of ion intensities for different isotopes of U and Nd.[709]

6.2.6. Near-Field Laser Ablation

To improve the lateral resolution of LA−ICP−MS, Becker et al. have explored near-field enhancement effects of laser radiation at the sharp tip of a thin silver needle.[723−725] Depending on the sample-to-tip distance, the observed laser craters ranged from 200 nm to 2 μm in diameter.[725] Meyer et al. recently described nanoscale surface sampling with a scanning setup that produced surface craters as small as 50 nm in diameter.[726] While, at present, the near-field ablation technique has not been applied for nanoscopic imaging of biological specimens, these recent developments indicate that that LA−ICP−MS has the potential to evolve into a routine microanalytical method that might offer similar sensitivity and spatial resolution compared with synchrotron-based microprobe instruments but at a small fraction of the costs.

7. Conclusions

Over the past decade, the capabilities of microanalytical imaging techniques have rapidly evolved. Most imaging techniques are now accessible to the biologist for routine analysis of the trace element composition of a broad range of biological samples. The combination of various imaging modalities, each with its own specific strengths, harbors particularly great potential for expanding the understanding of the complex interplay between metal cations and their biological environment. The ability to perform in situ speciation analysis of redox-active metals has already provided a wealth of intriguing insights into cellular redox cycles. This information is of particular importance in understanding fundamental aspects of disease progressions as well as the toxicology of xenobiotics. The recent development in mass spectrometric techniques are particularly exciting, considering future possibilities of analyzing simultaneously the trace element composition as well as the distribution of small molecule metabolites and proteins at the tissue and potentially subcellular level.

8. Acknowledgments

We gratefully thank the National Institutes of Health (Grants NIGMS/NIDDK, GM067169, DK68096) for funding our research on developing fluorescence probes and imaging tools for elucidating the inorganic physiology of trace metals in biological systems.

9. References

(1) Li, Y. F.; Chen, C. Y.; Qu, Y.; Gao, Y. X.; Li, B.; Zhao, Y. L.; Chai, Z. F. *Pure Appl. Chem.* **2008**, *80*, 2577.
(2) Ascone, I.; Strange, R. *J. Synchrotron Radiat.* **2009**, *16*, 413.
(3) Finney, L. A.; O'Halloran, T. V. *Science* **2003**, *300*, 931.
(4) Bush, A. I. *Curr. Opin. Chem. Biol.* **2000**, *4*, 184.
(5) Perls, M. *Virchows Arch. Pathol. Anat.* **1867**, *39*, 42.
(6) Lobinski, R.; Moulin, C.; Ortega, R. *Biochimie* **2006**, *88*, 1591.
(7) Twining, B. S.; Baines, S. B.; Vogt, S.; de Jonge, M. D. *J. Eukaryot. Microbiol.* **2008**, *55*, 151.
(8) Cheon, J.; Lee, J. H. *Acc. Chem. Res.* **2008**, *41*, 1630.
(9) Barthe, N.; Chatti, K.; Coulon, P.; Maitrejean, S.; Basse-Cathalinat, B. *Nucl. Instrum. Methods Phys. Res., Sect. A* **2004**, *527*, 41.
(10) Goldschmidt, J.; Zuschratter, W.; Scheich, H. *Neuroimage* **2004**, *23*, 638.
(11) Powell, R. D.; Pettay, J. D.; Powell, W. C.; Roche, P. C.; Grogan, T. M.; Hainfeld, J. F.; Tubbs, R. R. *Hum. Pathol.* **2007**, *38*, 1145.
(12) Giepmans, B. N. G.; Adams, S. R.; Ellisman, M. H.; Tsien, R. Y. *Science* **2006**, *312*, 217.
(13) Pearse, A. G. E. *Histochemistry. Theoretical and Applied*; 4th ed.; Churchill Livingstone: Edinburgh, 1980.
(14) Grohe, F. *Virchows Arch. Pathol. Anat.* **1861**, *20*, 306.
(15) Gömöri, G. *Am. J. Pathol.* **1936**, *12*, 655.
(16) Lillie, R. D. *Histopathologic Technic*; Blakiston: Philadelphia-Toronto, 1948.
(17) Lison, L. *Histochimie Animale, Methodes et Problemes*; Gauthier-Viallrs: Paris, 1936.
(18) Nguyen-Legros, J.; Bizot, J.; Bolesse, M.; Pulicani, J.-P. *Histochemistry* **1980**, *66*, 239.
(19) Schmeltzer, W. *Z. Wiss. Mikrosk.* **1933**, *50*, 99.
(20) Yu, S.; Iwatsuki, H.; Ichinohe, N.; Mori, F.; Shoumura, K. *Neurosci. Lett.* **2001**, *308*, 70.
(21) Meguro, R.; Asano, Y.; Odagiri, S.; Li, C.; Iwatsuki, H.; Shoumura, K. *Arch. Histol. Cytol.* **2005**, *68*, 171.
(22) Meguro, R.; Asano, Y.; Iwatsuki, H.; Shoumura, K. *Histochem. Cell Biol.* **2003**, *120*, 73.
(23) Quincke, H. *Arch. Exp. Pathol. Pharmakol.* **1896**, *37*, 183.
(24) Meguro, R.; Asano, Y.; Odagiri, S.; Li, C.; Iwatsuki, H.; Shoumura, K. *Arch. Histol. Cytol* **2007**, *70*, 1.
(25) Boyce, R.; Herdmann, W. A. *Philos. Trans. London* **1897**−**1898**, *62*, 34.
(26) Mendel, L. B.; Bradley, H. C. *Am. J. Physiol.* **1905**, *14*, 313.
(27) Mallory, F. B.; Parker, F. J. *Am. J. Pathol.* **1939**, *15*, 517.
(28) Okamoto, K.; Utamura, M. *Trans. Soc. Pathol. Jpn.* **1938**, *20*, 573.
(29) Feigl, F.; Anger, V. *Spot Tests in Inorganic Analysis*; Elsevier: Amsterdam, 1972.
(30) Green, C. L. *Am. J. Pathol.* **1955**, *31*, 545.
(31) Uzman, L. L. *Lab. Invest.* **1956**, *5*, 299.
(32) Butt, E. M.; Nusbaum, R. E.; Gilmour, T. C.; Didio, S. L. *Am. J. Clin. Pathol* **1958**, *30*, 479.
(33) Lecca, S.; Pilloni, L.; Faa, G. *Eur. J. Morphol.* **2001**, *39*, 145.
(34) Okamoto, K.; Utamura, M.; Mikami, G. *Trans. Soc. Pathol. Jpn.* **1938**, *22*, 348.
(35) Okamoto, K.; Utamura, M.; Akagi, G. *Trans. Soc. Pathol. Jpn.* **1939**, *22*, 361.
(36) Irons, R. D.; Schenk, E. A.; Lee, J. C. *Arch. Pathol. Lab. Med.* **1977**, *101*, 298.
(37) Waterhouse, D. F. *Bull. Counc. Sci. Ind. Res. Aust.* **1945**, *191*, 7.
(38) Waterhouse, D. F. *Bull. Counc. Sci. Ind. Res. Aust.* **1945**, *191*, 21.
(39) Howell, J. S. *J. Pathol. Bacteriol.* **1959**, *77*, 473.
(40) Sandell, E. B. *Colorimetric Determination of Traces of Metals*; Wiley: New York, 1959.
(41) Shikata, T.; Uzawa, T.; Yoshiwara, N.; Akatsuka, T.; Yamasaki, S. *Jpn. J. Exp. Med.* **1974**, *44*, 25.
(42) Jain, S.; Scheuer, P. J.; Archer, B.; Newman, S. P.; Sherlock, S. *J. Clin. Path.* **1978**, *31*, 784.
(43) Sipponen, P.; Salaspuro, M. P.; Makkonen, H. M. *Ann. Clin. Res.* **1975**, *7*, 273.
(44) Salaspuro, M.; Sipponen, P. *Gut* **1976**, *17*, 787.
(45) Jain, S.; Scheuer, P. J.; Archer, B.; Newman, S. P.; Sherlock, S. *J. Clin. Pathol.* **1978**, *31*, 784.
(46) Gomori, G. *Microscopic Histochemistry*; Chicago University Press: Chicago, IL, 1952.
(47) Sebruyns, M. *C. R. Soc. Biol. Paris* **1946**, *140*, 1141.
(48) Szerdahelyi, P.; Kasa, P. *Int. Rev. Cytol.* **1984**, *89*, 1.
(49) Frederickson, C. J. *Int. Rev. Neurobiol.* **1989**, *31*, 145.
(50) Okamoto, K. *Trans. Soc. Pathol. Jpn.* **1943**, *33*, 247.
(51) Okamoto, K. *Trans. Soc. Pathol. Jpn.* **1942**, *32*, 99.
(52) Okamoto, K.; Aoyama, T.; Ibaraki, H.; Narumi, M.; Shibata, Y.; Kawasaki, D.; Shibata, A.; Komatsu, K. *Hyogo J. Med. Sci.* **1951**, *1*, 77.
(53) Wolff, H.; Ringler, D. *Z. Ges. Exp. Med.* **1954**, *124*, 236.
(54) Fleischhauer, K.; Horstmann, E. *Z. Zellforsch.* **1957**, *46*, 598.
(55) Danscher, G.; Shipley, M. T.; Anderson, P. *Brain Res.* **1975**, *85*, 522.
(56) Frederickson, C. J.; Howell, G. A.; Frederickson, M. H. *Exp. Neurol.* **1981**, *73*, 812.
(57) McNary, W. F. J. *J. Histochem. Cytochem.* **1954**, *2*, 185.
(58) Mager, M.; McNary, W. F. J.; Lionetti, F. *J. Histochem. Cytochem.* **1953**, *1*, 493.
(59) McNary, W. F. *Blood* **1957**, *12*, 644.
(60) Shima, C.; Tsunoda, K.-i.; Akaiwa, H.; Suzuku, K.; Nakajima, K. *Anal. Biochem.* **1996**, *236*, 173.
(61) Maske, H. *Naturwissenschaften* **1955**, *42*, 424.
(62) Frederickson, C. J.; Howell, G. A. *The Neurobiology of Zinc*; Alan R. Liss: New York, 1984.
(63) Yanagida, T.; Ishii, Y. *Single Molecule Dynamics in Life Science*; Wiley-VCH: Weinheim, Germany, 2009.
(64) Que, E. L.; Domaille, D. W.; Chang, C. J. *Chem. Rev.* **2008**, *108*, 1517.
(65) Domaille, D. W.; Que, E. L.; Chang, C. J. *Nat. Chem. Biol.* **2008**, *4*, 168.
(66) deSilva, A. P.; Gunaratne, H. Q. N.; Gunnlaugsson, T.; Huxley, A. J. M.; McCoy, C. P.; Rademacher, J. T.; Rice, T. E. *Chem. Rev.* **1997**, *97*, 1515.
(67) Valeur, B.; Leray, I. *Coord. Chem. Rev.* **2000**, *205*, 3.
(68) Rurack, K. *Spectrochim. Acta, Part A* **2001**, *57*, 2161.
(69) Kim, H. N.; Lee, M. H.; Kim, H. J.; Kim, J. S.; Yoon, J. *Chem. Soc. Rev.* **2008**, *37*, 1465.
(70) Kimura, E.; Aoki, S. *Biometals* **2001**, *14*, 191.
(71) Kimura, E.; Koike, T. *Chem. Soc. Rev.* **1998**, *27*, 179.
(72) Jiang, P. J.; Guo, Z. J. *Coord. Chem. Rev.* **2004**, *248*, 205.
(73) Kikuchi, K.; Komatsu, K.; Nagano, T. *Curr. Opin. Chem. Biol.* **2004**, *8*, 182.
(74) Lim, N. C.; Freake, H. C.; Bruckner, C. *Chem.*−*Eur. J.* **2005**, *11*, 38.
(75) Thompson, R. B. *Curr. Opin. Chem. Biol.* **2005**, *9*, 526.
(76) Carol, P.; Sreejith, S.; Ajayaghosh, A. *Chem.*−*Asian J.* **2007**, *2*, 338.
(77) Nolan, E. M.; Lippard, S. J. *Acc. Chem. Res.* **2009**, *42*, 193.
(78) Nolan, E. M.; Lippard, S. J. *Chem. Rev.* **2008**, *108*, 3443.
(79) Mahanand, D.; Houck, J. C. *Clin. Chem.* **1968**, *14*, 6.
(80) Watanabe, S.; Frantz, W.; Trottier, D. *Anal. Biochem.* **1963**, *5*, 345.
(81) Hahn von Dorsche, H.; Fiedler, H. *Acta Histochem.* **1970**, *39*, 359.
(82) Toroptsev, I. V.; Eshchenko, V. A. *Tsitologiya* **1970**, *12*, 1481.
(83) Toroptsev, I. V.; Eshchenko, V. A. *Bull. Exp. Biol. Med.* **1971**, *72*, 118.
(84) Eshchenko, V. A. *Tsitologiya* **1978**, *55*, 27.
(85) Toroptsev, I. V.; Eshchenko, V. A. *Farmakol. Toksikol.* **1982**, *45*, 82.
(86) Frederickson, C. J. *Int. Rev. Neurobiol.* **1989**, *31*, 145.
(87) Frederickson, C. J.; Kasarskis, E. J.; Ringo, D.; Frederickson, R. E. *J. Neurosci. Methods* **1987**, *20*, 91.
(88) IMahadevan, I. B.; Kimber, M. C.; Lincoln, S. F.; Tiekink, E.; Ward, A. D.; Betts, W. H.; Forbes, I. J.; Zalewski, P. D. *Aust. J. Chem.* **1996**, *49*, 561.
(89) Coyle, P.; Zalewski, P. D.; Philcox, J. C.; Forbes, I. J.; Ward, A. D.; Lincoln, S. F.; Mahadevan, I.; Rofe, A. M. *Biochem. J.* **1994**, *303*, 781.
(90) Zalewski, P. D.; Millard, S. H.; Forbes, I. J.; Kapaniris, O.; Slavotinek, O.; Betts, W. H.; Ward, A. D.; Lincoln, S. F.; Mahadevan, I. *J. Histochem. Cytochem.* **1994**, *42*, 877.
(91) Zalewski, P. D.; Forbes, I. J.; Betts, W. H. *Biochem. J.* **1993**, *296*, 403.
(92) Wellenreuther, G.; Cianci, M.; Tucoulou, R.; Meyer-Klaucke, W.; Haase, H. *Biochem. Biophys. Res. Commun.* **2009**, 198.
(93) Hirano, T.; Kikuchi, K.; Urano, Y.; Higuchi, T.; Nagano, T. *J. Am. Chem. Soc.* **2000**, *122*, 12399.
(94) Hirano, T.; Kikuchi, K.; Urano, Y.; Nagano, T. *J. Am. Chem. Soc.* **2002**, *124*, 6555.
(95) Komatsu, K.; Kikuchi, K.; Kojima, H.; Urano, Y.; Nagano, T. *J. Am. Chem. Soc.* **2005**, *127*, 10197.
(96) Chang, C. J.; Nolan, E. M.; Jaworski, J.; Burdette, S. C.; Sheng, M.; Lippard, S. J. *Chem. Biol.* **2004**, *11*, 203.
(97) Frederickson, C. J.; Burdette, S. C.; Sensi, S. L.; Weiss, J. H.; Yin, H. Z.; Balaji, R. V.; Truong-Tran, A. Q.; Bedell, E.; Prough, D. S.; Lippard, S. J. *J. Neurosci. Methods* **2004**, *139*, 79.
(98) Burdette, S. C.; Frederickson, C. J.; Bu, W. M.; Lippard, S. J. *J. Am. Chem. Soc.* **2003**, *125*, 1778.
(99) Grynkiewicz, G.; Poenie, M.; Tsien, R. Y. *J. Biol. Chem.* **1985**, *260*, 3440.
(100) Komatsu, K.; Urano, Y.; Kojima, H.; Nagano, T. *J. Am. Chem. Soc.* **2007**, *129*, 13447.
(101) Kim, H. M.; Seo, M. S.; An, M. J.; Hong, J. H.; Tian, Y. S.; Choi, J. H.; Kwon, O.; Lee, K. J.; Cho, B. R. *Angew. Chem., Int. Ed.* **2008**, *47*, 5167.

(102) Sumalekshmy, S.; Henary, M. M.; Siegel, N.; Lawson, P. V.; Wu, Y.; Schmidt, K.; Bredas, J. L.; Perry, J. W.; Fahrni, C. J. *J. Am. Chem. Soc.* **2007**, *129*, 11888.
(103) Tang, B.; Huang, H.; Xu, K.; Tong, L.; Yang, G.; Liu, X.; An, L. *Chem. Commun.* **2006**, 3609.
(104) Kiyose, K.; Kojima, H.; Urano, Y.; Nagano, T. *J. Am. Chem. Soc.* **2006**, *128*, 6548.
(105) Atilgan, S.; Ozdemir, T.; Akkaya, E. U. *Org. Lett.* **2008**, *10*, 4065.
(106) Rurack, K.; Resch-Genger, U. *Chem. Soc. Rev.* **2002**, *31*, 116.
(107) Yang, L. C.; McRae, R.; Henary, M. M.; Patel, R.; Lai, B.; Vogt, S.; Fahrni, C. J. *Proc. Natl. Acad. Sci. U.S.A.* **2005**, *102*, 11179.
(108) Zeng, L.; Miller, E. W.; Pralle, A.; Isacoff, E. Y.; Chang, C. J. *J. Am. Chem. Soc.* **2006**, *128*, 10.
(109) Bricks, J. L.; Kovalchuk, A.; Trieflinger, C.; Nofz, M.; Büschel, M.; Tolmachev, A. I.; Daub, J.; Rurack, K. *J. Am. Chem. Soc.* **2005**, *127*, 13522.
(110) Yu, M.; Shi, M.; Chen, Z.; Li, F.; Li, X.; Gao, Y.; Xu, J.; Yang, H.; Zhou, Z.; Yi, T.; Huang, C. *Chem.—Eur. J.* **2008**, *14*, 6892.
(111) Zhang, M.; Gao, Y.; Li, M.; Yu, M.; Li, F.; Li, L.; Zhu, M.; Zhang, J.; Yi, T.; Huang, C. *Tetrahedron Lett.* **2007**, *48*, 3709.
(112) Danscher, G.; Stoltenberg, M. *Prog. Histochem. Cytochem.* **2006**, *41*, 57.
(113) Gallyas, F. *Acta Morphol. Acad. Sci. Hung.* **1971**, *19*, 57.
(114) Gallyas, F. *Stain Technol.* **1979**, *54*, 173.
(115) Danscher, G. *Histochemistry* **1981**, *71*, 81.
(116) Danscher, G. *Histochemistry* **1981**, *71*, 1.
(117) Danscher, G.; Stoltenberg, M. *Prog. Histochem. Cytochem.* **2006**, *41*, 57.
(118) Timm, F. *Histochemie* **1960**, *2*, 150.
(119) Timm, F. *Dtsch. Z. Ges. Gerichtl. Med.* **1958**, *46*, 706.
(120) Haug, F. M. S. *Adv. Anat. Embryol. Cell Biol.* **1973**, *47*, 1.
(121) Cole, T. B.; Wenzel, H. J.; Kafer, K. E.; Schwartzkroin, P. A.; Palmiter, R. D. *Proc. Natl. Acad. Sci. U.S.A.* **1999**, *96*, 1716.
(122) Wenzel, H. J.; Cole, T. B.; Born, D. E.; Schwartzkroin, P. A.; Palmiter, R. D. *Proc. Natl. Acad. Sci. U.S.A.* **1997**, *94*, 12676.
(123) Danscher, G.; Stoltenberg, M. *J. Histochem. Cytochem.* **2005**, *53*, 141.
(124) Danscher, G. *Histochem. J.* **1996**, *28*, 361.
(125) Danscher, G. *Histochemistry* **1982**, *76*, 281.
(126) Christensen, M. K.; Frederickson, C. J.; Danscher, G. *J. Histochem. Cytochem.* **1992**, *40*, 575.
(127) Rau, R. *Clin. Rheumatol.* **2005**, *24*, 189.
(128) Danscher, G.; Hansen, H. J.; Mollermadsen, B. *Histochemistry* **1984**, *81*, 283.
(129) Mollermadsen, B.; Mogensen, S. C.; Danscher, G.; Rungby, J.; Thorlaciussussing, O.; Graudal, H. *Int. J. Tissue React.: Exp. Clin. Aspects* **1985**, *7*, 439.
(130) Mollermadsen, B.; Thorlaciussussing, O. *Exp. Mol. Pathol.* **1984**, *41*, 74.
(131) Mollermadsen, B.; Danscher, G. *Exp. Mol. Pathol.* **1983**, *39*, 327.
(132) Danscher, G. *Histochem. Cell Biol.* **2002**, *117*, 447.
(133) Danscher, G.; Hacker, G. W.; Grimelius, L.; Norgaard, J. O. R. *J. Histotechnol.* **1993**, *16*, 201.
(134) Danscher, G. *Histochemistry* **1981**, *71*, 177.
(135) Danscher, G. *Histochemistry* **1984**, *81*, 331.
(136) Danscher, G.; Mollermadsen, B. *J. Histochem. Cytochem.* **1985**, *33*, 219.
(137) Mollermadsen, B.; Danscher, G. *Toxicol. Appl. Pharmacol.* **1991**, *108*, 457.
(138) Mollermadsen, B. *Toxicol. Appl. Pharmacol.* **1990**, *103*, 303.
(139) Ross, J. F.; Switzer, R. C.; Poston, M. R.; Lawhorn, G. T. *Brain Res.* **1996**, *725*, 137.
(140) Danscher, G.; Stoltenberg, M.; Kemp, K.; Pamphlett, R. *J. Histochem. Cytochem.* **2000**, *48*, 1503.
(141) Pilloni, L.; Lecca, S.; Van Eyken, P.; Flore, C.; Demelia, L.; Pilleri, G.; Nurchi, A. M.; Farci, A. M. G.; Ambu, R.; Callea, F.; Faa, G. *Histopathology* **1998**, *33*, 28.
(142) Goldfischer, S.; Sternlieb, I. *Am. J. Pathol.* **1968**, *53*, 883.
(143) Sato, M.; Ohtomo, K.; Daimon, T.; Sugiyama, T.; Iijima, K. *J. Histochem. Cytochem.* **1994**, *42*, 1585.
(144) Schell, H.; Hornstein, O. P. *Acta Histochem.* **1974**, *48*, 232.
(145) Kozma, M.; Szerdahelyi, P.; Kasa, P. *Acta Histochem.* **1981**, *62*, 142.
(146) Szerdahelyi, P.; Kasa, P. *Histochemistry* **1986**, *95*, 349.
(147) Niese, S. *Czech. J. Phys.* **2006**, *56*, D3.
(148) Hevesy, G. V.; Paneth, F. *Z. Anorg. Chem.* **1913**, *82*, 323.
(149) Hevesy, G. V. *Biochem. J.* **1923**, *17*, 439.
(150) Rogers, A. W. *Techniques of Autoradiography*; Elsevier: Amsterdam, 1979.
(151) Niepce de Saint-Victor, M. *Comp. Rend.* **1867**, *65*, 505.
(152) Caro, L. G. *J. Cell. Biol.* **1962**, *15*, 173.
(153) Takeda, A. *Brain Res. Rev.* **2000**, *34*, 137.
(154) Takeda, A. *Biometals* **2001**, *14*, 343.
(155) Pullen, R. G. L.; Franklin, P. A.; Hall, G. H. *Neurochem. Res.* **1990**, *15*, 1003.
(156) Pullen, R. G. L.; Franklin, P. A.; Hall, G. H. *J. Neurochem.* **1991**, *56*, 485.
(157) Franklin, P. A.; Pullen, R. G. L.; Hall, G. H. *Neurochem. Res.* **1992**, *17*, 767.
(158) Frederickson, C. J.; Hernandez, M. D.; Goik, S. A.; Morton, J. D.; McGinty, J. F. *Brain Res.* **1988**, *446*, 383.
(159) Takeda, A.; Akiyama, T.; Sawashita, J.; Okada, S. *Brain Res.* **1994**, *640*, 341.
(160) Takeda, A.; Sawashita, J.; Okada, S. *Brain Res.* **1994**, *658*, 252.
(161) Takeda, A.; Sawashita, J.; Okada, S. *Brain Res.* **1995**, *695*, 53.
(162) Paoletti, P.; Vergnano, A. M.; Barbour, B.; Casado, M. *Neuroscience* **2009**, *158*, 126.
(163) Harris, W. R.; Keen, C. *J. Nutr.* **1989**, *119*, 1677.
(164) Takeda, A.; Kawai, M.; Okada, S. *Brain Res.* **1997**, *769*, 193.
(165) Nagase, S.; Shimamune, K. *Science* **1979**, *205*, 590.
(166) Takeda, A.; Suzuki, M.; Okada, S.; Oku, N. *J. Health Sci.* **2000**, *46*, 209.
(167) Takeda, A.; Suzuki, M.; Okada, S.; Oku, N. *Brain Res.* **2000**, *863*, 241.
(168) Takeda, A.; Takefuta, S.; Ijiro, H.; Okada, S.; Oku, N. *Brain Res. Bull.* **1999**, *49*, 453.
(169) Takeda, A.; Suzuki, M.; Oku, N. *Biometals* **2002**, *15*, 371.
(170) Golub, M. S.; Keen, C. L.; Gershwin, M. E.; Hendrickx, A. G. *J. Nutr.* **1995**, *125*, S2263.
(171) Sawashita, J.; Takeda, A.; Okada, S. *Dev. Brain Res.* **1997**, *102*, 295.
(172) Takeda, A.; Minami, A.; Takefuta, S.; Tochigi, M.; Oku, N. *J. Neurosci. Res.* **2001**, *63*, 447.
(173) Hirate, M.; Takeda, A.; Tamano, H.; Enomoto, S.; Oku, N. *Epilepsy Res.* **2002**, *51*, 109.
(174) Takeda, A.; Hirate, M.; Tamano, H.; Oku, N. *Epilepsy Res.* **2003**, *54*, 123.
(175) Takeda, A.; Hirate, M.; Tamano, H.; Nisibaba, D.; Oku, N. *J. Neurochem.* **2003**, *85*, 1575.
(176) Takeda, A.; Hanajima, T.; Ijiro, H.; Ishige, A.; Iizuka, S.; Okada, S.; Oku, N. *Brain Res.* **1999**, *828*, 174.
(177) Takeda, A.; Hirate, M.; Oku, N. *Biometals* **2004**, *17*, 141.
(178) Benari, Y. *Neuroscience* **1985**, *14*, 375.
(179) McQuitty, J. T.; Dewys, W. D.; Monaco, L.; Strain, W. H.; Rob, C. G.; Apgar, J.; Pories, W. J. *Cancer Res.* **1970**, *30*, 1387.
(180) Minkel, D. T.; Dolhun, P. J.; Calhoun, B. L.; Saryan, L. A.; Petering, D. H. *Cancer Res.* **1979**, *39*, 2451.
(181) Saryan, L. A.; Minkel, D. T.; Dolhun, P. J.; Calhoun, B. L.; Wielgus, S.; Schaller, M.; Petering, D. H. *Cancer Res.* **1979**, *39*, 2457.
(182) Takeda, A.; Tamano, H.; Enomoto, S.; Oku, N. *Cancer Res.* **2001**, *61*, 5065.
(183) Takeda, A.; Tamano, H.; Oku, N. *Brain Res.* **2003**, *965*, 170.
(184) Takeda, A. *Brain Res. Rev.* **2003**, *41*, 79.
(185) Wedler, F. C.; Denman, R. B. *Curr. Top. Cell. Regul.* **1984**, *24*, 153.
(186) Takeda, A.; Sawashita, J.; Okada, S. *Neurosci. Lett.* **1998**, *242*, 45.
(187) Zheng, W. *Clin. Toxicol.* **2001**, *39*, 711.
(188) Takeda, A.; Ishiwatari, S.; Okada, S. *J. Neurosci. Res.* **1999**, *56*, 93.
(189) Aisen, P.; Aasa, R.; Redfield, A. G. *J. Biol. Chem.* **1969**, *244*, 4628.
(190) Aschner, M.; Vrana, K. E.; Zheng, W. *Neurotoxicology* **1999**, *20*, 173.
(191) Murphy, V. A.; Wadhwani, K. C.; Smith, Q. R.; Rapoport, S. I. *J. Neurochem.* **1991**, *57*, 948.
(192) Rabin, O.; Hegedus, L.; Bourre, J. M.; Smith, Q. R. *J. Neurochem.* **1993**, *61*, 509.
(193) Jefferies, W. A.; Brandon, M. R.; Hunt, S. V.; Williams, A. F.; Gatter, K. C.; Mason, D. Y. *Nature* **1984**, *312*, 162.
(194) Takeda, A.; Ishiwatari, S.; Okada, S. *J. Neurosci. Res.* **2000**, *59*, 542.
(195) Huggenvik, J. I.; Craven, C. M.; Idzerda, R. L.; Bernstein, S.; Kaplan, J.; McKnight, G. S. *Blood* **1989**, *74*, 482.
(196) Malecki, E. A.; Cook, B. M.; Devenyi, A. G.; Beard, J. L.; Connor, J. R. *J. Neurol. Sci.* **1999**, *170*, 112.
(197) Connor, J. R.; Menzies, S. L. *Glia* **1996**, *17*, 83.
(198) Bradbury, M. W. B. *J. Neurochem.* **1997**, *69*, 443.
(199) Takeda, A. *J. Health Sci.* **2001**, *47*, 520.
(200) Aldred, A. R.; Dickson, P. W.; Marley, P. D.; Schreiber, G. *J. Biol. Chem.* **1987**, *262*, 5293.
(201) Craven, C. M.; Alexander, J.; Eldridge, M.; Kushner, J. P.; Bernstein, S.; Kaplan, J. *Proc. Natl. Acad. Sci. U.S.A.* **1987**, *84*, 3457.
(202) Takeda, A.; Takatsuka, K.; Sotogaku, N.; Oku, N. *Neurochem. Int.* **2002**, *41*, 223.
(203) Nielsen, J. E.; Jensen, L. N.; Krabbe, K. *J. Neurol. Neurosurg. Psychiatry* **1995**, *59*, 318.
(204) Takeda, A.; Takatsuka, K.; Connor, J. R.; Oku, N. *Brain Res.* **2001**, *912*, 154.

(205) Loeffler, D. A.; Connor, J. R.; Juneau, P. L.; Snyder, B. S.; Kanaley, L.; Demaggio, A. J.; Nguyen, H.; Brickman, C. M.; Lewitt, P. A. *J. Neurochem.* **1995**, *65*, 710.
(206) Ilbäck, N. G.; Fohlman, J.; Friman, G. *Toxicol. Appl. Pharmacol.* **1992**, *114*, 166.
(207) Ilbäck, N. G.; Fohlman, J.; Friman, G.; Glynn, A. W. *Toxicology* **1992**, *71*, 193.
(208) Denardo, G. L.; Kroger, L. A.; Denardo, S. J.; Miers, L. A.; Salako, Q.; Kukis, D. L.; Fand, I.; Shen, S.; Renn, O.; Meares, C. F. *Cancer* **1994**, *73*, 1012.
(209) Kraeber-Bodere, F.; Mishra, A.; Thedrez, P.; FaivreChauvet, A.; Bardies, M.; Imai, S.; LeBoterff, J.; Chatal, J. F. *Eur. J. Nucl. Med.* **1996**, *23*, 560.
(210) McQuade, P.; Rowland, D. J.; Lewis, J. S.; Welch, M. J. *Curr. Med. Chem.* **2005**, *12*, 807.
(211) Miller, P. W.; Long, N. J.; Vilar, R.; Gee, A. D. *Angew. Chem., Int. Ed.* **2008**, *47*, 8998.
(212) Anderson, C. J.; Welch, M. J. *Chem. Rev.* **1999**, *99*, 2219.
(213) Melendez, E. *Crit. Rev. Oncol. Hematol.* **2002**, *42*, 309.
(214) Tinoco, A. D.; Valentine, A. M. *J. Am. Chem. Soc.* **2005**, *127*, 11218.
(215) Vavere, A. L.; Jones, L. A.; McCarthy, T. J.; Rowland, D. J.; Welch, M. *J. Labelled Compd. Radiopharm.* **2001**, *44*, S793.
(216) Vavere, A. L.; Welch, M. J. *J. Nucl. Med.* **2005**, *46*, 683.
(217) Wadas, T. J.; Wong, E. H.; Weisman, G. R.; Anderson, C. J. *Curr. Pharm. Des.* **2007**, *13*, 3.
(218) Berezin, M. Y.; Guo, K.; Teng, B.; Edwards, W. B.; Anderson, C. J.; Vasalatiy, O.; Gandjbakhche, A.; Griffiths, G. L.; Achilefu, S. *J. Am. Chem. Soc.* **2009**, *131*, 9198.
(219) Lovqvist, A.; Humm, J. L.; Sheikh, A.; Finn, R. D.; Koziorowski, J.; Ruan, S.; Pentlow, K. S.; Jungbluth, A.; Welt, S.; Lee, F. T.; Brechbiel, M. W.; Larson, S. M. *J. Nucl. Med.* **2001**, *42*, 1281.
(220) Herzog, H.; Rösch, F.; Stocklin, G.; Lueders, C.; Qaim, S. M.; Feinendegen, L. E. *J. Nucl. Med.* **1993**, *34*, 2222.
(221) Rösch, F.; Herzog, H.; Stolz, B.; Brockmann, J.; Kohle, M.; Muhlensiepen, H.; Marbach, P.; Muller-Gartner, H. W. *Eur. J. Nucl. Med.* **1999**, *26*, 358.
(222) Rösch, F.; Herzog, H.; Plag, C.; Neumaier, B.; Braun, U.; Muller-Gartner, H. W.; Stocklin, G. *Eur. J. Nucl. Med.* **1996**, *23*, 958.
(223) Garmestani, K.; Milenic, D. E.; Plascjak, P. S.; Brechbiel, M. W. *Nucl. Med. Biol.* **2002**, *29*, 599.
(224) Jamar, F.; Barone, R.; Mathieu, I.; Walrand, S.; Labar, D.; Carlier, P.; de Camps, J.; Schran, H.; Chen, T.; Smith, M. C.; Bouterfa, H.; Valkema, R.; Krenning, E. P.; Kvols, L. K.; Pauwels, S. *Eur. J. Nucl. Med. Mol. Imaging* **2003**, *30*, 510.
(225) Caravan, P.; Ellison, J. J.; McMurry, T. J.; Lauffer, R. B. *Chem. Rev.* **1999**, *99*, 2293.
(226) Li, W. H.; Fraser, S. E.; Meade, T. J. *J. Am. Chem. Soc.* **1999**, *121*, 1413.
(227) Dhingra, K.; Fouskova, P.; Angelovski, G.; Maier, M. E.; Logothetis, N. K.; Toth, E. *J. Biol. Inorg. Chem.* **2008**, *13*, 35.
(228) Angelovski, G.; Fouskova, P.; Mamedov, I.; Canals, S.; Toth, E.; Logothetis, N. K. *ChemBioChem* **2008**, *9*, 1729.
(229) Mishra, A.; Fousková, P.; Angelovski, G.; Balogh, E.; Mishra, A. K.; Logothetis, N. K.; Tóth, E. *Inorg. Chem.* **2008**, *47*, 1370.
(230) Hifumi, H.; Tanimoto, A.; Citterio, D.; Komatsu, H.; Suzuki, K. *Analyst* **2007**, *132*, 1153.
(231) Hanaoka, K.; Kikuchi, K.; Urano, Y.; Nagano, T. *J. Chem. Soc., Perkin Trans. 2* **2001**, 1840.
(232) Hanaoka, K.; Kikuchi, K.; Urano, Y.; Narazaki, M.; Yokawa, T.; Sakamoto, S.; Yamaguchi, K.; Nagano, T. *Chem. Biol.* **2002**, *9*, 1027.
(233) Major, J. L.; Boiteau, R. M.; Meade, T. J. *Inorg. Chem.* **2008**, *47*, 10788.
(234) Major, J. L.; Parigi, G.; Luchinat, C.; Meade, T. J. *Proc. Natl. Acad. Sci. U.S.A.* **2007**, *104*, 13881.
(235) Zhang, X.-A.; Lovejoy, K. S.; Jasanoff, A.; Lippard, S. J. *Proc. Natl. Acad. Sci. U.S.A.* **2007**, *104*, 10780.
(236) Trokowski, R.; Ren, J. M.; Kalman, F. K.; Sherry, A. D. *Angew. Chem., Int. Ed.* **2005**, *44*, 6920.
(237) Que, E. L.; Chang, C. J. *J. Am. Chem. Soc.* **2006**, *128*, 15942.
(238) Que, E. L.; Gianolio, E.; Baker, S. L.; Wong, A. P.; Aime, S.; Chang, C. J. *J. Am. Chem. Soc.* **2009**, *131*, 8527.
(239) Ralle, M.; Lutsenko, S. *Biometals* **2009**, *22*, 197.
(240) Fahrni, C. J. *Curr. Opin. Chem. Biol.* **2007**, *11*, 121.
(241) Paunesku, T.; Vogt, S.; Maser, J.; Lai, B.; Woloschak, G. *J. Cell. Biochem.* **2006**, *99*, 1489.
(242) Ortega, R.; Devès, G.; Carmona, A. *J. R. Soc. Interface* **2009**, *6*, S649.
(243) Garratt-Reed, A. J.; Bell, D. C. *Energy-Dispersive X-ray Analysis in the Electron Microscope*; Garland Science: London, 2003.
(244) Roomans, G. M.; vonEuler, A. *Cell Biol. Int.* **1996**, *20*, 103.
(245) Zierold, K. *J. Trace Microprobe Tech.* **2002**, *20*, 181.
(246) Roomans, G. M. *J. Electron Microsc. Technol.* **1988**, *9*, 3.
(247) Veríssimo, A.; Alves, L. C.; Filipe, P.; Silva, J. N.; Silva, R.; Ynsa, M. D.; Gontier, E.; Moretto, P.; Pallon, J.; Pinheiro, T. *Microsc. Res. Technol.* **2007**, *70*, 302.
(248) Bertrand, M.; Weber, G.; Schoefs, B. *TRAC-Trends Anal. Chem.* **2003**, *22*, 254.
(249) Watt, F. *Nucl. Instrum. Methods Phys. Res., Sect. B* **1997**, *130*, 1.
(250) Themner, K.; Malmqvist, K. G. *Nucl. Instrum. Methods Phys. Res., Sect. B* **1986**, *15*, 404.
(251) Carmona, A.; Deves, G.; Ortega, R. *Anal. Bioanal. Chem.* **2008**, *390*, 1585.
(252) Lechner, P.; Fiorini, C.; Hartmann, R.; Kemmer, J.; Krause, N.; Leutenegger, P.; Longoni, A.; Soltau, H.; Stotter, D.; Stotter, R.; Struder, L.; Weber, U. *Nucl. Instrum. Methods Phys. Res., Sect. A* **2001**, *458*, 281.
(253) Carvalho, M. L.; Magalhaes, T.; Becker, M.; von Bohlen, A. *Spectrosc. Acta B* **2007**, *62*, 1004.
(254) Reinert, T.; Spemann, D.; Morawski, M.; Arendt, T. *Nucl. Instrum. Methods Phys. Res., Sect. B* **2006**, *249*, 734.
(255) Watt, F.; van Kan, J. A.; Rajta, I.; Bettiol, A. A.; Choo, T. F.; Breese, M. B. H.; Osipowicz, T. *Nucl. Instrum. Methods Phys. Res., Sect. B* **2003**, *210*, 14.
(256) Llabador, Y.; Moretto, P. *Applications of Nuclear Microprobes in the Life Sciences: An Efficient Analytical Technique for Research in Biology and Medicine*; World Scientific Publishing Company: Singapore, 1998.
(257) Matsuyama, S.; Mimura, H.; Katagishi, K.; Yumoto, H.; Handa, S.; Fujii, M.; Sano, Y.; Shimura, M.; Yabashi, M.; Nishino, Y.; Tamasaku, K.; Ishikawa, T.; Yamauchi, K. *Surf. Interface Anal.* **2008**, *40*, 1042.
(258) Ortega, R.; Bohic, S.; Tucoulou, R.; Somogyi, A.; Deves, G. *Anal. Chem.* **2004**, *76*, 309.
(259) Matsuyama, S.; Mimura, H.; Yumoto, H.; Sano, Y.; Yamamura, K.; Yabashi, M.; Nishino, Y.; Tamasaku, K.; Ishikawa, T.; Yamauchi, K. *Rev. Sci. Instrum.* **2006**, *77*, 103102.
(260) Snigirev, A.; Kohn, V.; Snigireva, I.; Lengeler, B. *Nature* **1996**, *384*, 49.
(261) Snigirev, A.; Snigireva, I. *C. R. Phys.* **2008**, *9*, 507.
(262) Schroer, C. G.; Kuhlmann, M.; Hunger, U. T.; Gunzler, T. F.; Kurapova, O.; Feste, S.; Frehse, F.; Lengeler, B.; Drakopoulos, M.; Somogyi, A.; Simionovici, A. S.; Snigirev, A.; Snigireva, I.; Schug, C.; Schroder, W. H. *Appl. Phys. Lett.* **2003**, *82*, 1485.
(263) Di Fabrizio, E.; Romanato, F.; Gentili, M.; Cabrini, S.; Kaulich, B.; Susini, J.; Barrett, R. *Nature* **1999**, *401*, 895.
(264) Twining, B. S.; Baines, S. B.; Fisher, N. S.; Maser, J.; Vogt, S.; Jacobsen, C.; Tovar-Sanchez, A.; Sanudo-Wilhelmy, S. A. *Anal. Chem.* **2003**, *75*, 3806.
(265) McRae, R.; Lai, B.; Vogt, S.; Fahrni, C. J. *J. Struct. Biol.* **2006**, *155*, 22.
(266) Von Euler, A.; Wroblewski, R.; Roomans, G. M. *Scanning Microsc.* **1992**, *6*, 451.
(267) Roomans, G. M.; Voneuler, A.; Mork, A. C.; Palsgard, E.; Vonsteyern, C. V. *Eur. J. Morphol.* **1993**, *31*, 21.
(268) Kirz, J.; Jacobsen, C.; Howells, M. *Q. Rev. Biophys.* **1995**, *28*, 33.
(269) Neumann, A.; Reske, T.; Held, M.; Jahnke, K.; Ragoss, C.; Maier, H. R. *J. Mater. Sci., Mater. Med.* **2004**, *15*, 1135.
(270) Penner-Hahn, J. E. *Coord. Chem. Rev.* **2005**, *249*, 161.
(271) Bacquart, T.; Deves, G.; Carmona, A.; Tucoulou, R.; Bohic, S.; Ortega, R. *Anal. Chem.* **2007**, *79*, 7353.
(272) Valko, M.; Morris, H.; Cronin, M. T. D. *Curr. Med. Chem.* **2005**, *12*, 1161.
(273) Bergers, G.; Benjamin, L. E. *Nat. Rev. Cancer* **2003**, *3*, 401.
(274) Finney, L.; Vogt, S.; Fukai, T.; Glesne, D. *Clin. Exp. Pharmacol. Physiol.* **2009**, *36*, 88.
(275) Finney, L.; Mandava, S.; Ursos, L.; Zhang, W.; Rodi, D.; Vogt, S.; Legnini, D.; Maser, J.; Ikpatt, F.; Olopade, O. I.; Glesne, D. *Proc. Natl. Acad. Sci. U.S.A.* **2007**, *104*, 2247.
(276) Weigelt, B.; Peterse, J. L.; van 't Veer, L. J. *Nat. Rev. Cancer* **2005**, *5*, 591.
(277) Farquharson, M. J.; Geraki, K. *X-Ray Spectrom.* **2004**, *33*, 240.
(278) Farquharson, M. J.; Geraki, K.; Falkenberg, G.; Leek, R.; Harris, A. *Appl. Radiat. Isot.* **2007**, *65*, 183.
(279) Farquharson, M. J.; Al-Ebraheem, A.; Falkenberg, G.; Leek, R.; Harris, A. L.; Bradley, D. A. *Phys. Med. Biol.* **2008**, *53*, 3023.
(280) Geraki, K.; Farquharson, M. J.; Bradley, D. A. *Phys. Med. Biol.* **2002**, *47*, 2327.
(281) Geraki, K.; Farquharson, M. J.; Bradley, D. A.; Gundogdu, O.; Falkenberg, G. *X-Ray Spectrom.* **2008**, *37*, 12.
(282) Pereira, G. R.; Rocha, H. S.; Anjos, M. J.; Farias, P. C. M. A.; Pérez, C. A.; Lopes, R. T. *Eur. J. Radiol.* **2008**, *68*, S104.
(283) Pereira, G. R.; Anjos, M. J.; Rocha, H. S.; Faria, P.; Perez, C. A.; Lopes, R. T. *Nucl. Instrum. Methods Phys. Res., Sect. A* **2007**, *580*, 951.

(284) Pereira, G. R.; Rocha, H. S.; Anjos, M. J.; Faria, P.; Perez, C. A.; Lopes, R. T. *Nucl. Instrum. Methods Phys. Res., Sect. A* **2007**, *581*, 128.
(285) Rocha, H. S.; Pereira, G. R.; Anjos, M. J.; Faria, P.; Kellermann, G.; Perez, C. A.; Tirao, G.; Mazzaro, I.; Giles, C.; Lopes, R. T. *X-Ray Spectrom.* **2007**, *36*, 247.
(286) Moul, J. W.; Mouraviev, V.; Sun, L.; Schroeck, F. R.; Polascik, T. J. *Curr. Opin. Urol.* **2009**, *19*, 154.
(287) Thomas, J. A. *Nutr. Rev.* **1999**, *57*, 95.
(288) Costello, L. C.; Franklin, R. B. *Mol. Cancer* **2006**, *5*, 17.
(289) Ide-Ektessabi, A.; Fujisawa, S.; Sugimura, K.; Kitamura, Y.; Gotoh, A. *X-Ray Spectrom.* **2002**, *31*, 7.
(290) Bruijnincx, P. C. A.; Sadler, P. J. *Curr. Opin. Chem. Biol.* **2008**, *12*, 197.
(291) Hall, M. D.; Mellor, H. R.; Callaghan, R.; Hambley, T. W. *J. Med. Chem.* **2007**, *50*, 3403.
(292) Sakurai, H.; Okamoto, M.; Hasegawa, M.; Satoh, T.; Oikawa, M.; Kamiya, T.; Arakawa, K.; Nakano, T. *Cancer Sci.* **2008**, *99*, 901.
(293) Ortega, R.; Moretto, P.; Fajac, A.; Benard, J.; Llabador, Y.; Simonoff, M. *Cell. Mol. Biol.* **1996**, *42*, 77.
(294) Corde, S.; Biston, M. C.; Elleaume, H.; Esteve, F.; Charvet, A. M.; Joubert, A.; Ducros, V.; Bohic, S.; Simionovici, A.; Brochard, T.; Nemoz, C.; Renier, M.; Tropres, I.; Fiedler, S.; Bravin, A.; Thomlinson, W.; Le Bas, J. F.; Balosso, J. *Radiat. Res.* **2002**, *158*, 763.
(295) Hall, M. D.; Dillon, C. T.; Zhang, M.; Beale, P.; Cai, Z. H.; Lai, B.; Stampfl, A. P. J.; Hambley, T. W. *J. Biol. Inorg. Chem.* **2003**, *8*, 726.
(296) Hall, M. D.; Alderden, R. A.; Zhang, M.; Beale, P. J.; Cai, Z. H.; Lai, B.; Stampfl, A. P. J.; Hambley, T. W. *J. Struct. Biol.* **2006**, *155*, 38.
(297) Hall, M. D.; Foran, G. J.; Zhang, M.; Beale, P. J.; Hambley, T. W. *J. Am. Chem. Soc.* **2003**, *125*, 7524.
(298) Ilinski, P.; Lai, B.; Cai, Z.; Yun, W.; Legnini, D.; Talarico, T.; Cholewa, M.; Webster, L. K.; Deacon, G. B.; Rainone, S.; Phillips, D. R.; Stampfl, A. P. J. *Cancer Res.* **2003**, *63*, 1776.
(299) Chen, K. G.; Valencia, J. C.; Lai, B.; Zhang, G. F.; Paterson, J. K.; Rouzaud, F.; Berens, W.; Wincovitch, S. M.; Garfield, S. H.; Leapman, R. D.; Hearing, V. J.; Gottesman, M. M. *Proc. Natl. Acad. Sci. U.S.A.* **2006**, *103*, 9903.
(300) Alderden, R. A.; Mellor, H. R.; Modok, S.; Hall, M. D.; Sutton, S. R.; Newville, M. G.; Callaghan, R.; Hambley, T. W. *J. Am. Chem. Soc.* **2007**, *129*, 13400.
(301) Ott, I.; Gust, R. *Arch. Pharm.* **2007**, *340*, 117.
(302) Waern, J. B.; Harris, H. H.; Lai, B.; Cai, Z. H.; Harding, M. M.; Dillon, C. T. *J. Biol. Inorg. Chem.* **2005**, *10*, 443.
(303) Hall, M. D.; Failes, T. W.; Yamamoto, N.; Hambley, T. W. *Dalton Trans.* **2007**, 3983.
(304) Ware, D. C.; Palmer, B. D.; Wilson, W. R.; Denny, W. A. *J. Med. Chem.* **1993**, *36*, 1839.
(305) Bonnitcha, P. D.; Hall, M. D.; Underwood, C. K.; Foran, G. J.; Zhang, M.; Beale, P. J.; Hambley, T. W. *J. Inorg. Biochem.* **2006**, *100*, 963.
(306) Hall, M. D.; Underwood, C. K.; Failes, T. W.; Foran, G. J.; Hambley, T. W. *Aust. J. Chem.* **2007**, *60*, 180.
(307) Carney, D. A. *Leuk. Lymphoma* **2008**, *49*, 1846.
(308) Nicolis, I.; Dacher, P.; Guyon, F.; Chevallier, P.; Curis, E.; Benazeth, S. *J. Trace Microprobe Technol.* **2002**, *20*, 565.
(309) Curis, E.; Nicolis, I.; Bohic, S.; Somogyi, A.; Simionovici, A.; Benazeth, S. *Phys. Scr.* **2005**, *T115*, 870.
(310) Munro, K. L.; Mariana, A.; Klavins, A. I.; Foster, A. J.; Lai, B.; Vogt, S.; Cai, Z.; Harris, H. H.; Dillon, C. T. *Chem. Res. Toxicol.* **2008**, *21*, 1760.
(311) Nieuwenhuys, R.; Voogd, J.; van Huijzen, C. *The Human Central Nervous System*; Springer: Berlin Heidelberg, 2007.
(312) Que, E. L.; Domaille, D. W.; Chang, C. J. *Chem. Rev.* **2008**, *108*, 1517.
(313) Burdette, S. C.; Lippard, S. J. *Proc. Natl. Acad. Sci. U.S.A.* **2003**, *100*, 3605.
(314) Zatta, P.; Lucchini, R.; van Rensburg, S. J.; Taylor, A. *Brain. Res. Bull.* **2003**, *62*, 15.
(315) Szczerbowska-Boruchowska, M.; Chwiej, J.; Lankosz, M.; Adamek, D.; Wojcik, S.; Krygowska-Wajs, A.; Tomik, B.; Bohic, S.; Susini, J.; Simionovici, A.; Dumas, P.; Kastyak, M. *X-Ray Spectrom.* **2005**, *34*, 514.
(316) Maenhaut, W.; Hebbrecht, G.; Dereuck, J. *Nucl. Instrum. Methods Phys. Res., Sect. B* **1993**, *75*, 180.
(317) Carmona, A.; Cloetens, P.; Deves, G.; Bohic, S.; Ortega, R. *J. Anal. At. Spectrom.* **2008**, *23*, 1083.
(318) Ortega, R.; Cloetens, P.; Devès, G.; Carmona, A.; Bohic, S. *PLoS ONE* **2007**, *2*, e925.
(319) Reinert, T.; Morawski, M.; Arendt, T.; Butz, T. *Nucl. Instrum. Methods Phys. Res., Sect. B* **2003**, *210*, 395.
(320) Fiedler, A.; Reinert, T.; Morawski, M.; Brückner, G.; Arendt, T.; Butz, T. *Nucl. Instrum. Methods Phys. Res., Sect. B* **2007**, *260*, 153.
(321) Morawski, M.; Reinert, T.; Bruckner, G.; Wagner, F. E.; Arendt, T.; Troger, W. *Hyperfine Interact.* **2004**, *159*, 285.
(322) Bohic, S.; Murphy, K.; Paulus, W.; Cloetens, P.; Salome, M.; Susini, J.; Double, K. *Anal. Chem.* **2008**, *80*, 9557.
(323) MacDonald, B. K.; Cockerell, O. C.; Sander, J. W.; Shorvon, S. D. *Brain* **2000**, *123* (Part 4), 665.
(324) Lotharius, J.; Brundin, P. *Nat. Rev. Neurosci.* **2002**, *3*, 932.
(325) Dick, F. D.; De Palma, G.; Ahmadi, A.; Scott, N. W.; Prescott, G. J.; Bennett, J.; Semple, S.; Dick, S.; Counsell, C.; Mozzoni, P.; Haites, N.; Wettinger, S. B.; Mutti, A.; Otelea, M.; Seaton, A.; Söderkvist, P.; Felice, A. *Occup. Environ. Med.* **2007**, *64*, 666.
(326) Dexter, D. T.; Wells, F. R.; Agid, F.; Agid, Y.; Lees, A. J.; Jenner, P.; Marsden, C. D. *Lancet* **1987**, *2*, 1219.
(327) Dexter, D. T.; Carayon, A.; Javoy-Agid, F.; Agid, Y.; Wells, F. R.; Daniel, S. E.; Lees, A. J.; Jenner, P.; Marsden, C. D. *Brain* **1991**, *114*, 1953.
(328) Ren, M. Q.; Xie, J. P.; Wang, X. S.; Ong, W. Y.; Leong, S. K.; Watt, F. *Nucl. Instrum. Methods Phys. Res., Sect. B* **2001**, *181*, 522.
(329) Morawski, M.; Reinert, T.; Meinecke, C.; Arendt, T.; Butz, T. *Nucl. Instrum. Methods Phys. Res., Sect. B* **2005**, *231*, 229.
(330) Popescu, B. F.; George, M. J.; Bergmann, U.; Garachtchenko, A. V.; Kelly, M. E.; McCrea, R. P. E.; Lüning, K.; Devon, R. M.; George, G. N.; Hanson, A. D.; Harder, S. M.; Chapman, L. D.; Pickering, I. J.; Nichol, H. *Phys. Med. Biol.* **2009**, *54*, 651.
(331) Morawski, M.; Meinecke, C.; Reinert, T.; Dörffel, A. C.; Riederer, P.; Arendt, T.; Butz, T. *Nucl. Instrum. Methods Phys. Res., Sect. B* **2005**, *231*, 224.
(332) Smith, S. R.; Cooperman, S.; Lavaute, T.; Tresser, N.; Ghosh, M.; Meyron-Holtz, E.; Land, W.; Ollivierre, H.; Jortner, B.; Switzer, R.; Messing, A.; Rouault, T. A. *Ann. N.Y. Acad. Sci.* **2004**, *1012*, 65.
(333) Zhang, P. J.; Land, W.; Lee, S.; Juliani, J.; Lefman, J.; Smith, S. R.; Germain, D.; Kessel, M.; Leapman, R.; Rouault, T. A.; Subramaniam, S. *J. Struct. Biol.* **2005**, *150*, 144.
(334) Ide-Ektessabi, A.; Kawakami, T.; Watt, F. *Nucl. Instrum. Methods Phys. Res., Sect. B* **2004**, *213*, 590.
(335) Yoshida, S.; Ide-Ektessabi, A.; Fujisawa, S. *Struct. Chem.* **2003**, *14*, 85.
(336) Reinert, T.; Fiedler, A.; Morawski, M.; Arendt, T. *Nucl. Instrum. Methods Phys. Res., Sect. B* **2007**, *260*, 227.
(337) Szczerbowska-Boruchowska, M.; Lankosz, M.; Ostachowicz, J.; Adamek, D.; Krygowska-Wajs, A.; Tomik, B.; Szczudlik, A.; Simionovici, A.; Bohic, S. *X-Ray Spectrom.* **2004**, *33*, 3.
(338) Szczerbowska-Boruchowska, M. *X-Ray Spectrom.* **2008**, *37*, 21.
(339) Chwiej, J.; Fik-Mazgaj, K.; Szczerbowska-Boruchowska, M.; Lankosz, M.; Ostachowicz, J.; Adamek, D.; Simionovici, A.; Bohic, S. *Anal. Chem.* **2005**, *77*, 2895.
(340) Chwiej, J.; Adamek, D.; Szczerbowska-Boruchowska, M.; Krygowska-Wajs, A.; Bohic, S.; Lankosz, M. *J. Trace Elem. Med. Biol.* **2008**, *22*, 183.
(341) Ferri, C. P.; Prince, M.; Brayne, C.; Brodaty, H.; Fratiglioni, L.; Ganguli, M.; Hall, K.; Hasegawa, K.; Hendrie, H.; Huang, Y.; Jorm, A.; Mathers, C.; Menezes, P. R.; Rimmer, E.; Scazufca, M. *Lancet* **2005**, *366*, 2112.
(342) Hardy, J.; Selkoe, D. J. *Science* **2002**, *297*, 353.
(343) Bush, A. I. *Trends Neurosci.* **2003**, *26*, 207.
(344) Liu, G. J.; Huang, W. D.; Moir, R. D.; Vanderburg, C. R.; Lai, B.; Peng, Z. C.; Tanzi, R. E.; Rogers, J. T.; Huang, X. D. *J. Struct. Biol.* **2006**, *155*, 45.
(345) Samudralwar, D. L.; Diprete, C. C.; Ni, B. F.; Ehmann, W. D.; Markesbery, W. R. *J. Neurol. Sci.* **1995**, *130*, 139.
(346) Deibel, M. A.; Ehmann, W. D.; Markesbery, W. R. *J. Neurol. Sci.* **1996**, *143*, 137.
(347) Ide-Ektessabi, A. *Application of Synchrotron Radiation*; Springer: Berlin Heidelberg, 2007.
(348) Lovell, M. A.; Robertson, J. D.; Teesdale, W. J.; Campbell, J. L.; Markesbery, W. R. *J. Neurol. Sci.* **1998**, *158*, 47.
(349) Rajendran, R.; Ren, M. Q.; Ynsa, M. D.; Casadesus, G.; Smith, M. A.; Perry, G.; Halliwell, B.; Watt, F. *Biochem. Biophys. Res. Commun.* **2009**, *382*, 91.
(350) Ishihara, R.; Ide-Ektessabi, A.; Ikeda, K.; Mizuno, Y.; Fujisawa, S.; Takeuchi, T.; Ohta, T. *Neuroreport* **2002**, *13*, 1817.
(351) Miller, L. M.; Smith, R. J.; Ruppel, M. E.; Ott, C. H.; Lanzirotti, A. *Rev. Sci. Instrum.* **2005**, *76*, 066107.
(352) Miller, L. M.; Wang, Q.; Telivala, T. P.; Smith, R. J.; Lanzirotti, A.; Miklossy, J. *J. Struct. Biol.* **2006**, *155*, 30.
(353) Byler, D. M.; Susi, H. *Biopolymers* **1986**, *25*, 469.
(354) McCrea, R. P. E.; Harder, S. L.; Martin, M.; Buist, R.; Nichol, H. *Eur. J. Radiol.* **2008**, *68S*, 109.
(355) Collingwood, J. F.; Chong, R. K. K.; Kasama, T.; Cervera-Gontard, L.; Dunin-Borkowski, R. E.; Perry, G.; Posfai, M.; Siedlak, S. L.; Simpson, E. T.; Smith, M. A.; Dobson, J. *J. Alzheimers Dis.* **2008**, *14*, 235.
(356) Wijesekera, L. C.; Leigh, P. N. *Orphanet J. Rare Dis.* **2009**, *4*, 3.

(357) Carrí, M. T.; Ferri, A.; Cozzolino, M.; Calabrese, L.; Rotilio, G. *Brain Res. Bull.* **2003**, *61*, 365.
(358) Chwiej, J.; Szczerbowska-Boruchowska, M.; Wojcik, S.; Lankosz, M.; Chlebda, M.; Adamek, D.; Tomik, B.; Setkowicz, Z.; Falkenberg, G.; Stegowski, Z.; Szczudlik, A. *J. Alloys Compd.* **2005**, *401*, 184.
(359) Szczerbowska-Boruchowska, M.; Lankosz, M.; Ostachowicz, J.; Adamek, D.; Krygowska-Wajs, A.; Tomik, B.; Szczudlik, A.; Simionovici, A.; Bohic, S. *J. Phys. IV* **2003**, *104*, 325.
(360) Tomik, B.; Chwiej, J.; Szczerbowska-Boruchowska, M.; Lankosz, M.; Wojcik, S.; Adamek, D.; Falkenberg, G.; Bohic, S.; Simionovici, A.; Stegowski, Z.; Szczudlik, A. *Neurochem. Res.* **2006**, *31*, 321.
(361) de Bie, P.; Muller, P.; Wijmenga, C.; Klomp, L. W. J. *J. Med. Genet.* **2007**, *44*, 673.
(362) Stohs, S. J.; Bagchi, D. *Free Radical Biol. Med.* **1995**, *18*, 321.
(363) Suzuki, M.; Gitlin, J. D. *Pediatr. Int.* **1999**, *41*, 436.
(364) Kirby, B. J.; Danks, D. M.; Legge, G. J.; Mercer, J. F. *J. Inorg. Biochem.* **1998**, *71*, 189.
(365) Brewer, G. J.; Dick, R. D.; Yuzbasiyan-Gurkin, V.; Tankanow, R.; Young, A. B.; Kluin, K. J. *Arch. Neurol.* **1991**, *48*, 42.
(366) Wiggelinkhuizen, M.; Tilanus, M. E. C.; Bollen, C. W.; Houwen, R. H. J. *Aliment. Pharmacol. Ther.* **2009**, *29*, 947.
(367) Zhang, L.; Lichtmannegger, J.; Summer, K. H.; Webb, S.; Pickering, I. J.; George, G. N. *Biochemistry* **2009**, *48*, 891.
(368) Sergeant, C.; Gouget, B.; Llabador, Y.; Simonoff, M.; Yefimova, M.; Courtois, Y.; Jeanny, J. C. *Nucl. Instrum. Methods Phys. Res., Sect. B* **1999**, *158*, 344.
(369) Sergeant, C.; Llabador, Y.; Deves, G.; Vesvres, M. H.; Simonoff, M.; Yefimova, M.; Courtois, Y.; Jeanny, J. C. *Nucl. Instrum. Methods Phys. Res., Sect. B* **2001**, *181*, 533.
(370) Yefimova, M. G.; Jeanny, J. C.; Guillonneau, X.; Keller, N.; Nguyen-Legros, J.; Sergeant, C.; Guillou, F.; Courtois, Y. *Invest. Ophthalmol. Vis. Sci.* **2000**, *41*, 2343.
(371) Stocker, R.; Keaney, J. F. *Physiol. Rev.* **2004**, *84*, 1381.
(372) Stadler, N.; Lindner, R. A.; Davies, M. J. *Arterioscler. Thromb. Vasc. Biol.* **2004**, *24*, 949.
(373) Stadler, N.; Stanley, N.; Heeneman, S.; Vacata, V.; Daemen, M.; Bannon, P. G.; Waltenberger, J.; Davies, M. J. *Arterioscler. Thromb. Vasc. Biol.* **2008**, *28*, 1024.
(374) Danesh, J.; Appleby, P. *Circulation* **1999**, *99*, 852.
(375) Horwitz, L. D.; Rosenthal, E. A. *Vasc. Med.* **1999**, *4*, 93.
(376) de Valk, B.; Marx, J. J. *Arch. Intern. Med.* **1999**, *159*, 1542.
(377) Roijers, R. B.; Dutta, R. K.; Cleutjens, J. P. M.; Mutsaers, P. H. A.; De Goeij, J. J. M.; Van der Vusse, G. *J. Anal. Chem.* **2008**, *80*, 55.
(378) Roijers, R. B.; Dutta, R. K.; Mutsaers, P. H. A.; Gijbels, M. J. J.; de Winther, M. P. J.; de Goeij, J. J. M.; van der Vusse, G. J. *Nucl. Instrum. Methods Phys. Res., Sect. B* **2005**, *231*, 239.
(379) Rajendran, R.; Ren, M.; Ning, P.; Huat, B. T. K.; Halliwell, B.; Watt, F. *Nucl. Instrum. Methods Phys. Res., Sect. B* **2007**, *260*, 136.
(380) Hennig, B.; Toborek, M.; McClain, C. J. *Nutrition* **1996**, *12*, 711.
(381) Hennig, B.; Meerarani, P.; Toborek, M.; McClain, C. J. *J. Am. Coll. Nutr.* **1999**, *18*, 152.
(382) Watt, F.; Grime, G. W.; Brook, A. J.; Gadd, G. M.; Perry, C. C.; Pearce, R. B.; Turnau, K.; Watkinson, S. C. *Nucl. Instrum. Methods Phys. Res., Sect. B* **1991**, *54*, 123.
(383) Minqin, R.; Watt, F.; Huat, B. T. K.; Halliwell, B. *Free Radical Biol. Med.* **2003**, *34*, 746.
(384) Gajda, M.; Banas, K.; Banas, A.; Jawien, J.; Mateuszuk, L.; Chlopicki, S.; Kwiatek, W. M.; Cichockil, T.; Falkenberg, G. *X-Ray Spectrom.* **2008**, *37*, 495.
(385) Jawień, J.; Nastałek, P.; Korbut, R. *J. Physiol. Pharmacol.* **2004**, *55*, 503.
(386) Minqin, R.; En, H.; Beck, K.; Rajendran, R.; Wu, B. J.; Halliwell, B.; Watt, F.; Stocker, R. *Nucl. Instrum. Methods Phys. Res., Sect. B* **2007**, *260*, 240.
(387) Wu, B. J.; Kathir, K.; Witting, P. K.; Beck, K.; Choy, K.; Li, C.; Croft, K. D.; Mori, T. A.; Tanous, D.; Adams, M. R.; Lau, A. K.; Stocker, R. *J. Exp. Med.* **2006**, *203*, 1117.
(388) Simionescu, M.; Antohe, F. *Handbook Exp. Pharmacol.* **2006**, 41.
(389) Sima, A. V.; Stancu, C. S.; Simionescu, M. *Cell Tissue Res.* **2009**, *335*, 191.
(390) Witting, P. K.; Harris, H. H.; Rayner, B. S.; Aitken, J. B.; Dillon, C. T.; Stocker, R.; Lai, B.; Cai, Z. H.; Lay, P. A. *Biochemistry* **2006**, *45*, 12500.
(391) Tayebjee, M. H.; Lip, G. Y. H.; MacFadyen, R. J. *Curr. Med. Chem.* **2005**, *12*, 917.
(392) Altekin, E.; Coker, C.; Sisman, A. R.; Onvural, B.; Kuralay, F.; Kirimh, O. *J. Trace Elem. Med. Biol.* **2005**, *18*, 235.
(393) Carbonell, T.; Rama, R. *Curr. Med. Chem.* **2007**, *14*, 857.
(394) Evans, P. J.; Smith, C.; Mitchinson, M. J.; Halliwell, B. *Free Radical Res.* **1995**, *23*, 465.
(395) Konoha, K.; Sadakane, Y.; Kawahara, M. *J. Health Sci.* **2006**, *52*, 1.
(396) Sun, Y. J.; Jin, K. L.; Mao, X. O.; Zhu, Y. H.; Greenberg, D. A. *Proc. Natl. Acad. Sci. U.S.A.* **2001**, *98*, 15306.
(397) Duong, T. T. H.; Witting, P. K.; Antao, S. T.; Parry, S. N.; Kennerson, M.; Lai, B.; Vogt, S.; Lay, P. A.; Harris, H. H. *J. Neurochem.* **2009**, *108*, 1143.
(398) Hossmann, K. A. *Neuropharmacology* **2008**, *55*, 257.
(399) Fujioka, M.; Taoka, T.; Matsuo, Y.; Hiramatsu, K. I.; Kondo, Y.; Ogoshi, K.; Miyasaki, A.; Sakaki, T.; Kato, K.; Colony, A.; Siesjs, B. K. *Stroke* **2000**, *31*, P221.
(400) Fujioka, M.; Taoka, T.; Matsuo, Y.; Mishima, K.; Ogoshi, K.; Kondo, Y.; Tsuda, M.; Fujiwara, M.; Asano, T.; Sakaki, T.; Miyasaki, A.; Park, D.; Siesjo, B. K. *Ann. Neurol.* **2003**, *54*, 732.
(401) Wang, X.; Qian, J.; He, R.; Wei, L.; Liu, N.; Zhang, Z.; Huang, Y.; Lei, H. *Magn. Reson. Med.* **2006**, *56*, 474.
(402) Langheinrich, A. C.; Michniewicz, A.; Sedding, D. G.; Lai, B.; Jorgensen, S. M.; Bohle, R. M.; Ritman, E. L. *Invest. Radiol.* **2007**, *42*, 263.
(403) Andrews, N. C. *N. Engl. J. Med.* **1999**, *341*, 1986.
(404) Pietrangelo, A. *N. Engl. J. Med.* **2004**, *350*, 2383.
(405) Pietrangelo, A. *Biochim. Biophys. Acta* **2006**, *1763*, 700.
(406) Guinote, I.; Fleming, R.; Silva, R.; Filipe, P.; Silva, J. N.; Verissimo, A.; Napoleao, P.; Alves, L. C.; Pinheiro, T. *Nucl. Instrum. Methods Phys. Res., Sect. B* **2006**, *249*, 697.
(407) Fox, P. L. *Biometals* **2003**, *16*, 9.
(408) Osterode, W.; Falkenberg, G.; Hoeftberger, R.; Wrba, F. *Spectrochim. Acta B* **2007**, *62*, 682.
(409) Gilsanz, V. *Trends Endocrinol. Metab.* **1998**, *9*, 184.
(410) Yamaguchi, M. *Gen. Pharmacol.* **1995**, *26*, 1179.
(411) Blumer, M. J. F.; Longato, S.; Fritsch, H. *Ann. Anat.* **2008**, *190*, 305.
(412) Rubin, J.; Rubin, C.; Jacobs, C. R. *Gene* **2006**, *367*, 1.
(413) Bradley, D. A.; Moger, C. J.; Winlove, C. P. *Nucl. Instrum. Methods Phys. Res., Sect. A* **2007**, *580*, 473.
(414) Kaabar, W.; Daar, E.; Gundogdu, O.; Jenneson, P. M.; Farquharson, M. J.; Webb, M.; Jeynes, C.; Bradley, D. A. *Appl. Radiat. Isot.* **2009**, *67*, 475.
(415) Gallagher, J. C.; Nams; Ettinger, B.; Gass, M. L. S.; Kagan, R.; McClung, B. L.; McClung, M. R.; Simon, J. A. *Menopause: J. N. Am. Menopause Soc.* **2002**, *9*, 84.
(416) Kalu, D. N. *Bone Miner.* **1991**, *15*, 175.
(417) Lima, I.; Anjos, M. J.; Fleiuss, M. L. F.; Rosenthal, D.; Lopes, R. T. *X-Ray Spectrom.* **2008**, *37*, 249.
(418) Zhang, Y. X.; Cheng, F.; Li, D. Y.; Wang, Y. S.; Zhang, G. L.; Liao, W. S.; Tang, T. T.; Huang, Y. Y.; He, W. *Biol. Trace Elem. Res.* **2005**, *103*, 177.
(419) Lima, I.; Anjos, M. J.; Farias, M. L. F.; Pantaleão, T. U.; da Costa, V. M. C.; Lopes, R. T. *Eur. J. Radiol.* **2008**, *68*, S95.
(420) Selwitz, R. H.; Ismail, A. I.; Pitts, N. B. *Lancet* **2007**, *369*, 51.
(421) Anttila, A. *Arch. Oral Biol.* **1986**, *31*, 723.
(422) Brown, C. J.; Chenery, S. R. N.; Smith, B.; Tomkins, A.; Roberts, G. J.; Sserunjogi, L.; Thompson, M. *Analyst* **2002**, *127*, 319.
(423) Preoteasa, E. A.; Preoteasa, E.; Kuczumow, A.; Gurban, D.; Harangus, L.; Grambole, D.; Herrmann, F. *X-Ray Spectrom.* **2008**, *37*, 517.
(424) Harris, H. H.; Vogt, S.; Eastgate, H.; Lay, P. A. *J. Biol. Inorg. Chem.* **2008**, *13*, 303.
(425) Souza, A. P.; Gerlach, R. F.; Line, S. R. P. *Biomaterials* **2001**, *22*, 2025.
(426) Malara, P.; Kwapulinski, J.; Malara, B. *Sci. Total Environ.* **2006**, *369*, 59.
(427) McCormick, D. A.; Contreras, D. *Annu. Rev. Physiol.* **2001**, *63*, 815.
(428) Hamed, S. A.; Abdellah, M. M.; El-Melegy, N. *J. Pharmacol. Sci.* **2004**, *96*, 465.
(429) Chwiej, J.; Winiarski, W.; Ciarach, M.; Janeczko, K.; Lankosz, M.; Rickers, K.; Setkowicz, Z. *J. Biol. Inorg. Chem.* **2008**, *13*, 1267.
(430) Bossy-Wetzel, E.; Schwarzenbacher, R.; Lipton, S. A. *Nat. Med.* **2004**, *10*, 2.
(431) Radtke, A. L.; O'Riordan, M. X. D. *Cell Microbiol.* **2006**, *8*, 1720.
(432) Appelberg, R. *J. Leukocyte Biol.* **2006**, *79*, 1117.
(433) Wagner, D.; Maser, J.; Lai, B.; Cai, Z. H.; Barry, C. E.; Bentrup, K. H. Z.; Russell, D. G.; Bermudez, L. E. *J. Immunol.* **2005**, *174*, 1491.
(434) Tilley, L.; McFadden, G.; Cowman, A.; Klonis, N. *Trends Parasitol.* **2007**, *23*, 268.
(435) Williams, G. J.; Hanssen, E.; Peele, A. G.; Pfeifer, M. A.; Clark, J.; Abbey, B.; Cadenazzi, G.; de Jonge, M. D.; Vogt, S.; Tilley, L.; Nugent, K. A. *Cytometry, Part A* **2008**, *73A*, 949.
(436) Barceloux, D. G. *Clin. Toxicol.* **1999**, *37*, 201.
(437) Bresson, C.; Lamouroux, C.; Sandre, C.; Tabarant, M.; Gault, N.; Poncy, J. L.; Lefaix, U.; Den Auwer, C.; Spezia, R.; Gaigeot, M. P.; Ansoborlo, E.; Mounicou, S.; Frayssse, A.; Deves, G.; Bacquart, T.; Seznec, H.; Pouthier, T.; Moretto, P.; Ortega, R.; Lobinski, R.; Moulin, C. *Biochimie* **2006**, *88*, 1619.
(438) Bernstein, I. A.; Vaughan, F. L. *J. Toxicol. Environ. Health B* **1999**, *2*, 1.

(439) Lison, D.; De Boeck, M.; Verougstraete, V.; Kirsch-Volders, M. *Occup. Environ. Med.* **2001**, *58*, 619.
(440) Ortega, R.; Bresson, C.; Fraysse, A.; Sandre, C.; Devès, G.; Gombert, C.; Tabarant, M.; Bleuet, P.; Seznec, H.; Simionovici, A.; Moretto, P.; Moulin, C. *Toxicol. Lett.* **2009**, *188*, 26.
(441) Nemery, B.; Verbeken, E. K.; Demedts, M. *Semin. Respir. Crit. Care Med.* **2001**, *22*, 435.
(442) Kelleher, P.; Pacheco, K.; Newman, L. S. *Environ. Health Perspect.* **2000**, *108*, 685.
(443) Naqvi, A. H.; Hunt, A.; Burnett, B. R.; Abraham, J. L. *Arch. Environ. Occup. Health* **2008**, *63*, 51.
(444) Moriyama, H.; Kobayashi, M.; Takada, T.; Shimizu, T.; Terada, M.; Narita, J.; Maruyama, M.; Watanabe, K.; Suzuki, E.; Gejyo, F. *Am. J. Respir. Crit. Care Med.* **2007**, *176*, 70.
(445) Costa, M.; Klein, C. B. *Crit. Rev. Toxicol.* **2006**, *36*, 155.
(446) Urbano, A. M.; Rodrigues, C. F. D.; Alpoim, M. C. *Gene Ther. Mol. Biol.* **2008**, *12B*, 219.
(447) Zhitkovich, A. *Chem. Res. Toxicol.* **2005**, *18*, 3.
(448) Mulyani, I.; Levina, A.; Lay, P. A. *Angew. Chem., Int. Ed.* **2004**, *43*, 4504.
(449) Nguyen, A.; Mulyani, I.; Levina, A.; Lay, P. A. *Inorg. Chem.* **2008**, *47*, 4299.
(450) Dillon, C. T.; Lay, P. A.; Kennedy, B. J.; Stampfl, A. P. J.; Cai, Z. H.; Ilinski, P.; Rodrigues, W.; Legnini, D. G.; Lai, B.; Maser, J. *J. Biol. Inorg. Chem.* **2002**, *7*, 640.
(451) Dillon, C. T.; Kennedy, B. J.; Lay, P. A.; Lai, B.; Cai, Z.; Stampfl, A. P. J.; Ilinski, P.; Legnini, D.; Maser, J.; Rodrigues, W.; Shea-McCarthy, G.; Cholewa, M. *J. Phys. IV* **2003**, *104*, 293.
(452) Ortega, R.; Fayard, B.; Salome, M.; Deves, G.; Susini, J. *J. Phys. IV* **2003**, *104*, 289.
(453) Ortega, R.; Fayard, B.; Salome, M.; Deves, G.; Susini, J. *Chem. Res. Toxicol.* **2005**, *18*, 1512.
(454) Levina, A.; Lay, P. A. *Chem. Res. Toxicol.* **2008**, *21*, 563.
(455) Harris, H. H.; Levina, A.; Dillon, C. T.; Mulyani, I.; Lai, B.; Cai, Z. H.; Lay, P. A. *J. Biol. Inorg. Chem.* **2005**, *10*, 105.
(456) Carter, D. E.; Aposhian, H. V.; Gandolfi, A. J. *Toxicol. Appl. Pharmacol.* **2003**, *193*, 309.
(457) Thomas, D. J. *Toxicol. Appl. Pharmacol.* **2007**, *222*, 365.
(458) Lu, D. P.; Qiu, J. Y.; Jiang, B.; Wang, Q.; Liu, K. Y.; Liu, Y. R.; Chen, S. S. *Blood* **2002**, *99*, 3136.
(459) Don, A. S.; Kisker, O.; Dilda, P.; Donoghue, N.; Zhao, X. Y.; Decollogne, S.; Creighton, B.; Flynn, E.; Folkman, J.; Hogg, P. J. *Cancer Cell* **2003**, *3*, 497.
(460) Hayakawa, T.; Kobayashi, Y.; Cui, X.; Hirano, S. *Arch. Toxicol.* **2005**, *79*, 183.
(461) Challenger, F. *Chem. Rev.* **1945**, *36*, 315.
(462) Del Razo, L. M.; Stybo, M.; Cullen, W. R.; Thomas, D. J. *Toxicol. Appl. Pharmacol.* **2001**, *174*, 282.
(463) Vahidnia, A.; Van der Voet, G. B.; de Wolf, F. A. *Hum. Exp. Toxicol.* **2007**, *26*, 823.
(464) Rodriguez, V. M.; Carrizales, L.; Jimenez-Capdeville, M. E.; Dufour, L.; Giordano, M. *Brain Res. Bull.* **2001**, *55*, 301.
(465) Molin, Y.; Frisk, P.; Ilback, N. G. *Anti-Cancer Drugs* **2008**, *19*, 812.
(466) Kitchin, K. T. *Toxicol. Appl. Pharmacol.* **2001**, *172*, 249.
(467) Rubio, M.; Perez, R. D.; Perez, C. A.; Eynard, A. H.; Bongiovanni, G. A. *Radiat. Phys. Chem.* **2008**, *77*, 1.
(468) Zeng, H. W.; Uthus, E. O.; Combs, G. F. *J. Inorg. Biochem.* **2005**, *99*, 1269.
(469) Gailer, J. *Appl. Organomet. Chem.* **2002**, *16*, 701.
(470) Gailer, J.; Ruprecht, L.; Reitmeir, P.; Benker, M.; Schramel, P. *Appl. Organometal. Chem.* **2004**, *18*, 670.
(471) Bedwal, R. S.; Nair, N.; Sharma, M. P.; Mathur, R. S. *Med. Hypotheses* **1993**, *41*, 150.
(472) Berry, J. P.; Galle, P. *J. Submicrosc. Cytol. Pathol.* **1994**, *26*, 203.
(473) Nogueira, C. W.; Zeni, G.; Rocha, J. B. T. *Chem. Rev.* **2004**, *104*, 6255.
(474) Zeng, H. W.; Combs, G. F. *J. Nutr. Biochem.* **2008**, *19*, 1.
(475) Gailer, J.; George, G. N.; Pickering, I. J.; Prince, R. C.; Younis, H. S.; Winzerling, J. J. *Chem. Res. Toxicol.* **2002**, *15*, 1466.
(476) Burns, F. J.; Rossman, T.; Vega, K.; Uddin, A.; Vogt, S.; Lai, B.; Reeder, R. J. *Environ. Health Perspect.* **2008**, *116*, 703.
(477) Kehr, S.; Malinouski, M.; Finney, L.; Vogt, S.; Labunskyy, V. M.; Kasaikina, M. V.; Carlson, B. A.; Zhou, Y.; Hatfield, D. L.; Gladyshev, V. N. *J. Mol. Biol.* **2009**, *389*, 808.
(478) Huff, J.; Lunn, R. M.; Waalkes, M. P.; Tomatis, L.; Infante, P. F. *Int. J. Occup. Environ. Health* **2007**, *13*, 202.
(479) Giaginis, C.; Gatzidou, E.; Theocharis, S. *Toxicol. Appl. Pharmacol.* **2006**, *213*, 282.
(480) Nordberg, M. *Talanta* **1998**, *46*, 243.
(481) Coyle, P.; Philcox, J. C.; Carey, L. C.; Rofe, A. M. *Cell. Mol. Life Sci.* **2002**, *59*, 627.
(482) Noel, L.; Guerin, T.; Kolf-Clauw, M. *Food Chem. Toxicol.* **2004**, *42*, 1203.
(483) Nagamine, T.; Nakazato, K.; Suzuki, K.; Kusakabe, T.; Sakai, T.; Oikawa, A.; Satoh, T.; Kamiya, T.; Arakawa, K. *Biol. Trace Elem. Res.* **2007**, *117*, 115.
(484) Benoff, S.; Jacob, A.; Hurley, I. R. *Hum. Reprod. Update* **2000**, *6*, 107.
(485) Thompson, J.; Bannigan, J. *Reprod. Toxicol.* **2008**, *25*, 304.
(486) Yiin, S. J.; Chern, C. L.; Sheu, J. Y.; Lin, T. H. *Biometals* **1999**, *12*, 353.
(487) Kusakabe, T.; Nakajima, K.; Suzuki, K.; Nakazato, K.; Takada, H.; Satoh, T.; Oikawa, M.; Kobayashi, K.; Koyama, H.; Arakawa, K.; Nagamine, T. *Biometals* **2008**, *21*, 71.
(488) Kusakabe, T.; Nakajima, K.; Nakazato, K.; Suzuki, K.; Takada, H.; Satoh, T.; Oikawa, M.; Arakawa, K.; Nagamine, T. *Toxicol. in Vitro* **2008**, *22*, 1469.
(489) Tchounwou, P. B.; Ayensu, W. K.; Ninashvili, N.; Sutton, D. *Environ. Toxicol.* **2003**, *18*, 149.
(490) Risher, J. F.; Murray, E. H.; Prince, G. R. *Toxicol. Ind. Health* **2002**, *18*, 109.
(491) Shenker, B. J.; Datar, S.; Mansfield, K.; Shapiro, I. M. *Toxicol. Appl. Pharmacol.* **1997**, *143*, 397.
(492) Mueller, P. W.; Price, R. G.; Finn, W. F. *Environ. Health Perspect.* **1998**, *106*, 227.
(493) Edinger, A. L.; Thompson, C. B. *Curr. Opin. Cell Biol.* **2004**, *16*, 663.
(494) Homma-Takeda, S.; Takenaka, Y.; Kumagai, Y.; Shimojo, N. *Environ. Toxicol. Pharmacol.* **1999**, *7*, 179.
(495) Gailer, J. *Coord. Chem. Rev.* **2007**, *251*, 234.
(496) Korbas, M.; Blechinger, S. R.; Krone, P. H.; Pickering, I. J.; George, G. N. *Proc. Natl. Acad. Sci. U.S.A.* **2008**, *105*, 12108.
(497) Clifton, J. C. *Pediatr. Clin. North Am.* **2007**, *54*, 237.
(498) Harris, H. H.; Vogt, S.; Eastgate, H.; Legnini, D. G.; Hornberger, B.; Cai, Z.; Lai, B.; Lay, P. A. *J. Synchrot. Radiat.* **2008**, *15*, 123.
(499) Sprietsma, J. E. *Med. Hypotheses* **1999**, *53*, 6.
(500) Ilbäck, N. G.; Fohlman, J.; Friman, G.; Ehrnst, A. *Chemosphere* **1994**, *29*, 1145.
(501) Ilbäck, N. G.; Wesslen, L.; Fohlman, J.; Friman, G. *Toxicol. Lett.* **1996**, *89*, 19.
(502) Goyer, R. A. *Annu. Rev. Nutr.* **1997**, *17*, 37.
(503) South, P. K.; Morris, V. C.; Levander, O. A.; Smith, A. D. *J. Toxicol. Env. Health A* **2001**, *63*, 511.
(504) Ilbäck, N. G.; Lindh, C.; Minqin, R.; Friman, G.; Watt, F. *Biol. Trace Elem. Res.* **2005**, *108*, 215.
(505) Patrick, L. *Altern. Med. Rev.* **2006**, *11*, 2.
(506) Mansouri, M. T.; Cauli, O. *Environ. Toxicol. Pharmacol.* **2009**, *27*, 307.
(507) Zoeger, N.; Roschger, P.; Hofstaetter, J. G.; Jokubonis, C.; Pepponi, G.; Falkenberg, G.; Fratzl, P.; Berzlanovich, A.; Osterode, W.; Streli, C.; Wobrauschek, P. *Osteoarthr. Cartilage* **2006**, *14*, 906.
(508) Zoeger, N.; Streli, C.; Wobrauschek, P.; Jokubonis, C.; Pepponi, G.; Roschger, P.; Hofstaetter, J.; Berzianovich, A.; Wegrzynek, D.; Chinea-Cano, E.; Markowicz, A.; Simon, R.; Falkenberg, G. *X-Ray Spectrom.* **2008**, *37*, 3.
(509) Gemmel, A.; Tavares, M.; Alperin, S.; Soncini, J.; Daniel, D.; Dunn, J.; Crawford, S.; Braveman, N.; Clarkson, T. W.; McKinlay, S.; Bellinger, D. C. *Environ. Health Perspect.* **2002**, *110*, A625.
(510) Arora, M.; Chan, S. W. Y.; Kennedy, B. J.; Sharma, A.; Crisante, D.; Walker, D. M. *J. Trace Elem. Med. Biol.* **2004**, *18*, 135.
(511) Cerklewski, F. L. *J. Nutr.* **1981**, *111*, 1780.
(512) Takatsuka, T.; Tanaka, K.; Iijima, Y. *Dent. Mater.* **2005**, *21*, 1170.
(513) Batra, N.; Nehru, B.; Bansal, M. P. *Reprod. Toxicol.* **1998**, *12*, 535.
(514) Hsu, P. C.; Guo, Y. L. L. *Toxicology* **2002**, *180*, 33.
(515) Arora, M.; Kennedy, B. J.; Ryan, C. G.; Boadle, R. A.; Walker, D. M.; Harland, C. L.; Lai, B.; Cai, Z. H.; Vogt, S.; Zoellner, H.; Chan, S. W. Y. *Arch. Oral Biol.* **2007**, *52*, 938.
(516) Thomson, R. M.; Parry, G. J. *Muscle Nerve* **2006**, *33*, 732.
(517) Zoeger, N.; Wobrauschek, P.; Streli, C.; Pepponi, G.; Roschger, P.; Falkenberg, G.; Osterode, W. *X-Ray Spectrom.* **2005**, *34*, 140.
(518) Behets, G. J.; Verberckmoes, S. C.; D'Haese, P. C.; De Broe, M. E. *Curr. Opin. Nephrol. Hypertens.* **2004**, *13*, 403.
(519) Damment, S. J. P.; Pennick, M. *Clin. Pharmacokinet.* **2008**, *47*, 553.
(520) Behets, G. J.; Dams, G.; Vercauteren, S. R.; Damment, S. J.; Bouillon, R.; De Broe, M. E.; D'Haese, P. C. *J. Am. Soc. Nephrol.* **2004**, *15*, 2219.
(521) Behets, G. J.; Verberckmoes, S. C.; Oste, L.; Bervoets, A. R.; Salome, M.; Cox, A. G.; Denton, J.; De Broe, M. E.; D'Haese, P. C. *Kidney Int.* **2005**, *67*, 1830.
(522) Slatopolsky, E.; Liapis, H.; Finch, J. *Kidney Int.* **2005**, *68*, 2809.
(523) Bervoets, A. R. J.; Behets, G. J.; Schryvers, D.; Roels, F.; Yang, Z.; Verberckmoes, S. C.; Damment, S. J. P.; Dauwe, S.; Mubiana, V. K.; Blust, R.; De Broe, M. E.; D'Haese, P. C. *Kidney Int.* **2009**, *75*, 389.

(524) Rodriguez, I.; Perez-Rial, S.; Gonzalez-Jimenez, J.; Perez-Sanchez, J. M.; Herranz, F.; Beckmann, N.; Ruiz-Cabello, J. *J. Pharm. Sci.* **2008**, *97*, 3637.
(525) Hermann, P.; Kotek, J.; Kubicek, V.; Lukes, I. *Dalton Trans.* **2008**, 3027.
(526) Thomsen, H. S. *J. Magnet. Reson. Imag.* **2008**, *28*, 284.
(527) Endres, P. J.; MacRenaris, K. W.; Vogt, S.; Allen, M. J.; Meade, T. J. *Mol. Imaging* **2006**, *5*, 485.
(528) Lee, J.; Burclette, J. E.; MacRenaris, K. W.; Mustafi, D.; Woodruff, T. K.; Meade, T. J. *Chem. Biol.* **2007**, *14*, 824.
(529) Endres, P. J.; MacRenaris, K. W.; Vogt, S.; Meade, T. J. *Bioconjugate Chem.* **2008**, *19*, 2049.
(530) Allen, M. J.; Meade, T. J. *J. Biol. Inorg. Chem.* **2003**, *8*, 746.
(531) Bullok, K. E.; Gammon, S. T.; Violini, S.; Prantner, A. M.; Villalobos, V. M.; Sharma, V.; Piwnica-Worms, D. *Mol. Imaging* **2006**, *5*, 1.
(532) Chrzascik, I. *Crit. Rev. Anal. Chem.* **2009**, *39*, 70.
(533) Ahlem, A.; Ali, E. H.; Leila, T. *Biol. Trace Elem. Res.* **2008**, *124*, 40.
(534) Biellmann, J. F. *Chem. Rev.* **2003**, *103*, 2019.
(535) Lee, J.; Zylka, M. J.; Anderson, D. J.; Burdette, J. E.; Woodruff, T. K.; Meade, T. J. *J. Am. Chem. Soc.* **2005**, *127*, 13164.
(536) Craft, E. S.; Abu-Qare, A. W.; Flaherty, M. M.; Garofolo, M. C.; Rincavage, H. L.; Abou-Donia, M. B. *J. Toxicol. Env. Health B* **2004**, *7*, 297.
(537) Carrière, M.; Gouget, B.; Gallien, J. P.; Avoscan, L.; Gobin, R.; Verbavatz, J. M.; Khodja, H. *Nucl. Instrum. Methods Phys. Res., Sect. B* **2005**, *231*, 268.
(538) Carrière, M.; Proux, O.; Milgram, S.; Thiebault, C.; Avoscan, L.; Barre, N.; Den Auwer, C.; Gouget, B. *J. Biol. Inorg. Chem.* **2008**, *13*, 655.
(539) Donnadieu-Claraz, M.; Bonnehorgne, M.; Dhieux, B.; Maubert, C.; Cheynet, M.; Paquet, F.; Gourmelon, P. *Radiat. Res.* **2007**, *167*, 454.
(540) Milgram, S.; Carriere, M.; Thiebault, C.; Berger, P.; Khodja, H.; Gouget, B. *Nucl. Instrum. Methods Phys. Res., Sect. B* **2007**, *260*, 254.
(541) Kim, J.; Piao, Y.; Hyeon, T. *Chem. Soc. Rev.* **2009**, *38*, 372.
(542) Suh, W. H.; Suslick, K. S.; Stucky, G. D.; Suh, Y. H. *Prog. Neurobiol.* **2009**, *87*, 133.
(543) Paunesku, T.; Rajh, T.; Wiederrecht, G.; Maser, J.; Vogt, S.; Stojicevic, N.; Protic, M.; Lai, B.; Oryhon, J.; Thurnauer, M.; Woloschak, G. *Nat. Mater.* **2003**, *2*, 343.
(544) Paunesku, T.; Vogt, S.; Lai, B.; Maser, J.; Stojićević, N.; Thurn, K. T.; Osipo, C.; Liu, H.; Legnini, D.; Wang, Z.; Lee, C.; Woloschak, G. E. *Nano Lett.* **2007**, *7*, 596.
(545) Endres, P. J.; Paunesku, T.; Vogt, S.; Meade, T. J.; Woloschak, G. E. *J. Am. Chem. Soc.* **2007**, *129*, 15760.
(546) Thurn, K. T.; Paunesku, T.; Wu, A.; Brown, E. M. B.; Lai, B.; Vogt, S.; Maser, J.; Aslam, M.; Dravid, V.; Bergan, R.; Woloschak, G. E. *Small* **2009**, *5*, 1318.
(547) Jacobsen, C. *Trends Cell. Biol.* **1999**, *9*, 44.
(548) Kucheyev, S. O.; van Buuren, T.; Baumann, T. F.; Satcher, J. H.; Willey, T. M.; Meulenberg, R. W.; Felter, T. E.; Poco, J. F.; Gammon, S. A.; Terminello, L. J. *Phys. Rev. B* **2004**, *69*, 7.
(549) Ashcroft, J. M.; Gu, W.; Zhang, T.; Hughes, S. M.; Hartman, K. B.; Hofmann, C.; Kanaras, A. G.; Kilcoyne, D. A.; Le Gros, M.; Yin, Y.; Alivisatos, A. P.; Larabell, C. A. *Chem. Commun.* **2008**, 2471.
(550) Grzanka, A. *Acta Histochem.* **2001**, *103*, 453.
(551) Bendayan, M. *Biotechnol. Histochem.* **2000**, *75*, 203.
(552) Robinson, J. M.; Takizawa, T.; Vandre, D. D.; Burry, R. W. *Microsc. Res. Technol.* **1998**, *42*, 13.
(553) Robinson, J. M.; Takizawa, T.; Vandre, D. D. *J. Microsc. Oxford* **2000**, *199*, 163.
(554) Weipoltshammer, K.; Schofer, C.; Almeder, M.; Wachtler, F. *Histochem. Cell Biol.* **2000**, *114*, 489.
(555) Jain, P. K.; Huang, X. H.; El-Sayed, I. H.; El-Sayed, M. A. *Acc. Chem. Res.* **2008**, *41*, 1578.
(556) Reiss, P.; Protiere, M.; Li, L. *Small* **2009**, *5*, 154.
(557) Costa-Fernández, J. M.; Pereiro, R.; Sanz-Medel, A. *Trends Anal. Chem.* **2006**, *25*, 207.
(558) Somers, R. C.; Bawendi, M. G.; Nocera, D. G. *Chem. Soc. Rev.* **2007**, *36*, 579.
(559) Chan, W. C. W.; Nie, S. M. *Science* **1998**, *281*, 2016.
(560) Bruchez, M.; Moronne, M.; Gin, P.; Weiss, S.; Alivisatos, A. P. *Science* **1998**, *281*, 2013.
(561) Corezzi, S.; Urbanelli, L.; Cloetens, P.; Emiliani, C.; Helfen, L.; Bohic, S.; Elisei, F.; Fioretto, D. *Anal. Biochem.* **2009**, *388*, 33.
(562) Ju-Nam, Y.; Lead, J. R. *Sci. Total Environ.* **2008**, *400*, 396.
(563) Moghimi, S. M.; Hunter, A. C.; Murray, J. C. *FASEB J.* **2005**, *19*, 311.
(564) Unfried, K.; Albrecht, C.; Klotz, L. O.; Von Mikecz, A.; Grether-Beck, S.; Schins, R. P. F. *Nanotoxicology* **2007**, *1*, 52.
(565) Serpone, N.; Dondi, D.; Albini, A. *Inorg. Chim. Acta* **2007**, *360*, 794.
(566) Kahru, A.; Dubourguier, H. C.; Blinova, I.; Ivask, A.; Kasemets, K. *Sensors* **2008**, *8*, 5153.
(567) Tan, M. H.; Commens, C. A.; Burnett, L.; Snitch, P. J. *Australas. J. Dermatol.* **1996**, *37*, 185.
(568) Lekki, J.; Stachura, Z.; Dabros, W.; Stachura, J.; Menzel, F.; Reinert, T.; Butz, T.; Pallon, J.; Gontier, E.; Ynsa, M. D.; Moretto, P.; Kertesz, Z.; Szikszai, Z.; Kiss, A. Z. *Nucl. Instrum. Methods Phys. Res., Sect. B* **2007**, *260*, 174.
(569) Laurent, S.; Forge, D.; Port, M.; Roch, A.; Robic, C.; Elst, L. V.; Muller, R. N. *Chem. Rev.* **2008**, *108*, 2064.
(570) Wang, B.; Feng, W. Y.; Wang, M.; Shi, J. W.; Zhang, F.; Ouyang, H.; Zhao, Y. L.; Chai, Z. F.; Huang, Y. Y.; Xie, Y. N.; Wang, H. F.; Wang, J. *Biol. Trace Elem. Res.* **2007**, *118*, 233.
(571) Gao, Y.; Liu, N. Q.; Chen, C. Y.; Luo, Y. F.; Li, Y. F.; Zhang, Z. Y.; Zhao, Y. L.; Zhao, B. L.; Iida, A.; Chai, Z. F. *J. Anal. At. Spectrom.* **2008**, *23*, 1121.
(572) Tejral, G.; Panyala, N. R.; Havel, J. *J. Appl. Biomed.* **2009**, *7*, 1.
(573) Pumera, M. *Chem.—Eur. J.* **2009**, *15*, 4970.
(574) Zhang, L. W.; Zeng, L. L.; Barron, A. R.; Monteiro-Riviere, N. A. *Int. J. Toxicol.* **2007**, *26*, 103.
(575) Cheng, J. P.; Flahaut, E.; Cheng, S. H. *Environ. Toxicol. Chem.* **2007**, *26*, 708.
(576) Bussy, C.; Cambedouzou, J.; Lanone, S.; Leccia, E.; Heresanu, V.; Pinault, M.; Mayne-I'Hermite, M.; Brun, N.; Mory, C.; Cotte, M.; Doucet, J.; Boczkowski, J.; Launoist, P. *Nano Lett.* **2008**, *8*, 2659.
(577) Biju, V.; Itoh, T.; Anas, A.; Sujith, A.; Ishikawa, M. *Anal. Bioanal. Chem.* **2008**, *391*, 2469.
(578) Medintz, I. L.; Mattoussi, H.; Clapp, A. R. *Int. J. Nanomed.* **2008**, *3*, 151.
(579) Jackson, B. P.; Pace, H.; Lanzirotti, A.; Smith, R.; Ranville, J. F. *Anal. Bioanal. Chem.* **2009**, *394*, 911.
(580) Kemner, K. M.; Kelly, S. D.; Lai, B.; Maser, J.; O'Loughlin, E. J.; Sholto-Douglas, D.; Cai, Z. H.; Schneegurt, M. A.; Kulpa, C. F.; Nealson, K. H. *Science* **2004**, *306*, 686.
(581) Liu, C. X.; Gorby, Y. A.; Zachara, J. M.; Fredrickson, J. K.; Brown, C. F. *Biotechnol. Bioeng.* **2002**, *80*, 637.
(582) Fredrickson, J. K.; Romine, M. F. *Curr. Opin. Biotechnol.* **2005**, *16*, 269.
(583) Wilkins, M. J.; Livens, F. R.; Vaughan, D. J.; Lloyd, J. R. *Biogeochemistry* **2006**, *78*, 125.
(584) Marshall, M. J.; Beliaev, A. S.; Dohnalkova, A. C.; Kennedy, D. W.; Shi, L.; Wang, Z. M.; Boyanov, M. I.; Lai, B.; Kemner, K. M.; McLean, J. S.; Reed, S. B.; Culley, D. E.; Bailey, V. L.; Simonson, C. J.; Saffarini, D. A.; Romine, M. F.; Zachara, J. M.; Fredrickson, J. K. *PLoS Biol.* **2006**, *4*, 1324.
(585) Michibata, H.; Uyama, T.; Ueki, T.; Kanamori, K. *Microsc. Res. Technol.* **2002**, *56*, 421.
(586) Ueki, T.; Takemoto, K.; Fayard, B.; Salome, M.; Yamamoto, A.; Kihara, H.; Susini, J.; Scippa, S.; Uyama, T.; Michibata, H. *Zool. Sci.* **2002**, *19*, 27.
(587) Takemoto, K.; Ueki, T.; Fayard, B.; Yamamoto, A.; Salome, M.; Scippa, S.; Susini, J.; Uyama, T.; Michibata, H.; Kihara, H. *J. Phys. IV* **2003**, *104*, 333.
(588) Daly, M. J.; Gaidamakova, E. K.; Matrosova, V. Y.; Vasilenko, A.; Zhai, M.; Leapman, R. D.; Lai, B.; Ravel, B.; Li, S. M. W.; Kemner, K. M.; Fredrickson, J. K. *PLoS Biol.* **2007**, *5*, 769.
(589) Archibald, F. S.; Fridovich, I. *Arch. Biochem. Biophys.* **1982**, *214*, 452.
(590) Twining, B. S.; Baines, S. B.; Fisher, N. S. *Limnol. Oceanogr.* **2004**, *49*, 2115.
(591) Twining, B. S.; Baines, S. B.; Fisher, N. S.; Landry, M. R. *Deep-Sea Res., Part I: Oceanogr. Res. Pap.* **2004**, *51*, 1827.
(592) Twining, B. S.; Baines, S. B.; Fisher, N. S.; Jacobsen, C.; Maser, J. *J. Phys. IV* **2003**, *104*, 435.
(593) De Samber, B.; Silversmit, G.; Evens, R.; De Schamphelaere, K.; Janssen, C.; Masschaele, B.; Van Hoorebeke, L.; Balcaen, L.; Vanhaecke, F.; Falkenberg, G.; Vincze, L. *Anal. Bioanal. Chem.* **2008**, *390*, 267.
(594) Lipinski, M. R.; Przybylowicz, W. J.; Durholtz, M. D.; Mesjasz-Przybylowicz, J. *Nucl. Instrum. Methods Phys. Res., Sect. B* **1997**, *130*, 374.
(595) Doubleday, Z.; Belton, D.; Pecl, G.; Semmens, J. *Nucl. Instrum. Methods Phys. Res., Sect. B* **2008**, *266*, 67.
(596) Lichtenegger, H. C.; Birkedal, H.; Casa, D. M.; Cross, J. O.; Heald, S. M.; Waite, J. H.; Stucky, G. D. *Chem. Mater.* **2005**, *17*, 2927.
(597) Yamauchi, M.; Tanaka, J.; Harada, Y. *Acta Oto-Laryngol.* **2008**, *128*, 846.
(598) Marigomez, I.; Soto, M.; Cajaraville, M. P.; Angulo, E.; Giamberini, L. *Microsc. Res. Technol.* **2002**, *56*, 358.
(599) McDonnell, L. A.; Heeren, R. M. A. *Mass Spectrom. Rev.* **2007**, *26*, 606.
(600) Herzog, R. F. K.; Viehböck, F. P. *Phys. Rev.* **1949**, *76*, 855.

(601) Castaing, R.; Slodzian, G. *C. R. Hebd. Acad. Sci. Paris.* **1962**, *255*, 1893.
(602) Liebl, H. *J. Appl. Phys.* **1967**, *38*, 5277.
(603) Slodzian, G.; Daigne, B.; Girard, F.; Boust, F.; Hillon, F. In *Proceedings of the 8th International Conference on Secondary Ion Mass Spectrometry, SIMS VIII*; Benninghoven, A., Janssen, K. T. F., Tumpner, J., Werner, H. W., Eds.; John Wiley & Sons: New York, 1991.
(604) Slodzian, G.; Daigne, B.; Girard, F.; Boust, F.; Hillion, F. *Biol. Cell* **1992**, *74*, 43.
(605) Chandra, S.; Smith, D. R.; Morrison, G. H. *Anal. Chem.* **2000**, *72*, 104A.
(606) Guerquin-Kern, J. L.; Wu, T. D.; Quintana, C.; Croisy, A. *Biochim. Biophys. Acta* **2005**, *1724*, 228.
(607) Chandra, S. *Appl. Surf. Sci.* **2003**, *203*, 679.
(608) Chandra, S. *Appl. Surf. Sci.* **2004**, 467.
(609) Betti, M. *Int. J. Mass Spectrom.* **2005**, *242*, 169.
(610) Levi-Setti, R.; Gavrilov, K. L.; Neilly, M. E. *Appl. Surf. Sci.* **2006**, *252*, 6765.
(611) Chandra, S.; Harris, W. C.; Morrison, G. H. *J. Histochem. Cytochem.* **1984**, *32*, 1224.
(612) Strick, R.; Strissel, P. L.; Gavrilov, K.; Levi-Setti, R. *J. Cell Biol.* **2001**, *155*, 899.
(613) Adachi, Y.; Luke, M.; Laemmli, U. K. *Cell* **1991**, *64*, 137.
(614) Levi-Setti, R.; Gavrilov, K. L.; Strissel, P. L.; Strick, R. *Appl. Surf. Sci.* **2004**, *231*−*232*, 479.
(615) Levi-Setti, R.; Gavrilov, K. L.; Neilly, M. E.; Strick, R.; Strissel, P. L. *Appl. Surf. Sci.* **2006**, *252*, 6907.
(616) Herzog, M.; Soyer, M. O. *Eur. J. Cell Biol.* **1983**, *30*, 33.
(617) Metivier, C.; Soyergobillard, M. O. *Biol. Cell* **1986**, *56*, 163.
(618) Rizzo, P. J. *Cell Res.* **2003**, *13*, 215.
(619) Levi-Setti, R.; Gavrilov, K. L.; Rizzo, P. J. *Eur. J. Cell. Biol* **2008**, *87*, 963.
(620) Strissel, P. L.; Gavrilov, K. L.; Levi-Setti, R.; Strick, R. *Appl. Surf. Sci.* **2006**, *252*, 6770.
(621) Chandra, S. *J. Microsc. (Oxford, U.K.)* **2001**, *204*, 150.
(622) Chandra, S. *Eur. J. Cell. Biol.* **2005**, *84*, 783.
(623) Chandra, S.; Ausserer, W. A.; Morrison, G. H. *J. Cell Sci.* **1992**, *102*, 417.
(624) Chandra, S.; Morrison, G. H. *Int. J. Mass Spectrom. Ion Processes* **1995**, *143*, 161.
(625) Chandra, S.; Kable, E. P. W.; Morrison, G. H.; Webb, W. W. *J. Cell Sci.* **1991**, *100*, 747.
(626) Chandra, S.; Fewtrell, C.; Millard, P. J.; Sandison, D. R.; Webb, W. W.; Morrison, G. H. *J. Biol. Chem.* **1994**, *269*, 15186.
(627) Chandra, S.; Lorey, D. R. *Cell. Mol. Biol.* **2001**, *47*, 503.
(628) Smith, D. R.; Chandra, S.; Barth, R. F.; Yang, W. L.; Joel, D. D.; Coderre, J. A. *Cancer Res.* **2001**, *61*, 8179.
(629) Chandra, S.; Lorey, D. R.; Smith, D. R. *Radiat. Res.* **2002**, *157*, 700.
(630) Chandra, S.; Lorey, D. R. *Int. J. Mass Spectrom.* **2007**, *260*, 90.
(631) Chandra, S.; Tjarks, W.; Lorey, D. R.; Barth, R. F. *J. Microsc. (Oxford, U.K.)* **2008**, *229*, 92.
(632) Barth, R. F.; Joensuu, H. *Radiother. Oncol.* **2007**, *82*, 119.
(633) Arlinghaus, H. F.; Kriegeskotte, C.; Fartmann, M.; Wittig, A.; Sauerwein, W.; Lipinsky, D. *Appl. Surf. Sci.* **2006**, *252*, 6941.
(634) Fartmann, M.; Dambach, S.; Kriegeskotte, C.; Lipinsky, D.; Wiesmann, H. P.; Wittig, A.; Sauerwein, W.; Arlinghaus, H. F. *Appl. Surf. Sci.* **2003**, *203*, 726.
(635) Fartmann, M.; Dambach, S.; Kriegeskotte, C.; Wiesmann, H. P.; Wittig, A.; Sauerwein, W.; Lipinsky, D.; Arlinghaus, H. F. *Surf. Interface Anal.* **2002**, *34*, 63.
(636) Dickinson, M.; Heard, P. J.; Barker, J. H. A.; Lewis, A. C.; Mallard, D.; Allen, G. C. *Appl. Surf. Sci.* **2006**, *252*, 6793.
(637) Chandra, S.; Morrison, G. H. *Science* **1985**, *228*, 1543.
(638) Cowan, J. A. *The Biological Chemistry of Magnesium*; VCH: New York, 1995.
(639) Musso, C. G. *Int. Urol. Nephrol.* **2009**, *41*, 357.
(640) Chandra, S.; Morrison, G. H. *J. Microsc. (Oxford, U.K.)* **1997**, *188*, 182.
(641) Chandra, S.; Morrison, G. H.; Beyenbach, K. W. *Am. J. Physiol.* **1997**, *273*, F939.
(642) Wasserman, R. H.; Brindak, M. E.; Meyer, S. A.; Fullmer, C. S. *Proc. Natl. Acad. Sci. U.S.A.* **1982**, *79*, 7939.
(643) Chandra, S.; Fullmer, C. S.; Smith, C. A.; Wasserman, R. H.; Morrison, G. H. *Proc. Natl. Acad. Sci. U.S.A.* **1990**, *87*, 5715.
(644) Mai, F. D.; Chen, B. J.; Ling, Y. C.; Wu, U. I.; Huang, Y. L.; Chang, H. M. *Appl. Surf. Sci.* **2008**, *255*, 1135.
(645) Ylitalo, P.; Karppane, H; Paasonen, M. K. *Nature* **1974**, *247*, 58.
(646) Hyde, T. M.; Miselis, R. R. *Am. J. Physiol.* **1984**, *247*, R173.
(647) Boxer, S. G.; Kraft, M. L.; Weber, P. K. *Annu. Rev. Biophys.* **2009**, *38*, 53.
(648) Champion, C.; Elbast, M.; Wu, T. D.; Colas-Linhart, N. *Braz. Arch. Biol. Technol.* **2007**, *50*, 135.
(649) Elbast, M.; Wu, T. D.; Guiraud-Vitaux, F.; Petiet, A.; Hindie, E.; Champion, C.; Croisy, A.; Guerquin-Kern, J. L.; Colas-Linhart, N. *C. R. Biol.* **2008**, *331*, 13.
(650) Labarre, P.; Papon, J.; Rose, A. H.; Guerquin-Kern, J. L.; Morandeau, L.; Wu, T. D.; Moreau, M. F.; Bayle, M.; Chezal, J. M.; Croisy, A.; Madelmont, J. C.; Turner, H.; Moins, N. *Nucl. Med. Biol.* **2008**, *35*, 783.
(651) Guerquin-Kern, J. L.; Hillion, F.; Madelmont, J. C.; Labarre, P.; Papon, J.; Croisy, A. *Biomed. Eng. Online* **2004**, *3*, 10.
(652) Bonnet-Duquennoy, M.; Papon, J.; Mishellany, F.; Labarre, P.; Guerquin-Kern, J. L.; Wu, T. D.; Gardette, M.; Maublant, J.; Penault-Llorca, F.; Miot-Noirault, E.; Cayre, A.; Madelmont, J. C.; Chezal, J. M.; Moins, N. *Int. J. Cancer* **2009**, *125*, 708.
(653) Lechene, C.; Hillion, F.; McMahon, G.; Benson, D.; Kleinfeld, A. M.; Kampf, J. P.; Distel, D.; Luyten, Y.; Bonventre, J.; Hentschel, D.; Park, K. M.; Ito, S.; Schwartz, M.; Benichou, G.; Slodzian, G. *J. Biol.* **2006**, *5*, 20.
(654) Behrens, S.; Losekann, T.; Pett-Ridge, J.; Weber, P. K.; Ng, W. O.; Stevenson, B. S.; Hutcheon, I. D.; Relman, D. A.; Spormann, A. M. *Appl. Environ. Microbiol.* **2008**, *74*, 3143.
(655) Musat, N.; Halm, H.; Winterholler, B.; Hoppe, P.; Peduzzi, S.; Hillion, F.; Horreard, F.; Amann, R.; Jorgensen, B. B.; Kuypers, M. M. M. *Proc. Natl. Acad. Sci. U.S.A.* **2008**, *105*, 17861.
(656) Audinot, J. N.; Guignard, C.; Migeon, H. N.; Hoffmann, L. *Appl. Surf. Sci.* **2006**, 6813.
(657) Eybe, T.; Audinot, J. N.; Bohn, T.; Guignard, C.; Migeon, H. N.; Hoffmann, L. *J. Appl. Microbiol.* **2008**, *105*, 1502.
(658) Verhaeghe, E. F.; Fraysse, A.; Guerquin-Kern, J. L.; Wu, T. D.; Deves, G.; Mioskowski, C.; Leblanc, C.; Ortega, R.; Ambroise, Y.; Potin, P. *J. Biol. Inorg. Chem.* **2008**, *13*, 257.
(659) Kilburn, M. R.; Wacey, D. *Appl. Surf. Sci.* **2008**, *255*, 1465.
(660) Sano, Y.; Shirai, K.; Takahata, N.; Hirata, T.; Sturchio, N. C. *Anal. Sci.* **2005**, *21*, 1091.
(661) Zumholz, K.; Hansteen, T.; Hillion, F.; Horreard, F.; Piatkowski, U. *Rev. Fish Biol. Fisheries* **2007**, *17*, 487.
(662) McKee, M. D.; Addison, W. N.; Kaartinen, M. T. *Cells Tissues Organs* **2005**, 181.
(663) Azari, F.; Vali, H.; Guerquin-Kern, J. L.; Wu, T. D.; Croisy, A.; Sears, S. K.; Tabrizian, M.; McKee, M. D. *J. Struct. Biol.* **2008**, *162*, 468.
(664) Zecca, L.; Youdim, M. B. H.; Riederer, P.; Connor, J. R.; Crichton, R. R. *Nat. Rev. Neurosci.* **2004**, *5*, 863.
(665) Markesbery, W. R. *Free Radical Biol. Med.* **1997**, *23*, 134.
(666) Bartzokis, G. *Neurobiol. Aging* **2004**, *25*, 5.
(667) Quintana, C.; Bellefqih, S.; Laval, J. Y.; Guerquin-Kern, J. L.; Wu, T. D.; Avila, J.; Ferrer, I.; Arranz, R.; Patino, C. *J. Struct. Biol.* **2006**, *153*, 42.
(668) Quintana, C.; Wu, T. D.; Delatour, B.; Dhenain, M.; Guerquin-Kern, J. L.; Croisy, A. *Microsc. Res. Technol.* **2007**, *70*, 281.
(669) Zukor, H.; Song, W.; Liberman, A.; Mui, J.; Vali, H.; Fillebeen, C.; Pantopoulos, K.; Wu, T. D.; Guerquin-Kern, J. L.; Schipper, H. M. *J. Neurochem.* **2009**, *109*, 776.
(670) Schipper, H. M.; Stopa, E. G. *Ann. Neurol.* **1995**, *37*, 758.
(671) Moreira, P. I.; Siedlak, S. L.; Wang, X. L.; Santos, M. S.; Oliveira, C. R.; Tabaton, M.; Nunomura, A.; Szweda, L. I.; Aliev, G.; Smith, M. A.; Zhu, X. W.; Perry, G. *Autophagy* **2007**, *3*, 614.
(672) Ma, Y. R.; Aichmayer, B.; Paris, O.; Fratzl, P.; Meibom, A.; Metzler, R. A.; Politi, Y.; Addadi, L.; Gilbert, P.; Weiner, S. *Proc. Natl. Acad. Sci. U.S.A.* **2009**, *106*, 6048.
(673) Hallegot, P.; Walter, P.; Cotte, M.; Audinot, J. N.; Guillot, J.; Migeon, H. N.; Tallarek, E.; Hagenhoff, B. *Appl. Surf. Sci.* **2008**, *255*, 1154.
(674) Slaveykova, V. I.; Guignard, C.; Eybe, T.; Migeon, H. N.; Hoffmann, L. *Anal. Bioanal. Chem.* **2009**, *393*, 583.
(675) Smart, K. E.; Kilburn, M.; Schroeder, M.; Martin, B. G. H.; Hawes, C.; Marsh, J. M.; Grovenor, C. R. M. *J. Cosmet. Sci.* **2009**, *60*, 337.
(676) Smart, K. E.; Kilburn, M. R.; Salter, C. J.; Smith, J. A. C.; Grovenor, C. R. M. *Int. J. Mass Spectrom.* **2007**, *260*, 107.
(677) Dauphas, S.; Delhaye, T.; Lavastre, O.; Corlu, A.; Guguen-Guillouzo, C.; Ababou-Girard, S.; Geneste, F. *Anal. Chem.* **2008**, *80*, 5958.
(678) Becker, J. S. *J. Anal. At. Spectrom.* **2002**, *17*, 1172.
(679) Beauchemin, D. *Anal. Chem.* **2008**, *80*, 4455.
(680) Becker, J. S. *J. Anal. At. Spectrom.* **2005**, *20*, 1173.
(681) Mokgalaka, N. S.; Gardea-Torresdey, J. L. *Appl. Spectrosc. Rev.* **2006**, *41*, 131.
(682) Gray, A. L. *Analyst* **1985**, *110*, 551.
(683) Becker, J. S.; Su, J.; Zoriya, M. V.; Dobrowolska, J.; Matusch, A. *Eur. J. Mass Spectrom.* **2007**, *13*, 1.
(684) Becker, J. S.; Zoriy, M.; Becker, J. S.; Dobrowolska, J.; Matusch, A. *J. Anal. At. Spectrom.* **2007**, *22*, 736.
(685) Becker, J. S.; Zoriy, M.; Wu, B.; Matusch, A. *J. Anal. At. Spectrom.* **2008**, *23*, 1275.
(686) Becker, J. S.; Zoriy, M.; Dressler, V. L.; Wu, B. *Pure Appl. Chem.* **2008**, *80*, 2643.

(687) Garbe-Schönberg, C. D.; Reimann, C.; Pavlov, V. A. *Environ. Geol.* **1997**, *32*, 9.
(688) Watmough, S. A.; Hutchinson, T. C.; Evans, R. D. *J. Environ. Qual.* **1998**, *27*, 1087.
(689) Watmough, S. A.; Hutchinson, T. C.; Evans, R. D. *Environ. Sci. Technol.* **1998**, *32*, 2185.
(690) Hoffmann, E.; Lüdke, C.; Scholze, H.; Stephanowitz, H. *Fresenius J. Anal. Chem.* **1994**, *350*, 253.
(691) Narewski, U.; Werner, G.; Schulz, H.; Vogt, C. *Fresenius J. Anal. Chem.* **2000**, *366*, 167.
(692) Hoffmann, E.; Lüdke, C.; Skole, J.; Stephanowitz, H.; Ullrich, E.; Colditz, D. *Fresenius J. Anal. Chem.* **2000**, *367*, 579.
(693) Lee, K. M.; Appleton, J.; Cooke, M.; Keenan, F.; Sawicka-Kapusta, K. *Anal. Chim. Acta* **1999**, *395*, 179.
(694) Lochner, F.; Appleton, J.; Keenan, F.; Cooke, M. *Anal. Chim. Acta* **1999**, *401*, 299.
(695) Richardson, C. A.; Chenery, S. R. N.; Cook, J. M. *Mar. Ecol.: Prog. Ser.* **2001**, *211*, 157.
(696) Price, G. D.; Pearce, N. J. G. *Mar. Pollut. Bull.* **1997**, *34*, 1025.
(697) Bellotto, V. R.; Miekeley, N. *Fresenius J. Anal. Chem* **2000**, *367*, 635.
(698) Toland, H.; Perkins, B.; Pearce, N.; Keenan, F.; Leng, M. J. *J. Anal. At. Spectrom.* **2000**, *15*, 1143.
(699) Vander Putten, E.; Dehairs, F.; Keppens, E.; Baeyens, W. *Geochim. Cosmochim. Acta* **2000**, *64*, 997.
(700) Feldmann, J.; Kindness, A.; Ek, P. *J. Anal. At. Spectrom.* **2002**, *17*, 813.
(701) Kindness, A.; Sekaran, C. N.; Feldmann, J. *Clin. Chem.* **2003**, *49*, 1916.
(702) Becker, J. S.; Zoriy, M. V.; Pickhardt, C.; Palomero-Gallagher, N.; Zilles, K. *Anal. Chem.* **2005**, *77*, 3208.
(703) Becker, J. S.; Zoriy, M. V.; Pickhardta, C.; Zillesb, K. *J. Anal. At. Spectrom.* **2005**, *20*, 912.
(704) Jackson, B.; Harper, S.; Smith, L.; Flinn, J. *Anal. Bioanal. Chem.* **2006**, *384*, 951.
(705) Zoriy, M. V.; Becker, J. S. *Int. J. Mass Spectrom.* **2007**, *264*, 175.
(706) Dobrowolska, J.; Dehnhardt, M.; Matusch, A.; Zoriy, M.; Palomero-Gallagher, N.; Koscielniak, P.; Zilles, K.; Becker, J. S. *Talanta* **2008**, *74*, 717.
(707) Zoriy, M. V.; Dehnhardt, M.; Reifenberger, G.; Zilles, K.; Becker, J. S. *Int. J. Mass Spectrom.* **2006**, *257*, 27.
(708) Zoriy, M. V.; Dehnhardt, M.; Matusch, A.; Becker, J. S. *Spectrochim. Acta B* **2008**, *63*, 375.
(709) Becker, J. S.; Dobrowolska, J.; Zoriy, M.; Matusch, A. *Rapid Commun. Mass Spectrom.* **2008**, *22*, 2768.
(710) Hutchinson, R. W.; Cox, A. G.; McLeod, C. W.; Marshall, P. S.; Harper, A.; Dawson, E. L.; Howlett, D. R. *Anal. Biochem.* **2005**, *346*, 225.
(711) Hare, D.; Reedy, B.; Grimm, R.; Simon, W.; Volitakis, I.; George, J. L.; Cherny, R. A.; Bush, A. I.; Finkelstein, D. I.; Doble, P. *Metallomics* **2009**, *1*, 53.
(712) Hare, D.; Burger, F.; Austin, C.; Fryer, F.; Grimm, R.; Reedy, B.; Scolyer, R. A.; Thompson, J. F.; Doble, P. *Analyst* **2009**, *134*, 450.
(713) Seuma, J.; Bunch, J.; Cox, A.; McLeod, C.; Bell, J.; Murray, C. *Proteomics* **2008**, *8*, 3775.
(714) Zoriy, M.; Matusch, A.; Spruss, T.; Becker, J. S. *Int. J. Mass Spectrom.* **2007**, *260*, 102.
(715) Austin, C.; Hare, D.; Rozelle, A. L.; Robinson, W. H.; Grimm, R.; Doble, P. *Metallomics* **2009**, *1*, 142.
(716) Becker, J. S.; Matusch, A.; Depboylu, C.; Dobrowolska, J.; Zoriy, M. V. *Anal. Chem.* **2007**, *79*, 6074.
(717) Becker, J. S.; Dietrich, R. C.; Matusch, A.; Pozebon, D.; Dressier, V. L. *Spectrochim. Acta B* **2008**, *63*, 1248.
(718) Wu, B.; Chen, Y. X.; Becker, J. S. *Anal. Chim. Acta* **2009**, *633*, 165.
(719) Wu, B.; Zoriy, M.; Chen, Y. X.; Becker, J. S. *Talanta* **2009**, *78*, 132.
(720) Galiova, M.; Kaiser, J.; Novotny, K.; Novotny, J.; Vaculovic, T.; Liska, M.; Malina, R.; Stejskal, K.; Adam, V.; Kizek, R. *Appl. Phys. A: Mater. Sci. Process.* **2008**, *93*, 917.
(721) Becker, J. S.; Sela, H.; Dobrowolska, J.; Zoriy, M. *Int. J. Mass Spectrom.* **2008**, *270*, 1.
(722) Becker, J. S.; Sela, H.; Dobrowolska, J.; Zoriy, M.; Becker, J. S. *Int. J. Mass Spectrom.* **2008**, *270*, 1.
(723) Becker, J. S.; Gorbunoff, A.; Zoriy, M.; Izmer, A.; Kayser, M. *J. Anal. At. Spectrom.* **2006**, *21*, 19.
(724) Zoriy, M. V.; Kayser, M.; Becker, J. S. *Int. J. Mass Spectrom.* **2008**, *273*, 151.
(725) Zoriy, M. V.; Becker, J. S. *Rapid Commun. Mass. Spectrom.* **2009**, *23*, 23.
(726) Meyer, K. A.; Ovchinnikova, O.; Ng, K.; Goeringer, D. E. *Rev. Sci. Instrum.* **2008**, *79*, 123710.

CR900223A